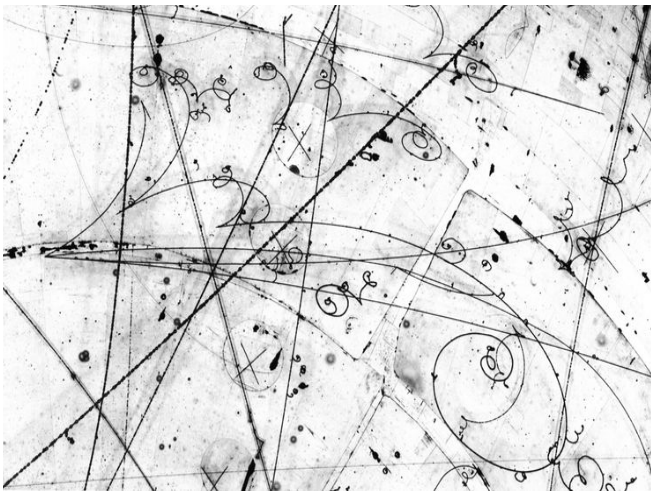

Probing the CP nature of the Higgs' couplings in $t\bar{t}H$ events at the LHC

Duarte Rocha Peixoto Azevedo
Mestrado em Física
Departamento de Física e Astronomia
2017

Orientador
António Joaquim Onofre de A. R. Gonçalves, Professor Associado
Faculdade de Ciências da Universidade do Minho

Coorientador
Frank Filthaut, Professor Associado
Faculdade de Ciências da Universidade de Radboud

MSc

Todas as correções determinadas pelo júri, e só essas, foram efetuadas.

O Presidente do Júri,

Porto, / /

“Studying elementary particles is like smashing two mechanical clocks together and trying to guess how they work based on the springs, gears, and levers that fly out.”

-Unknown

Acknowledgements

I want to thank my advisors Prof. António Onofre and Prof. Frank Filthaut for the incredible amount of time, patience and knowledge shared with me. Needless to say, their support was crucial in helping me through this step of my academic path. They were not only advisors but friends. I also want to thank my family and friends which, one way or another, helped me greatly in completing this thesis. To all of you a sincere thank you.

UNIVERSIDADE DO PORTO

Abstract

Faculdade de Ciências
Departamento de Física e Astronomia

MSc. Physics

Probing the CP nature of the Higgs' couplings in $t\bar{t}H$ events at the LHC

by Duarte AZEVEDO

The CP nature of the Higgs coupling to top quarks, using $t\bar{t}h$ events produced in proton-proton collisions, is addressed in this thesis for a center of mass energy of 13 TeV at the LHC. Semileptonic final states of $t\bar{t}h$ with one lepton and at least six jets from the decays

$$t \to bW^{+} \to b(l^{+}\nu_l \text{ or } jj)$$

$$\bar{t} \to \bar{b}W^{-} \to \bar{b}(l^{-}\bar{\nu}_l \text{ or } jj)$$

$$h \to b\bar{b}$$

are analysed. Pure scalar ($h = H$) and pseudo-scalar ($h = A$) Higgs boson signal events, generated with *MadGraph5_aMC@NLO*, are fully reconstructed by applying a kinematic fit. New angular distributions of the decay products, as well as CP angular asymmetries are explored to separate the scalar from the pseudo-scalar components of the Higgs boson and reduce the contribution from the dominant irreducible background $t\bar{t}b\bar{b}$. Significant differences between signal and Standard Model (SM) background are observed for the angular distributions and asymmetries, even after the full kinematic fit reconstruction of the events, allowing to define the best observables for a global fit of the Higgs couplings parameters. A dedicated analysis is applied to efficiently identify signal events and reject as much as possible the Standard Model expected background at the LHC.

Sumário

A natureza do acoplamento do bosão de Higgs aos quarks top, usando eventos $t\bar{t}h$ produzidos em colisões de protões, é estudada nesta dissertação para uma energia de centro de massa de 13 TeV no LHC. Estados finais semi-leptónicos de $t\bar{t}h$ com um leptão e pelo menos seis jatos dos decaímentos

$$t \to bW^+ \to b(l^+\nu_l \text{ ou } jj)$$
$$\bar{t} \to \bar{b}W^- \to \bar{b}(l^-\bar{\nu}_l \text{ ou } jj)$$
$$h \to b\bar{b}$$

são analisados. Eventos com Higgs escalares ($h = H$) e pseudo-escalares ($h = A$), gerados com *MadGraph5_aMC@NLO*, são reconstruídos através de um ajuste cinemático. Novas distribuições e assimetrias angulares são exploradas para separar as componentes escalares e pseudo-escalares do Higgs e reduzir as contribuições do fundo irredutível dominante $t\bar{t}b\bar{b}$. Diferenças significativas entre sinal e fundo do Modelo Padrão são encontradas nas distribuições angulares e assimetrias, mesmo depois do processo de reconstrução, permitindo assim a definição das melhores observáveis para o ajuste global dos parâmetros do acoplamento do Higgs. Uma análise dedicada é efectuada para identificar eventos de sinal e rejeitar ao máximo eventos de fundo do Modelo Padrão.

Contents

List of Figures

List of Tables

List of Abbreviations

SM	**S**tandard **M**odel
BSM	**B**eyond **S**tandard **M**odel
EM	**E**lectro**m**agnetic/**E**lectro**m**anetism
EW	**E**lectro**w**eak
QED	**Q**uantum **E**lectro**d**ynamics
QCD	**Q**uantum **C**hromo**d**ynamics
QFT	**Q**uantum **F**ield **T**heory
IVB	**I**ntermediate **V**ector **B**oson
(N)LO	(**N**ext-to) **L**eading **O**rder
(N)LL	(**N**ext-to) **L**eading **L**ogarithm
CP	**C**harge and **P**arity
MC	**M**onte-**C**arlo
Gen	Monte-Carlo **Gen**enerator level
Rec	**Rec**construction level
MLE	**M**aximum **L**ikelihood **E**stimate
TM	**T**ruth **M**atch
TF	**T**ransfer **F**unction
MET	**M**issing (E_t) **T**ransverse **E**nergy
LHC	**L**arge **H**adron **C**ollider
ATLAS	**A** **T**oroidal LHC **A**pparatu**s**
Had	**Had**ronic
Lep	**Lep**tonic
CL	**C**onfidence **L**evel

Overview

This thesis focus on developing and motivating a full set of variables that are sensitive to the Higgs couplings to top quarks, not only from a theoretical standpoint but also considering the acceptance region and resolution effects of the ATLAS detector. The methodology is divided into following steps:

1. Generating $t\bar{t}H(A)$/background events with the current LHC specifications, proton-proton collisions with a center-of-mass (CM) of $\sqrt{13}$ TeV.
2. Implementing a fast detector simulation that mimics the ATLAS detector. For a realistic analysis, the acceptance region available and resolution are limited, thus the CP variables to be defined have to be sensitive within this window.
3. Developing a full kinematic fit, capable of reconstructing the expected detected decay products from generated sample.
4. Searching and motivating CP sensitive variables for the Higgs' coupling to the top quarks.
5. Implementing a multivariate analysis for those variables, studying them through the whole spectrum of the Standard Model (SM) background and computing confidence limits for the existence of the different signals.

Step one is concerned in generating collision events following a standard model- and a *beyond* standard model (BSM) lagragian, which incorporates a pseudo-scalar coupling between the Higgs' field and the fermions' field. Chapter 1 introduces the standard model as a whole. The Higgs' mechanism is explained and its coupling to quarks is generalized to incorporate a CP-odd component.

The LHC and ATLAS experimental apparatus are described in chapter 2.

Chapter 3 studies in full detail the expected backgrounds for the process at hand, $t\bar{t}H(A)$, its topologies and signal/background ratios. From thereon, the complete generation of events (signal and background) is described, finalizing with the description of the `Delphes` package, a fast detector simulation.

Chapter 4 introduces the Bayesian analysis and the concept of Maximum Likelihood Estimate as a statistical tool that is used for the kinematic reconstruction.

The development of a kinematic fit is described in chapter 5. This part covers point three in its entirety.

Chapter 6 motivates and presents a set of CP sensitive variables. In turn, these are used in a multivariate analysis which allows extraction of 95% Confidence Level (CL) limits on the production of signal events at the LHC, after event selection, in the background hypothesis only.

Chapter 1

Introduction

1.1 Standard Model

The Standard Model [49] (SM) is a set of theories that explains three out of the four fundamental interactions: Electromagnetic, Weak and Strong. The Gravitational force with no success[1]. It also contains the catalogue of all discovered elementary particles and their properties. This model explains by far the largest amount of phenomena compared to others. Therefore, it seems the correct way to explain nature as a whole. Furthermore, it correctly predicts the region of applicability of its perturbative and non-perturbative approaches, successfully unifies the electromagnetic with the weak force and includes massive particles by means of the Higgs' Mechanism.

Nonetheless, since it is not in agreement with Einstein's Theory of General Relativity, fails to account gravity as a mean of explaining the dynamic of the universe and does not contain a viable dark matter candidate.

1.1.1 Fermions

Fermions constitute part of the SM of particles. They are characterized by having a half-integer spin value. All the elementary fermions (discovered) have a spin of 1/2. Fermions obey the Fermi-Dirac's Statistics. Namely that, two identical fermions cannot occupy a state with the exact same quantum numbers. This sets the wave-function of the system as antisymmetric with respect to all indistinguishable particles permutations. This is often called Pauli's Exclusion Principle.

The fermions are divided into two major groups: leptons and quarks.

Leptons

Leptons only interact via the weak and electromagnetic force. Table 1.1 lists the fundamental leptons and their properties.

Particle	Family	Charge (e)	Mass	Interactions
Electron - $e^{\pm}$	1	± 1	511 keV	EM, Weak.
Elec. Neutrino - ν_e	1	0	< 2 eV	Weak.
Muon - $\mu^{\pm}$	2	± 1	105.7 MeV	EM, Weak.
Muon Neutrino - ν_μ	2	0	< 2 eV	Weak.
Tau - $\tau^{\pm}$	3	± 1	1.78 GeV	EM, Weak.
Tau Neutrino - ν_τ	3	0	< 2 eV	Weak.

TABLE 1.1: Standard Model Leptons [50].

---

[1] The Gravitational force will not be taken into consideration for here on out.

Quarks

In contrast with leptons, quarks interact via all forces. The strong force imposes that there cannot be a lone quark for arbitrary large distances, due to the increasing effective interaction strength with distance. Quarks are the fundamental constituents of some composed particles like mesons and baryons, the latter being the building block for atoms' nuclei. A composed particle made out of quarks is called a hadron.

The list of all discovered quarks and their properties is shown in Table 1.2.

Particle	Family	Charge (e)	Mass	Interactions
Up - u	1	$2/3$	$1.3 - 3.3$ MeV	EM, Weak, Strong.
Down - d	1	$-1/3$	$4.1 - 5.8$ MeV	EM, Weak, Strong.
Charm - c	2	$2/3$	1.27 GeV	EM, Weak, Strong.
Strange - s	2	$-1/3$	101 MeV	EM, Weak, Strong.
Top - t	3	$2/3$	173.2 GeV	EM, Weak, Strong.
Bottom - b	3	$-1/3$	4.19 GeV	EM, Weak, Strong.

TABLE 1.2: Standard Model Quarks [50].

1.1.2 Gauge Bosons

The other *half* of the SM of particles is composed of bosons. Bosons have integer valued spin, thus, they obey Bose-Einstein's statistics. Namely that, identical bosons can have the exact same quantum numbers and a bosons' system's wave-function has to be symmetric. All known elementary bosons are gauge ones, excluding the Higgs. These particles appear as mediators of the several forces after imposing local gauge symmetry to their corresponding Lagrangian. All gauge bosons have a spin of 1.

The list of gauge bosons is given in Table 1.3.

Particle	Charge (e)	Mass	Interaction
Photon - γ	0	0	EM
W bosons - $W^{\pm}$	±1	80.385 GeV	Weak
Z boson - Z^0	0	91.1876 GeV	Weak
Gluon - g	0	0	Strong

TABLE 1.3: Standard Model Gauge Bosons [50].

1.2 Top Quark Physics

The top quark has charge equal to two thirds that of the electron and the *third* component projection of weak isospin equals one half. It is a member of the third quark family. The other being the bottom quark.

Its phenomenology is driven by its large mass. Being heavier than a W boson, it is the only quark that decays weakly, i.e., into a real W boson and a b quark. At NLO, the theoretical width of the top-quark [50] is

$$\Gamma_t = 1.35 \text{ GeV}/c^2 \tag{1.1}$$

hence, its very short lifetime ($\sim 0.5 \times 10^{-24}$ s) prohibits the formation of top-flavoured hadrons[2] or $t\bar{t}$-quarkonium-bound states. In addition, it is the only quark whose Yukawa coupling to the Higgs boson is of the order of unity.

For these reasons the top quark plays a special role in the SM and in many extensions thereof. Its phenomenology provides a unique laboratory where one's understanding of the strong interactions, both in the perturbative and non-perturbative regimes, can be tested.

Accurate knowledge of its properties (mass, couplings, production cross section, decay branching ratios, etc.) can bring key information on fundamental interactions at the electroweak breaking scale and beyond.

1.2.1 Production and decay at the LHC

In hadron colliders, like the LHC, top quarks are dominantly produced in pairs [18] through the processes at leading order in QCD

$$\begin{aligned} q\bar{q} &\to t\bar{t} \\ gg &\to t\bar{t} \end{aligned} \tag{1.2}$$

Figure 1.1 shows the *leading-order* (LO) Feynman diagrams for the top quark pair production.

(A) Quark/Anti-quark annihilation.

(B) Gluon fusion.

FIGURE 1.1: Top quark pair production example diagrams (LO).

When the LHC reaches energies around $\sqrt{s} = 14$ TeV, about 90% of the production will be from the latter process ($\sim 80\%$ at $\sqrt{s} = 7$ TeV).

The theoretical computations of the total cross section are available at *next-to-next-to leading order* (NNLO) with *next-to-next-to leading-log* (NNLL) soft gluon resummation [30]. If one takes the top quark mass to be 173.2 GeV/c^2, the cross sections of pair production at the LHC should be

$$\begin{aligned} \sigma_{t\bar{t}} &= 173.6^{+4.5+8.9}_{-5.9-8.9}\ \text{pb}, & \sqrt{s} &= 7\ \text{TeV} \\ \sigma_{t\bar{t}} &= 247.7^{+6.3+11.5}_{-8.5-11.5}\ \text{pb}, & \sqrt{s} &= 8\ \text{TeV} \\ \sigma_{t\bar{t}} &= 816.0^{+19.4+34.4}_{-28.6-34.4}\ \text{pb}, & \sqrt{s} &= 13\ \text{TeV} \end{aligned} \tag{1.3}$$

In Figure 1.2, the cross section of top quark pair production is represented as a function of the CM energy.

At the LHC, single top-quark production mechanisms are also expected [47] but with smaller cross sections, these include for instance

$$\begin{aligned} q\bar{q}' &\to t\bar{b} \\ qb &\to q't \end{aligned} \tag{1.4}$$

---

[2] Hadronization is the process where additional quarks emerge from the vacuum to create a colorless final state, namely, hadrons. This emergent phenomenon is due to color confinement, which states that a lone quark cannot exist indefinitely.

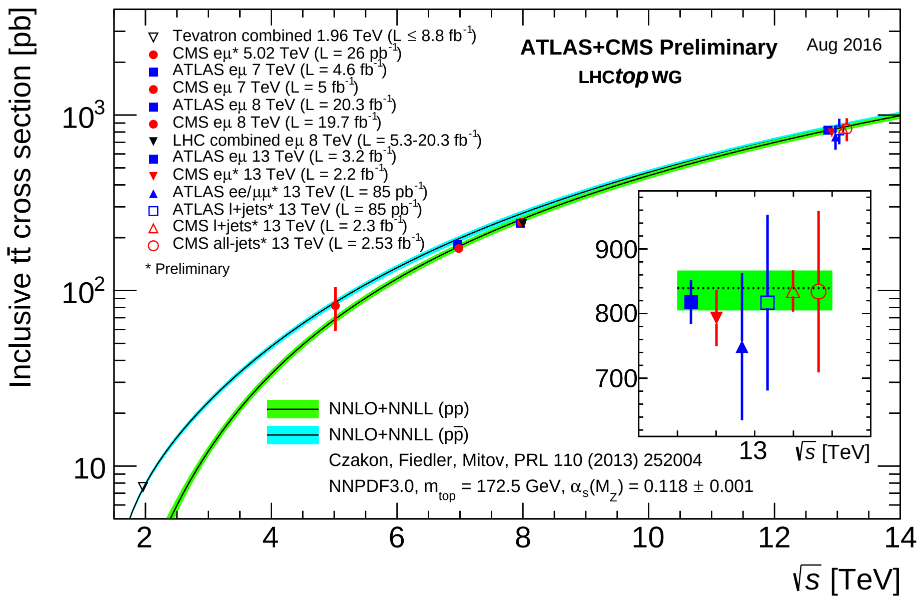

FIGURE 1.2: Theoretical and Experimental values of top pair production cross section (NNLO) vs. CM energy($\sqrt{s}$) [16]. Mass of the (anti)top-quark taken as $m_t = 172.5$.

mediated by virtual s-channel and t-channel W bosons. At the LHC, s- and t-channel production of top and anti-top quarks have different cross sections due to the charge asymmetry of the initial state. Example diagrams are shown in Figure 1.3.

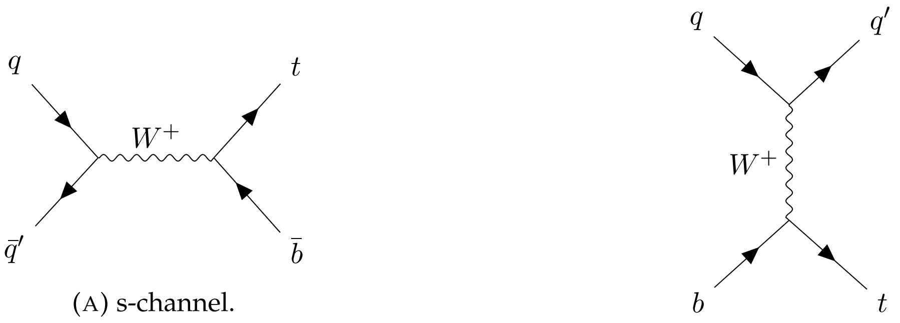

(A) s-channel.

(B) t-channel.

FIGURE 1.3: Single top quark production diagram examples (LO).

Theoretical NNLO cross section values for the s, t-channel single top quark ($t+\bar{t}$) are computed for $m_t = 173.3$ GeV/c^2 [19]. For the t-channel,

$$\begin{aligned} \sigma_t &= 65.7^{+1.9}_{-1.9}\ \text{pb}, & \sqrt{s} &= 7\ \text{TeV} \\ \sigma_t &= 85.1^{+2.5}_{-1.4}\ \text{pb}, & \sqrt{s} &= 8\ \text{TeV} \end{aligned} \tag{1.5}$$

the proportion of top/anti-top quarks should be around 65%. For the s-channel,

$$\begin{aligned} \sigma_s &= 4.5^{+0.2}_{-0.2}\ \text{pb}, & \sqrt{s} &= 7\ \text{TeV} \\ \sigma_s &= 5.5^{+0.2}_{-0.2}\ \text{pb}, & \sqrt{s} &= 8\ \text{TeV} \end{aligned} \tag{1.6}$$

the proportion of top/anti-top quarks should be around 69%.

At these energy regimes another process becomes relevant, the Wt-associated production [27],

$$\begin{aligned} bg &\to W^-t \\ \bar{b}g &\to W^+\bar{t} \end{aligned} \tag{1.7}$$

Production example diagrams are shown in Figure 1.4. At NNLO, Wt associated production has the following theoretical cross sections for the LHC [50],

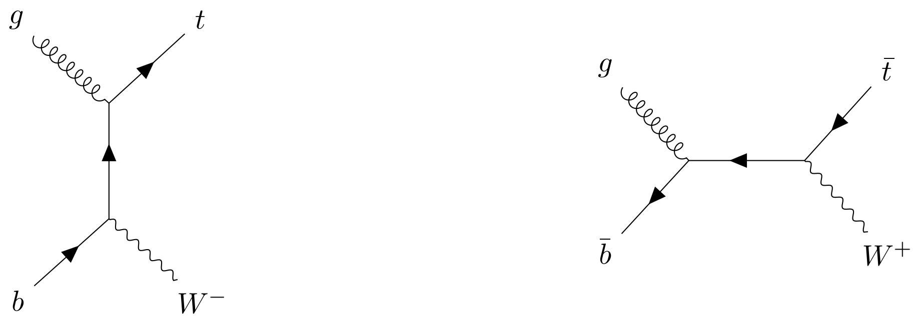

FIGURE 1.4: Top quark associated production with a W boson example diagrams (LO).

$$\begin{aligned} \sigma_{Wt} &= 15.5^{+1.2}_{-1.2}\ \text{pb}, & \sqrt{s} &= 7\ \text{TeV} \\ \sigma_{Wt} &= 22.1^{+1.5}_{-1.5}\ \text{pb}, & \sqrt{s} &= 8\ \text{TeV} \end{aligned} \tag{1.8}$$

with an equal production on both top and anti-top quarks. The full run of the cross section for a continuous range of $\sqrt{s}$ can be seen in Figure 1.5.

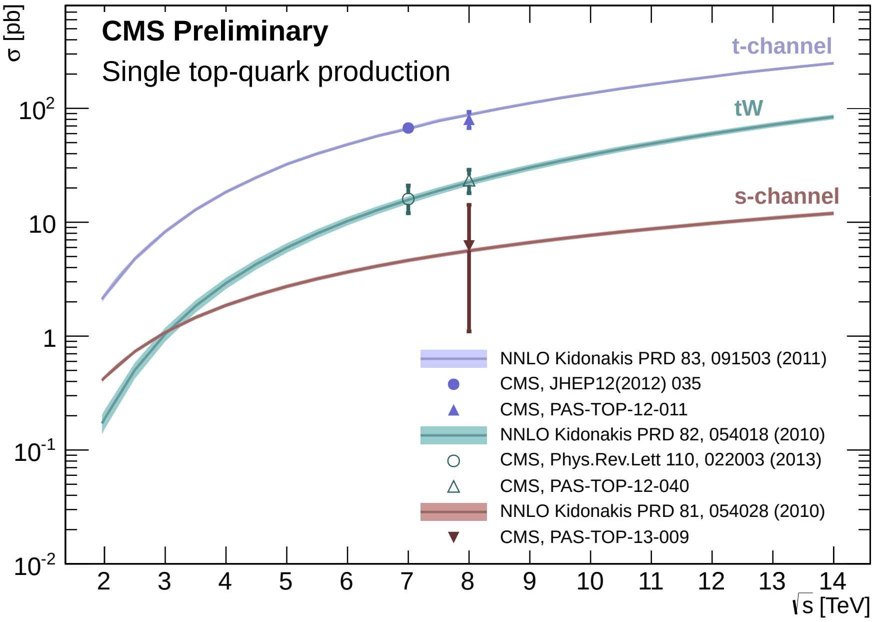

FIGURE 1.5: Theoretical and Experimental values of single top production cross section (NNLO) vs. CM energy($\sqrt{s}$) [58]. Mass of the (anti)top-quark taken as $m_t = 172.5$.

It is instructive to have a look at the CKM quark mixing matrix [50] to analyze the top quark decay modes,

$$V_{\text{CKM}} = \begin{bmatrix} 0.97427 \pm 0.00014 & 0.22536 \pm 0.00061 & 0.00355 \pm 0.000015 \\ 0.22522 \pm 0.00061 & 0.97343 \pm 0.000015 & 0.0414 \pm 0.0012 \\ 0.00886^{+0.00033}_{-0.00032} & 0.0405^{+0.0011}_{-0.0012} & 0.99914 \pm 0.00005 \end{bmatrix} \tag{1.9}$$

we can assume that $|V_{tb}| \gg |V_{td}|, |V_{ts}|$. Therefore, single top production is mainly driven by the $|V_{tb}|^2$ term. By the same reasoning, and since the top quark has a mass above the Wb threshold, it is expected mostly $t(\bar{t}) \to W^{\pm}b(\bar{b})$ events for the corresponding decays.

Let us focus on the top quark pair decay chain since it is expected that $t\bar{t}$ events will be the main background for $t\bar{t}H(A)$ signal events. It is possible to categorize the decay modes of both signal and main background in the same fashion since an associated Higgs should not alter the decay amplitudes of the accompanying top quarks. The top quark pair production (with our without associated Higgs) can be divided into three major decay modes [50],

$$\begin{aligned} &\text{A.} \quad t\bar{t}(H) \to W^+bW^-\bar{t}(Y_H) \to q\bar{q}'bq''\bar{q}'''\bar{b}(Y_H) && (45.7\%) \\ &\text{B.} \quad t\bar{t}(H) \to W^+bW^-\bar{t}(Y_H) \to q\bar{q}'bl^-\bar{\nu}_l\bar{b}(Y_H) + l^+\nu_l bq''\bar{q}'''\bar{b}(Y_H) && (43.8\%) \\ &\text{C.} \quad t\bar{t}(H) \to W^+bW^-\bar{t}(Y_H) \to l^+\nu_l bl^-\bar{\nu}_l\bar{b}(Y_H) && (10.5\%) \end{aligned} \tag{1.10}$$

where every quark hadronizes and give rise to showers that are identified as jet(s) and Y_H are the decay products of the Higgs. A, B and C refer to all-jets, semi-lepton (lepton + jets) and di-lepton (leptons + b jets) channels, respectively. Their ratio is given in parenthesis.

While l in the above decay chains refers to all leptons (electrons, muons or taus), most analyses distinguish e and μ from τ due to its reconstruction difficulties.

Identification of top quarks in the electroweak single top channel is substantially more difficult due to a less distinctive signature and much larger backgrounds, mostly due to top pair-production and W+jets production.

In this thesis, it is only considered the **semi-leptonic channel** with electrons and muons for both signal- ($t\bar{t}H(A)$) and main background ($t\bar{t}$) events.

1.2.2 Spin Correlations

One of the unique features of the top quark is that it decays before hadronization spoils the correlation between final state angular distributions and the top quark spin direction. Thus, the top-quark polarization is directly observable via the angular distribution of its decay products [43].

It is possible to define and measure observables sensitive to the top-quark spin and its production mechanisms. Although the top- and anti-top quarks produced by strong interactions in hadron collisions are essentially unpolarized, the spins of t and $\bar{t}$ are correlated. At the LHC, where gluon fusion is more common, ${}^1S_0$ states are the most frequent ones. Specially for the case where the invariant mass is close to the pole one.

It is shown that the direction of the top-quark spin is highly correlated to the angular distributions of its decayed daughters. Its joint angular distribution reads

$$\frac{1}{\sigma}\frac{d^2\sigma}{d(\cos\theta_+)d(\cos\theta_-)} = \frac{1}{4}\left(1 + B_1\cos\theta_+ + B_2\cos\theta_- - C\cos\theta_+ \cdot \cos\theta_-\right) \tag{1.11}$$

where $d^2\sigma/dxdy$ is the double differential distribution of the decay and θ_+, θ_- are the angles made by the direction of the children of the top quark with respect to the spin quantization axis (*a priori* arbitrary), all measured at the top quark's rest frame. The CP sensitive variables B_1 and B_2 are null for the pure scalar interactions. At the LHC, the value of C (NLO) is 0.326 in the helicity basis [18].

The importance of this correlation is that it is modified if a new $t\bar{t}$ production mechanism, such as: through a Z' boson, Kaluza-Klein gluons, or a **Higgs boson**, is considered. This means that certain angular variables might be sensitive (and will) to the Higgs' production.

1.3 Higgs Boson's Physics

To venture into this last piece of the Standard Model one has to understand its motivations.

In analogy with electricity and magnetism, which are manifestations of electromagnetism, a link exists between the latter and weak interactions. Electromagnetism and weak interactions fit into a locally gauge invariant description inside a broader symmetry group: $SU(2)_L \times U(1)_Y$[3]. Above the electroweak unification energy threshold[4], of about 100 GeV [24], both interactions merge into one. Below, only the observable $U(1)_{\text{EM}}$ symmetry[5] remains as result of spontaneous symmetry breaking.

This new unified theory, called Electroweak, describes both phenomena as one but has serious inconsistencies. These motivated the Higgs' mechanism [44]. On enumerating the inconsistencies it will be used the standard notation of particle physics and quantum field theory.

1] Local $SU(2)_L \times U(1)_Y$ gauge invariance forbids massive particles. This is true for both massive gauge bosons and fermions.

In the case of **bosons** this is easily comprehended if we take the analogous case of QED, where the Lagrangian density reads

$$\mathcal{L}_{\text{QED}} = \overline{\psi}\left(i\gamma^{\mu}\partial_{\mu} - m\right)\psi - \frac{1}{4}F^{\mu\nu}F_{\mu\nu} - e\overline{\psi}\gamma^{\mu}\psi A_{\mu} \tag{1.12}$$

If one were to add a mass term *ad hoc* to the gauge field A_μ, one would explicitly break $U(1)$ gauge invariance which is necessary if electric charge is to be conserved.

$$\frac{1}{2}m_{\gamma}^{2}A_{\mu}A^{\mu} \xrightarrow{U(1)} \frac{1}{2}m_{\gamma}^{2}(A_{\mu} + \frac{1}{e}\partial_{\mu}\lambda(x))((A^{\mu} + \frac{1}{e}\partial^{\mu}\lambda(x)) \neq \frac{1}{2}m_{\gamma}^{2}A_{\mu}A^{\mu} \tag{1.13}$$

For the case of QED, the problem is avoided since the photon's mass is zero. Hence, there is no mass term to begin with. Nevertheless, for the electroweak model the same argument holds, where the W and Z bosons *do have mass*[6]. Therefore, with the inclusion of mass terms, the corresponding symmetry is lost.

It can be noted, on the example above, that the fermion field was massive. The simplicity of the symmetry involved makes its existence indifferent to the characteristics of the fermion's field. That does not happen on more complex degrees of freedom, like the electroweak case.

In the EW case, fermions are not invariant to gauge transformations due to the fermions' chirality components. One knows that the gauge bosons $\vec{W}_\mu$ couple only to left-handed fermions, whereas the B_μ boson couples to both. This translates into a transformation law that differs for each chirality eigenstate

$$\begin{aligned} \psi_R &\xrightarrow{SU(2)_L\times U(1)_Y} \psi_R' = e^{i\beta(x)\hat{Y}}\psi_R \\ \psi_L &\xrightarrow{SU(2)_L\times U(1)_Y} \psi_L' = e^{i\alpha^i(x)\hat{T}_i + i\beta(x)\hat{Y}}\psi_L \end{aligned} \tag{1.14}$$

---

[3] The direct product of a SU(2) symmetry of the weak isospin degree of freedom with U(1) symmetry of the hypercharge degree of freedom.

[4] The equilibrium temperature of the universe.

[5] Associated with the gauge invariance of the photons' field.

[6] This will be seen in the development of the full Higgs' mechanism.

where $\hat{T}_i$ and $\hat{Y}$ are the generators of the $SU(2)_L$ and $U(1)_Y$ groups, respectively[7].

Since a mass term can always be written as

$$\begin{aligned} m_f\overline{\psi}\psi &= m_f\left(\overline{\psi}_L + \overline{\psi}_R\right)(\psi_L + \psi_R) \\ &= m_f(\overline{\psi}_L\psi_R + \overline{\psi}_R\psi_L) \end{aligned} \tag{1.15}$$

where $\overline{\psi}_L\psi_L = \overline{\psi}_R\psi_R = 0$, the Lagrangian would not remain invariant for a general local $SU(2)_L \times U(1)_Y$ transformation. Therefore, it would explicitly break symmetry.

2] Unitarity is violated. Several processes, like WW-scattering, break unitarity at high energies as the cross section increases indefinitely with energy

$$\sigma(WW \to ZZ) \propto E^2 \tag{1.16}$$

This makes the theory non-renormalizable which is essential if one is to be able to make reasonable physical predictions from the theory.

1.3.1 Higgs Mechanism

As we want the theory to be renormalizable, its high degree of symmetry cannot be lost[8]. Hence, we need to keep the full Lagrangian invariant to local $SU(2)_L \times U(1)_Y$ transformations. On the other hand, the ground state of the system does not need to follow the same requirements necessarily.

Similarly to the case of ferromagnetism, we can have a ground state which is invariant under full electroweak gauge transformations, above the unification energy (the corresponding Curie point), and only invariant to $U(1)_{\text{EM}}$ below that energy threshold.

In order to feature the Lagrangian with spontaneous symmetry breaking one can introduce a new particle, gifted with a suitable potential. This potential will keep the Lagrangian invariant to the full symmetry in both regimes but not its vacuum. This can be achieved through a process analogous to a phase transition.

Additionally, above the electroweak threshold, no particle is massive and left-handedness will be exclusive to fermions and right-handedness to anti-fermions. In the phase below the EW threshold, the vacuum acquires a non-null expectation value. This expectation value will generate mass terms for the respective particles and, in turn, massive fermions will have access to both chirality components. Moreover, through boson mixing, the physical bosons will have their respective mass, in a self-consistent manner.

To illustrate the mechanism, let us begin with the Electroweak Lagrangian [51] considering, for simplicity, that our fermion table is only composed of leptons[9]. Above the unification energy it reads

$$\mathcal{L}_{\text{EW}} = i\sum_l \left[\overline{\Psi}_l^L \not{D}_1 \Psi_l^L + \overline{\psi}_l^R \not{D}_2 \psi_l^R + \overline{\psi}_{\nu_l}^R \not{D}_3 \psi_{\nu_l}^R\right] - \frac{1}{4}\mathcal{W}_{\mu\nu}^a \mathcal{W}_a^{\mu\nu} - \frac{1}{4}\mathcal{B}^{\mu\nu}\mathcal{B}_{\mu\nu} \tag{1.17}$$

Regarding the notation used: The sum over l is through leptonic families. From here on out, a sum will be implicit every time an index is repeated in the same term. Thus, all sums related with indexes will be omitted.

The slashed notation, $\not{X}$, correspond to the Feynman's one of inner product $\gamma^\mu X_\mu$, where γ^μ are the usual Dirac's gamma matrices. Again, a sum over space-time coordinate indexes, μ, is implicitly present.

---

[7] An implicit summation over repeated indexes is assumed.

[8] This is not always true. What usually happens is that non-renormalizable theories can be seen to be low-energy effective theories arising from the spontaneous breaking of a gauge symmetry. Casting them in this light restores renormalizability.

[9] Quarks are of special interest, since this study is focused on their couplings'. As such, a section on this chapter is dedicated to study quarks within the Higgs' mechanism.

All space-time indexing will be written in Greek letters, whereas groups' component indexing will be with the one first few Latin letters. Space-time 4-vectors are written with one of the last Latin letter, for instance, x.

The left-handed fermionic fields, $\Psi_l^L = (\psi_l^L, \psi_{\nu_l}^L)^T$, are together in weak isospin doublets and have hypercharge $Y = -\frac{1}{2}$. The right-handed fermionic fields, ψ_l^R and $\psi_{\nu_l}^R$, are weak isospin singlets with hypercharge $Y = -1$ and $Y = 0$, respectively.

These components are obtained from the complete Dirac field by acting with the chirality projection operators on it

$$\begin{aligned} \psi^L(x) &= \hat{P}_L \psi(x) = \frac{1}{2}(1 - \gamma_5)\psi(x) \\ \psi^R(x) &= \hat{P}_R \psi(x) = \frac{1}{2}(1 + \gamma_5)\psi(x) \end{aligned} \tag{1.18}$$

where γ_5 is the last of the Dirac's gamma matrices.

To denote the Dirac's adjoint of the fields we use

$$\begin{aligned} \overline{\Psi} &\equiv \Psi^\dagger \gamma_0 \\ \overline{\psi} &\equiv \psi^\dagger \gamma_0 \end{aligned} \tag{1.19}$$

Even thought the Lagrangian is symmetric between right- and left-handed fermions, the way it is written is not. This is to accommodate the different fermions' fields into groups that share the same transformation laws. The local transformations, under the $SU(2)_L \times U(1)_Y$ group, of the different Dirac's fields are

$$\begin{aligned} &\Psi_l^L(x) \to \Psi'^L(x) = \exp\Big(i g_W \hat{\tau}^i w^i(x) - i\frac{g_Y}{2}\beta(x)\Big)\Psi_l^L(x) \\ &\psi_l^R(x) \to \psi_l'^R(x) = \exp(-i g_Y \beta(x))\psi_l^R(x) \\ &\psi_{\nu_l}^R(x) \to \psi_{\nu_l}'^R(x) = \psi_{\nu_l}^R(x) \end{aligned} \tag{1.20}$$

where g_W and g_Y are the *nude* weak isospin and hypercharge coupling constants.

In order to maintain gauge invariance, interaction terms are responsible to counterbalance the additional terms that appear from the transformed kinetic terms. These interaction terms add up to form the generalized momentum operators

$$\begin{aligned} D_1^\mu &\equiv \partial^\mu + i g_W \frac{\hat{\tau}_i}{2} W_i^\mu - i\frac{g_Y}{2} B^\mu \\ D_2^\mu &\equiv \partial^\mu - i g_Y B^\mu \\ D_3^\mu &\equiv \partial^\mu \end{aligned} \tag{1.21}$$

where $\partial_{\mu(\nu)} \equiv \frac{\partial}{\partial x^{\mu(\nu)}}$ represent partial derivatives with respect to one of the four space-time components.

The generalized momentum operators are also called covariant derivatives. These covariant derivatives are invariant to local gauge transformations and differ for each field due to the fields' transformation laws being different. The subscript **1**, **2** and **3** corresponds to the left-handed doublet, lepton right-handed singlet and neutrino right-handed singlet, respectively.

The gauge bosons' energy-momentum tensors are given by $\mathcal{W}_{\mu\nu}^a$ and $\mathcal{B}_{\mu\nu}$, respectively, and read

$$\begin{aligned} \mathcal{W}_{\mu\nu}^a &= \partial_\mu W_\nu^a(x) - \partial_\nu W_\nu^a(x) + g_W \epsilon^{abc} W_\mu^b(x) W_\nu^c(x) \\ \mathcal{B}_{\mu\nu} &= \partial_\mu B_\nu(x) - \partial_\nu B_\nu(x) \end{aligned} \tag{1.22}$$

with ϵ^{abc} being the fully anti-symmetric tensor with regards to permutations of its indexes. The energy-momentum tensors are also invariant under local gauge transformations.

At this point, one has a Lagrangian that represents a universe composed of leptons, electroweak bosons and their respective interactions, in the unified electroweak regime. This Lagrangian was the first step towards a theory which could incorporate mass.

The Higgs field is added to generate mass terms when it goes through a phase transition. This phase transition has the purpose of making the new ground state *spontaneously* break symmetry, reducing it to a $U(1)_{\text{EM}}$ symmetric. This will enable the photon to remain massless.

Intuition would say that this new field should be gifted with isospin and hypercharge in order for spontaneous symmetry breaking of the ground state to be possible. This is right and, as will be seen, the simplest case of an isospin doublet is sufficient

$$\Phi(x) = \begin{bmatrix} \phi_a(x) \\ \phi_b(x) \end{bmatrix} \tag{1.23}$$

where $\phi_a(x)$ and $\phi_b(x)$ are scalars under Lorentz transformations.

In a isospin doublet, the isospin *charge* is set *a priori* for each component. Conversely, the hypercharge can be left to decide. This will be convenient, as we shall see.

The local transformations under $SU(2)_L \times U(1)_Y$ are of the form

$$\Phi(x) \to \Phi'(x) = \exp\Big(ig_W \hat{\tau}^i w^i(x) + ig_Y \beta(x) \hat{Y}\Big)\Phi(x) \tag{1.24}$$

where $\hat{Y}$ is the hypercharge operator.

Let us now consider that $\mathcal{L}_{EW}$ represent the new Lagrangian with the new field, related with the previous (old) one by

$$\mathcal{L}_{EW} = \mathcal{L}_{\text{old}} + (D^\mu \Phi)^\dagger (D_\mu \Phi) - \mu^2 (\Phi^\dagger \Phi) - \lambda (\Phi^\dagger \Phi)^2 \tag{1.25}$$

This is the simplest case of a self-interacting Higgs field. One has μ^2, which can be viewed as a mass term, and λ, which is a self-coupling constant that must be set positive to limit the energy from below.

Due to its transformation law (1.24), the covariant derivative for the new field is

$$D^\mu = \partial^\mu + ig_W \hat{\tau}_a W_a^\mu + ig_B \hat{Y} B^\mu \tag{1.26}$$

which sets the interaction between the Higgs and the boson fields. Again, these terms maintain the Lagrangian's gauge invariance.

As one can predict, the μ^2 term will be responsible for phase changes (Figure 1.6), analogously to Landau's theory of phase transitions. For $\mu^2 > 0$ one has the trivial solution for the ground state of the Φ field, with null expectation value. In quantum field theory this means that

$$|\langle 0| \hat{\Phi} |0\rangle| = 0 \tag{1.27}$$

where $\hat{\Phi}$ is the corresponding second quantized operator of the Φ field. Vacuum states are written as $|0\rangle$. The ground state is invariant under the transformation (1.24). This phase represents the initial electroweak Lagrangian (1.17), except for an added Higgs field. The other phase, where $\mu^2 < 0$, sets an imaginary mass for Φ. The previous ground state is now tachionic and has to condensate into another stable solution, which has a non-trivial expectation value

$$|\langle 0| \hat{\Phi} |0\rangle| = \sqrt{\frac{-\mu^2}{2\lambda}} = \frac{v}{\sqrt{2}} \tag{1.28}$$

with $v = \sqrt{-\mu^2/\lambda}$.

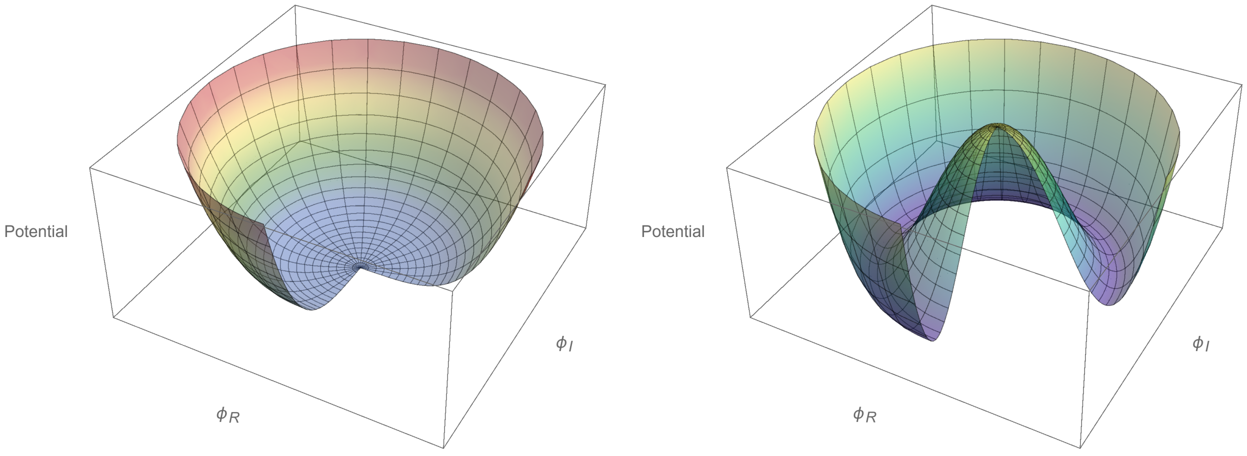

(A) $\mu^2 > 0$

(B) $\mu^2 < 0$

FIGURE 1.6: Higgs potential, simplified with just two degrees of freedom, before and after phase transition. The plot (A) represents an unbroken state whereas (B) represents a broken one.

To further study this phase, let us begin by considering, without loss of generality, that the previous vacuum condensates into the following ground state

$$\Phi_0 = \begin{bmatrix} \phi_a^0 \\ \phi_b^0 \end{bmatrix} = \begin{bmatrix} 0 \\ v/\sqrt{2} \end{bmatrix} \tag{1.29}$$

We see that the new ground state is not invariant to a general transformation of the field Φ (1.24). This means that symmetry is spontaneously broken. Nonetheless, we still expect to retain the $U(1)_{\text{EM}}$ symmetry, related with the masslessness of the photon. If electromagnetic gauge invariance is to be true, a specific value of hypercharge for the new field has to be chosen. This depends on which ground state becomes the new vacuum. Let us write down the electromagnetic gauge transformation law for the Φ field. From electroweak theory, it read

$$\Phi(x) \to \Phi'(x) = \exp\Big(-ie(\hat{Y} + \hat{\tau}_3)\beta(x)\Big)\Phi(x) \tag{1.30}$$

Considering the chosen vacuum, if we set the hypercharge to be $Y = 1/2$, the new ground state is invariant under EM gauge transformations. The photon remains massless in this phase. Furthermore, since electric charge is related to the third component of isospin and hypercharge,

$$Q = Y + \tau_3 \tag{1.31}$$

it means that the Higgs component with positive isospin is electrically charged.

The Higgs potential, as it was written, is an expansion around the first non-degenerate ground state. Since that previous ground state became unstable, it is necessary to expand it around the new stable vacuum

$$\Phi(x) = \frac{1}{\sqrt{2}} \begin{bmatrix} \eta_1(x) + i\eta_2(x) \\ v + \sigma(x) + i\eta_3(x) \end{bmatrix} \tag{1.32}$$

where $\eta_i(x)$ with $i = 1, 2, 3$ and $\sigma(x)$ are first order expansion terms in the components of the Φ.

The Goldstone theorem states that for each symmetry that is spontaneously broken the respective gauge boson acquires a mass term and an unphysical massless scalar Goldstone boson will appear. It will be seen that these Goldstone bosons are nothing but the new degrees of freedom related with the emergent longitudinal polarization of the gauge bosons that acquire mass.

Full $SU(2)_L$ and, independently, $U(1)_Y$ are lost. This can be trivially verified by applying an infinitesimal transformations of these, individually, on the vacuum state. This means that all gauge bosons associated with the generators of those groups will acquire mass. The *caveat* is that EM gauge invariance remains true, as was seen.

Since infinitesimal EM transformations are just linear combinations of infinitesimal $SU(2)_L$ and $U(1)_Y$ transformations, the actual number of symmetries lost is three. This translates into only three physical bosons[10] acquiring mass, as they correspond to the same linear combination. Consequently, only three Goldstone bosons will appear.

If one expands the Lagrangian with respect to the perturbations around the ground state (1.32) one would find that these unphysical fields are the $\eta_i(x)$ ones. These perturbations are *along* the Higgs potential circle of minima[11], as such, do not alter the potential energy.

If the only imposition on the Lagrangian is *global* gauge symmetry, the Goldstone's bosons would be a problem, as it would be impossible to *remove* them. This is an important property of imposing *local* gauge symmetry. By choosing an appropriate gauge[12], the Goldstone bosons can be *swoop* away, being implicitly present as the new degree of freedom of the massive gauge bosons.

From the previous expansion of the Φ field (1.32), if one chooses the transformation parameters of the $SU(2)_L \times U(1)_Y$ group to be

$$\begin{aligned} w_1(x) &= -\frac{\eta_2(x)}{g_w v} & \qquad w_2(x) &= -\frac{\eta_1(x)}{g_w v} \\ w_3(x) &= 0 & \beta(x) &= -\frac{2\eta_3(x)}{g_Y v} \end{aligned} \tag{1.33}$$

it results in obtaining a Goldstone boson free Lagrangian with the transformed Higgs field reading

$$\Phi'(x) = \begin{bmatrix} 0 \\ v + \sigma(x) \end{bmatrix} \tag{1.34}$$

where all the other fields transform accordingly.

To finalize the procedure it is necessary to derive mass terms for the leptons. In analogy with the bosons fields, that by interacting with a spontaneously broken field acquire a mass term, so a similar method has to be employed for the leptons.

For that end, let us consider a general Yukawa coupling [44] as follows

$$\begin{aligned} \mathcal{L}_{\text{LH}} = &- g_l \left[\overline{\Psi}_l^L(x)\psi_l^R(x)\Phi(x) + \Phi^\dagger(x)\overline{\psi}_l^R(x)\Psi_l^L(x)\right] \\ &- g_{\nu_l} \left[\overline{\Psi}_l^L(x)\psi_{\nu_l}^R(x)\tilde{\Phi}(x) + \tilde{\Phi}^\dagger(x)\overline{\psi}_{\nu_l}^R(x)\Psi_l^L(x)\right] \end{aligned} \tag{1.35}$$

where g_l and g_{ν_l} are dimensionless coupling constants.

On the second term of the right-hand side of the equation, $\tilde{\Phi}(x)$ is defined as

$$\tilde{\Phi}(x) = -i\left[\Phi^\dagger(x)\hat{\tau}_2\right]^T = \begin{bmatrix} \phi_b^*(x) \\ -\phi_a^*(x) \end{bmatrix} \tag{1.36}$$

Considering this interaction does not explicitly break gauge invariance.

---

[10] The $W^\pm$ and Z^0.

[11] In four dimensions.

[12] The unitary gauge.

As it is, one can write the full Lagrangian before symmetry breaking, in the basis of the electroweak symmetry group (the physical basis of that regime) it reads

$$\begin{aligned}
\mathcal{L}_{\mathrm{EW}} &= \mathcal{L}_{\mathrm{L}} + \mathcal{L}_{\mathrm{B}} + \mathcal{L}_{\mathrm{H}} + \mathcal{L}_{\mathrm{LH}} \\
&= i\sum_l \left[\overline{\Psi}_l^L \not{D}_1 \Psi_l^L + \overline{\psi}_l^R \not{D}_2 \psi_l^R + \overline{\psi}_{\nu_l}^R \not{D}_3 \psi_{\nu_l}^R\right] \\
&- \frac{1}{4}\mathcal{B}^{\mu\nu}(x)\mathcal{B}_{\mu\nu}(x) - \frac{1}{4}\mathcal{W}^a_{\mu\nu}(x)\mathcal{W}_a^{\mu\nu}(x) \\
&+ \left(D_\mu\Phi(x)\right)^\dagger \left(D^\mu\Phi(x)\right) - \mu^2(\Phi^\dagger(x)\Phi(x)) - \lambda(\Phi^\dagger(x)\Phi(x))^2 \\
&- g_l\left[\overline{\Psi}_l^L(x)\psi_l^R(x)\Phi(x) + \Phi^\dagger(x)\overline{\Psi}_l^R(x)\Psi_l^L(x)\right] \\
&- g_{\nu_l}\left[\overline{\Psi}_l^L(x)\psi_{\nu_l}^R(x)\tilde{\Phi}(x) + \tilde{\Phi}^\dagger(x)\overline{\psi}_{\nu_l}^R(x)\Psi_l^L(x)\right]
\end{aligned} \tag{1.37}$$

To obtain the Lagrangian after symmetry breaking, one expands the previous over the new ground state (1.32), obtaining the physical Higgs field $\sigma(x)$, as prescribed.

Subsequently, the Goldstone bosons are removed by choosing the unitary gauge (1.33).

Finally, one rewrites the electroweak gauge bosons as linear combination of the physical boson fields

$$\begin{aligned}
W_\mu(x) &= \frac{1}{\sqrt{2}}\left[W_\mu^1 - iW_\mu^2\right] & W_\mu^\dagger(x) &= \frac{1}{\sqrt{2}}\left[W_\mu^{1\dagger}(x) + iW_\mu^{2\dagger}(x)\right] \\
Z_\mu^0(x) &= \cos\theta_W W_\mu^3(x) - \sin\theta_W B_\mu(x) & A_\mu(x) &= \sin\theta_W W_\mu^3(x) + \cos\theta_W B_\mu(x)
\end{aligned} \tag{1.38}$$

The W_μ field and its adjoint $W_\mu^\dagger$ correspond to the the W^- and W^+ bosons, respectively, responsible for charged currents.

The Z_μ^0 and A_μ, the photon field, correspond to the neutral current bosons, with null charge.

The Weinberg angle, θ_W, describes how the third component of the weak isospin and the hypercharge bosons mix to form the neutral ones. It also relates the electroweak gauge boson's coupling constants with the electromagnetic one (e), it reads

$$g_W \sin\theta_W = g_Y \cos\theta_W = e \tag{1.39}$$

The complete procedure is straightforward but also very fastidious. As such, it is only going to be given the final result.

Neglecting the constant terms, it follows from equation (1.37), that $\mathcal{L}_B$ and $\mathcal{L}_H$ read

$$\begin{aligned}
\mathcal{L}_B + \mathcal{L}_H =& -\frac{1}{4}F^{\mu\nu}F_{\mu\nu} \\
& - \frac{1}{4}F^\dagger_{W\mu\nu}F_W^{\mu\nu} + m_W^2 W_\mu^\dagger W^\mu \\
& - \frac{1}{4}Z_{\mu\nu}Z^{\mu\nu} + \frac{1}{2}m_Z^2 Z_\mu Z^\mu \\
& + \frac{1}{2}(\partial^\mu\sigma)(\partial_\mu\sigma) - \frac{1}{2}m_H^2\sigma^2 \\
& + \mathcal{L}_I^{\mathrm{BB}} + \mathcal{L}_I^{\mathrm{BH}} + \mathcal{L}_I^{\mathrm{HH}}
\end{aligned} \tag{1.40}$$

where $F^{\mu\nu}$ is the well known Faraday Tensor [37]. The corresponding energy-momentum tensors of the other gauge bosons are $F_W^{\mu\nu}$, its adjoint and $Z^{\mu\nu}$. They are also differential 2-forms, and in component form, read

$$X_{\mu\nu} = \partial_\mu X_\nu - \partial_\nu X_\mu \tag{1.41}$$

The introduced mass parameters m_W, m_Z and m_H, in (1.40), are defined as

$$m_W = \frac{1}{2} v g \qquad m_Z = \frac{m_W}{\cos\theta_W} \qquad m_H = \sqrt{-2\mu^2} \tag{1.42}$$

Non-trivial interaction terms, $\mathcal{L}_I^{\mathrm{BB}}$, $\mathcal{L}_I^{\mathrm{BH}}$ and $\mathcal{L}_I^{\mathrm{HH}}$, emerge from the computation

$$\begin{aligned}
\mathcal{L}_I^{\mathrm{BB}} = {} & ig\cos\theta_W \Big[(W_\alpha^\dagger W_\beta - W_\beta^\dagger W_\alpha)\partial^\alpha Z^\beta + (\partial_\alpha W_\beta - \partial_\beta W_\alpha) W^{\dagger\beta} Z^\alpha \\
& - (\partial_\alpha W_\beta - \partial_\beta W_\alpha^\dagger) W^\beta Z^\alpha \Big] \\
& + ie\Big[(W_\alpha^\dagger W_\beta - W_\beta^\dagger W_\alpha)\partial^\alpha A^\beta + (\partial_\alpha W_\beta - \partial_\beta W_\alpha) W^{\dagger\beta} A^\alpha + (\partial_\alpha W_\beta^\dagger - \partial_\beta W_\alpha^\dagger) W^\beta A^\alpha \Big] \\
& + g^2 \cos^2\theta_W \Big[W_\alpha W_\beta^\dagger Z^\alpha Z^\beta - W_\beta W^{\dagger\beta} Z_\alpha Z^\beta \Big] \\
& + e^2 \Big[W_\alpha W_\beta^\dagger A^\alpha A^\beta - W_\beta W^{\dagger\beta} A_\alpha A^\alpha \Big] \\
& + eg\cos\theta_W \Big[W_\alpha W_\beta^\dagger (Z^\alpha A^\beta + A^\alpha Z^\beta) - 2 W_\beta W^{\dagger\beta} A_\alpha Z^\alpha \Big] \\
& + \frac{1}{2} g^2 W_\alpha^\dagger W_\beta \Big[W^{\dagger\alpha} W^\beta - W^\beta W^{\dagger\beta} \Big]
\end{aligned} \tag{1.43}$$

$$\mathcal{L}_I^{\mathrm{HB}} = \frac{1}{2} v g^2 W_\alpha^\dagger W^\alpha \sigma + \frac{1}{4} g^2 W_\alpha^\dagger W^\alpha \sigma^2 + \frac{v g^2}{4\cos^2\theta_W} Z_\alpha Z^\alpha \sigma + \frac{g^2}{8\cos^2\theta_W} Z_\alpha Z^\alpha \sigma^2 \tag{1.44}$$

$$\mathcal{L}_I^{\mathrm{HH}} = -\lambda v \sigma^3 - \frac{1}{4}\lambda\sigma^4 \tag{1.45}$$

The physical $W^\pm$ boson's coupling constant, g, is related with g_W by

$$g = 2\sqrt{2} g_W \tag{1.46}$$

By summing both chirality components, retrieving the fermions' complete Dirac field, we can consider the remaining two terms of the Lagrangian ($\mathcal{L}_L$ and $\mathcal{L}_{\mathrm{LH}}$) as

$$\mathcal{L}_L + \mathcal{L}_{\mathrm{LH}} = \overline{\psi}_l (i\partial\!\!\!/ - m_l)\psi_l + \overline{\psi}_{\nu_l}(i\partial\!\!\!/ - m_{\nu_l})\psi_{\nu_l} + \mathcal{L}_I^{\mathrm{LB}} + \mathcal{L}_I^{\mathrm{LH}} \tag{1.47}$$

Where additional non-interaction terms appear

$$\begin{aligned}
\mathcal{L}_I^{\mathrm{LB}} = {} & e\overline{\psi}_l \gamma^\alpha \psi_l A^\alpha - \frac{g}{2\sqrt{2}} \Big[\overline{\psi}_{\nu_l} \gamma^\alpha (1-\gamma_5)\psi_l W_\alpha + \overline{\psi}_l \gamma^\alpha (1-\gamma_5)\psi_{\nu_l} W_\alpha^\dagger \Big] \\
& - \frac{g}{4\cos\theta_W} \overline{\psi}_{\nu_l} \gamma^\alpha (1-\gamma_5)\psi_{\nu_l} Z_\alpha + \frac{g}{4\cos\theta_W} \overline{\psi}_l \gamma^\alpha (1 - 4\sin^2\theta_W - \gamma_5)\psi_l Z_\alpha
\end{aligned} \tag{1.48}$$

$$\mathcal{L}_I^{\mathrm{HL}} = -\frac{1}{v} m_l \overline{\psi}_l \psi_l \sigma - \frac{1}{v} m_{\nu_l} \overline{\psi}_{\nu_l} \psi_{\nu_l} \sigma \tag{1.49}$$

The mass terms m_l and m_{ν_l} follow from imposing standard Dirac mass terms, they read

$$m_l = v g_l / \sqrt{2} \qquad m_{\nu_l} = v g_{\nu_l} / \sqrt{2} \tag{1.50}$$

It is interesting to note, how the coupling constants of the Higgs field with fermions depends on their mass.

We now have all the pieces of the Lagrangian density, after symmetry breaking. They can be summarized as follow

$$\boxed{\mathcal{L}_{\text{EW}}^{\text{broken}} = \mathcal{L}_0 + \mathcal{L}_{\text{I}}} \tag{1.51}$$

$\mathcal{L}_0$ and $\mathcal{L}_{\text{I}}$ being the *free* and *interacting* parts of the Lagrangian, respectively

$$\boxed{\begin{aligned}\mathcal{L}_0 =& \overline{\psi}_l \left(i\partial\!\!\!/ - m_l\right) \psi_l + \overline{\psi}_{\nu_l} \left(i\partial\!\!\!/ - m_{\nu_l}\right) \psi_{\nu_l} \\ & - \frac{1}{4} F^{\mu\nu} F_{\mu\nu} \\ & - \frac{1}{2} F^{\dagger}_{W\mu\nu} F_W^{\mu\nu} + m_W^2 W_\mu^\dagger W^\mu \\ & - \frac{1}{4} Z_{\mu\nu} Z^{\mu\nu} + \frac{1}{2} m_Z^2 Z_\mu Z^\mu \\ & + \frac{1}{2} (\partial^\mu \sigma)(\partial_\mu \sigma) - \frac{1}{2} m_H^2 \sigma^2\end{aligned}} \tag{1.52}$$

$$\boxed{\mathcal{L}_I = \mathcal{L}_I^{\text{LB}} + \mathcal{L}_I^{\text{BB}} + \mathcal{L}_I^{\text{HH}} + \mathcal{L}_I^{\text{HB}} + \mathcal{L}_I^{\text{HL}}} \tag{1.53}$$

Spontaneous symmetry breaking generated the new interaction terms as well as the mass terms for the corresponding particles. All the new mass parameters, given in (1.42) and (1.50), have a univocal and consistent relation with the original parameters

$$g_W, g_B, -\mu^2, \lambda, g_l, g_{\nu_l} \tag{1.54}$$

One can now use three well known experimental quantities to derive the mass of the W and Z bosons. These are: the fine structure constant

$$\alpha = \frac{e^2}{4\pi} = \frac{1}{137.04} \tag{1.55}$$

The Fermi coupling constant, which from IVB theory of muon's decay [56], is defined as

$$G = \sqrt{2} \left(\frac{g_W}{m_W} \right)^2 = 1.166 \times 10^{-5} \text{GeV}^{-2} \tag{1.56}$$

And finally, from neutrino scattering experiments [23], it is possible to get a value for the mixing angle

$$\sin^2 \theta_W = 0.252 \pm 0.030 \tag{1.57}$$

Combining (1.42), (1.55) and (1.56) one can write the bosons mass as functions of the experimental parameters

$$\begin{aligned} m_W &= \left(\frac{\alpha\pi}{G\sqrt{2}} \right)^{1/2} \frac{1}{\sin \theta_W} & \qquad m_Z &= \left(\frac{\alpha\pi}{G\sqrt{2}} \right)^{1/2} \frac{2}{\sin 2\theta_W} \\ m_W &= 78.3 \pm 2.4 \quad \text{GeV} & m_Z &= 89.0 \pm 2.0 \quad \text{GeV} \end{aligned} \tag{1.58}$$

These are the *bare* masses of the free part of the Lagrangian. In order to compute the physical masses, radiative corrections of order α have to be included. To do so, it is necessary to delve into the concept of *renormalization*, which goes beyond the scope of this study.

Nevertheless, the renormalized masses are shown

$$m_W^{\text{ren}} = 83.0 \pm 2.8 \quad \text{GeV} \qquad m_Z^{\text{ren}} = 93.8 \pm 2.3 \quad \text{GeV} \tag{1.59}$$

Which seem to be in relatively good agreement with experimental values [50] for the bosons mass

$$m_W^{\text{exp}} = 80.385 \pm 0.015 \quad \text{GeV} \qquad m_Z^{\text{exp}} = 91.1876 \pm 0.0021 \quad \text{GeV} \tag{1.60}$$

This is a key comparison to validate the theory. The assumption that the Higgs field has hypercharge $Y = 1/2$ is in agreement with experiment.

We are left with one unknown parameter, namely λ. Hence, the Higgs mass cannot be theoretically computed, we have

$$m_H^0 = \sqrt{-2\mu^2} = \sqrt{2v^2\lambda} \tag{1.61}$$

Since the theory is renormalizable, due to the Higgs self-interacting terms, a minimum and a maximum mass value can be estimated based on the correct previsions of the theory in its lowest-order.

Nonetheless, it is still completely left for experiment to discover the true value.

This feat was accomplished in 2012, when CERN detected a new scalar particle compatible with the Higgs of this model. Ever since the discovery, its properties have been studied thoroughly and today the most precise value of its mass is

$$m_H^{\text{exp}} = 125.09 \pm 0.21 \tag{1.62}$$

Which puts the last piece of the SM jigsaw into play.

1.3.2 Cross Section and Branching Ratios

The independent observation by ATLAS [4] and CMS [26] of a new particle that had characteristics that matched those of a scalar boson with mass of approximately 125 GeV triggered the discovery of the Higgs particle. It was first detected by its decay products: $\gamma\gamma$, WW, and ZZ bosons in 2012. Now its production methods and main decay chains are known and can be divided into several groups/categories [3]. The collision of pp is always assumed, hence, it is omitted.

For the production processes one has:

- Main production processes: H, qqH, VH.
- Associated production with heavy quarks: $t\bar{t}H$,$b\bar{b}H$, $c\bar{c}H$.
- Associated production with single top/bottom quark: tHq, WtH, btH, tH,bH.
- Pair/triple production: HH, $qqHH$, VHH, $ttHH$.
- Associated production with a gauge boson and two jets: $qqHV$.
- Gauge boson scattering: $WW \to WW$, $WW \to HH$, etc.
- Rare processes: $qq \to H\gamma$, $t \to cH$.

The cross section, for the main processes, as a function of the CM energy is shown in Figure 1.7. The associate production of top quarks with Higgs bosons has one of the lowest cross sections and was not discovered so far. The reason why it is so interesting relies on the fact that this channel allows a direct measurement of the top quark Yukawa couplings to the Higgs boson.

As the mass discovered is 125 GeV, one expects the Higgs to decay [32] around

- 60% of the times into $b\bar{b}$ pairs.
- 21% into WW pairs.
- 9% into two gluons.

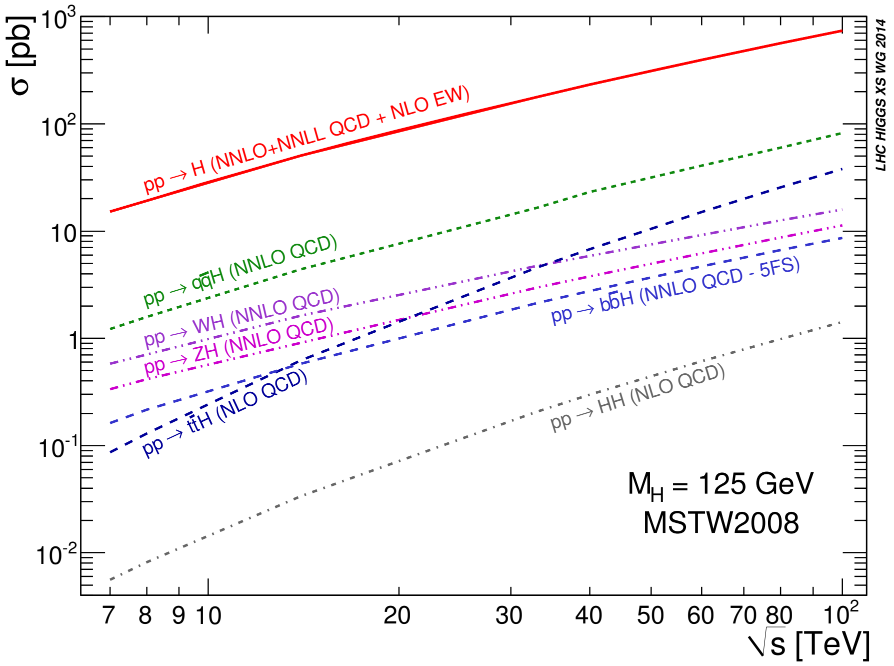

FIGURE 1.7: Run of the theoretical Higgs cross section values vs. the CM energy of the protons collision for several production modes [42]. The Higgs mass is assumed to have a pole mass of 125 GeV.

- 5% into $\tau\bar{\tau}$ pairs.
- 2.5% into $c\bar{c}$ pairs.
- 2.5% into ZZ pairs.
- 0.2% into $\gamma\gamma$.
- 0.15% into γZ.

In the WW and ZZ cases at least one of the gauge bosons will have a highly off-shell mass, since these are constrained by the pole values of the Higgs and gauge bosons masses.

1.3.3 Yukawa couplings for Quarks

To simulate Higgs events one needs to write down the full coupling to all the particles in the Lagrangian in order to have its full dynamics. This means including quarks to the expression derived (1.37). This can also be accomplished by Yukawa couplings [53], in analogy with leptons.

With leptons the process is rather simple. With quarks, an additional symmetry related with *colour* freedom has to be taken into consideration, as well as quark mixing through W bosons interaction. This forces the Higgs-Quark[13] interaction term to be of the form

$$\mathcal{L}_{HQ} = Y^d_{ij}\overline{Q}'^L_i(x)d'^R_j(x)\Phi(x) + Y^u_{ij}\overline{Q}'^L_i(x)u'^R_j(x)\tilde{\Phi}(x) + \text{h.c.} \tag{1.63}$$

where $Q'^L_i = (u'^L_i, d'^L_i)^T$ is a left-handed weak isospin doublet composed of up-like and down-like *interacting* quarks (Dirac fermions). The u'^R_i and d'^R_i fields are the right-handed isospin singlets counterparts[14].

---

[13] It is interesting to note that quark mixing happens through Higgs interaction above the electroweak unification threshold.

[14] Implicit summation is through families in the interaction basis.

The $\tilde{\Phi}(x)$ field follows the definition (1.36). The complex matrices $Y^{d/u}$ correspond to transition amplitudes from the state $|j, R\rangle$ to $|i, L\rangle$ and vice-versa, due to the hermitian conjugate term.

To retrieve back standard interaction terms and the physical quark fields, below the electroweak threshold, one has to diagonalize the coupling matrices

$$K_{ij}^{d/u} = (V^{d/u})_{im}(Y^{d/u})_{mn}(V^{\dagger d/u})_{nj} \tag{1.64}$$

where V^d, V^u are unitary matrices that diagonalize Y^d, Y^u, respectively, by a similarity transformation. The spontaneously broken Higgs-Quarks interaction becomes

$$\begin{aligned} \mathcal{L}_{HQ}^{\text{broken}} &= K_j^d \overline{d}_j^L(x) d_j^R(x)\sigma(x) + K_j^u \overline{u}_j^L(x) u_j^R(x)\sigma(x) + \text{h.c.} \\ &= g_i^q \overline{\psi}_i^L(x)\psi_i^R(x)\sigma(x) + \text{h.c.} \end{aligned} \tag{1.65}$$

with K_j^d and K_j^u being the diagonal terms of the diagonal coupling matrix K_{ij}^d and K_{ij}^u, respectively.

The new coupling g_j^q incorporates both $K_{ij}^{d/u}$ into one. If there is no distinction between u or d quarks the index accommodates the **flavour** information. The constant terms in $\sigma(x)$ will be the new mass terms for the quarks and are not included in the interaction term.

Notice how the primes have dropped. The new fields $\psi^{R/L}(x)$ are the *physical* quarks and they are relate to the interacting ones by

$$\begin{aligned} d_i^{R/L}(x) &= V_{ij}^d {d'}_j^{R/L}(x) \\ u_i^{R/L}(x) &= V_{ij}^u {u'}_j^{R/L}(x) \end{aligned} \tag{1.66}$$

These specific couplings are limited, since they just allows pure scalar interactions between the Higgs boson and quarks. Let us consider a CP violating Higgs-Quark coupling, by generalizing the previous Lagrangian. This comes at no cost in preserving local gauge invariance. It can be written as

$$\mathcal{L}_{HQ}^{\text{broken}} = g_i^q \overline{\psi}_i^L(x)(a_i + ib_i\gamma^5)\psi_i^R(x)\sigma(x) + \text{h.c.} \tag{1.67}$$

where a_i and b_i are the scalar and pseudo-scalar components, which in general depend on the quark flavour i.

Most often the sum of their square $(a_i^2 + b_i^2)$ is taken to be equal to unity. But in certain cases it is also considered the following generalization

$$a_i^2 + b_i^2 = k^2 \neq 1 \tag{1.68}$$

Since, as a first approach, the intention of this study is to start with the limit cases of pure scalar and pure pseudo-scalar Higgs, one sets the constants for $h = H$ (scalar) as

$$a_t = 1 \qquad\qquad b_t = 0 \tag{1.69}$$

and for $h = A$ (pseudo-scalar) as

$$a_t = 0 \qquad\qquad b_t = 1 \tag{1.70}$$

where $i = t$ the top quark, since it is the focus of this thesis.

The core of this study is to develop a multivariate analysis to create sensitive variables for each point in the spectrum of possibilities for this coupling. As such, several samples with different coupling values of a_i and b_i will be generated.

Having sensitive variables for each possibility will allow a direct comparison with LHC data. Therefore, enabling one to affirm on the true nature of the coupling.

Chapter 2

The Large Hadron Collider (LHC)

On April 5th, 2015, the LHC re-opened after a long period of two years of upgrades with a test run that reached 6.5 TeV per beam, a total of 13 TeV at a CM frame. This marked the beginning of the LHC run 2.

2.1 The LHC experiments

The LHC, Large Hadron Collider, built by CERN - European Organization for Nuclear Research, in collaboration with thousand of scientists and engineers from around the world, is the world's largest, most complex man-made experimental facility and the most powerful particle collider, reaching energy values of the order of the *tera* electron volt. It is a circular synchrotron-type hadron and ion collider with a perimeter of almost 27 km in a tunnel of around 175 m deep. The whole complex is located at the Franco-Swiss border near Geneva, Switzerland. The LHC main purpose is to probe new energy regimes in order to experimentally validate predictions of different fields in theoretical physics, namely particle and high-energy physics.

To that end, the LHC is divided into seven interaction points where beams cross or collide with targets, where the following experiments are located:

- The **ATLAS** experiment (A Toroidal LHC Apparatus) [1], is one of the large, general purpose detectors, along with CMS. It is focused on using the high-energy capacity of the LHC to validate predictions from the SM and others theories, with the study of the Higgs physics at its core.

- The **CMS** experiment (Compact Muon Solenoid) [25], is the other large, general purpose detector, which like the ATLAS experiment is dedicated into exploring beyond the previous attainable energies. ATLAS and CMS work as independent experiments with different teams for unbiased experimental results. Both made discoveries of a scalar particle with a mass of around 125 GeV which gave the confirmation of the discovery of the Higgs boson in 2012.

- The **ALICE** experiment (A Large Ion Collider Experiment) [6], is dedicated in studying quark-gluon plasma using mainly Pb-Pb collision. It is believed that this state of matter was one of the first primordial states after the Big Bang and may shed light into key problems of QCD (Quantum Chromodynamics), namely colour confinement, chiral symmetry restoration, among others.

- The **LHCb** experiment (LHC beauty) [7], is dedicated to the study of *b-physics*, which focus on, but not limited to, the study of CP violation on b-hadrons, branching ratios of the b-quark/hadrons decays and also electroweak interactions. Its main purpose is to look for clues for the matter-antimatter asymmetry in the universe.

- The **TOTEM** experiment (TOTal Elastic and diffractive cross section Measurement) [12], aims to measure total cross sections, elastic scattering and diffractive processes. It shares the intersection point of CMS.

- The **LHCf** experiment (Large Hadron Collider forward) [59], is a special-purpose astroparticle physics apparatus. It is located at the intersection point of the ATLAS experiment. It detects beams which are aligned with the beam pipe (at collision point). In particular, it studies the development of π^0 production in general collisions at ATLAS. This in turn will complement the other high energy measurements from observatories like Pierre Auger, in Argentina, and the Telescope Array Project, in the United States.
- The **MoEDAL** experiment (Monopole and Exotics Detector At the LHC) [52], is dedicated into finding exotic particles like magnetic monopoles, dyons and highly ionizing massive particles. Exotic particles like dyons are predicted by some grand unifying theories.

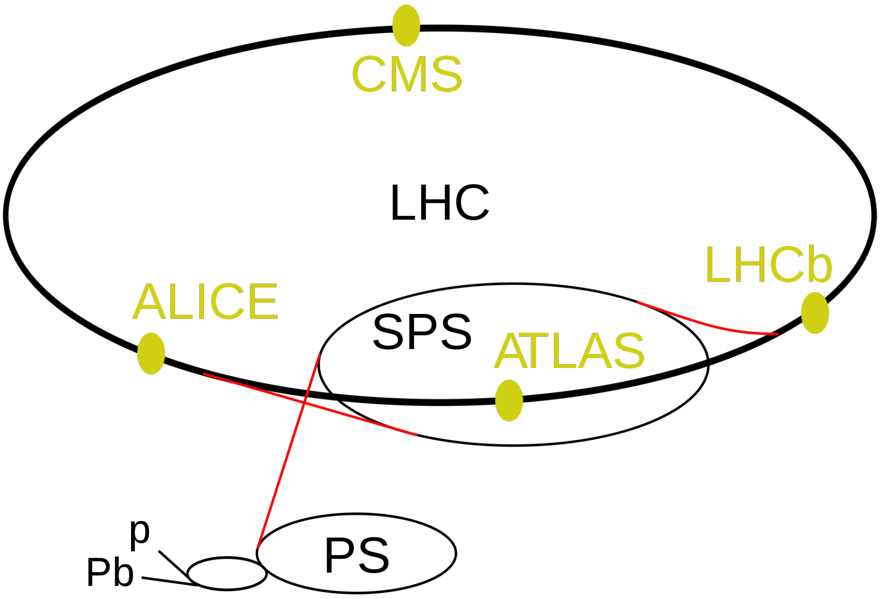

FIGURE 2.1: LHC structure and its four main experiments in yellow. The sections outside the main LHC regions are accelerators and synchrotrons. [REF]

2.2 The ATLAS Experiment

With the discovery of the Higgs Boson in 2012, its properties can be further studied. CP violation remains one of the core aims, since it would explain the matter and anti-matter asymmetry in the universe. New physics is also being investigated, specially broken supersymmetry since almost all string theories point out for new highly massive particles that can be obtained on this new energy regime.

This thesis will focus on events generated at the LHC which go through a fast simulation of a typical LHC experiment like ATLAS. Signal events, with different CP-even or CP-odd components of the Higgs couplings to top quarks are tested through angular distributions, that later can be probed with real data by ATLAS. Table 2.1 shows the general performance goals of the ATLAS detector [1].

2.2.1 The ATLAS detector

The ATLAS detector consists of a series of ever-larger concentric cylinders around the interaction point where the proton beams from the LHC collide. It can be divided into four major parts:

Detector component	Required resolution	η coverage	
		Measurement	Trigger
Tracking	$\sigma_{p_T}/p_T = 0.05\% p_T \oplus 1\%$	±2.5	
EM calorimetry	$\sigma_E/E = 10\%/\sqrt{E} \oplus 0.7\%$	±3.2	±2.5
Hadronic calorimetry (jets)			
barrel and end-cap	$\sigma_E/E = 50\%\sqrt{E} \oplus 3\%$	±3.2	±3.2
forward	$\sigma_E/E = 100\%\sqrt{E} \oplus 10\%$	$3.1 < \lvert\eta\rvert < 4.9$	$3.1 < \lvert\eta\rvert < 4.9$
Muon spectrometer	$\sigma_{p_T}/p_T = 10\%$ at $p_T = 1$ TeV	±2.7	±2.4

TABLE 2.1: General performance goals of the ATLAS detector [1]. The units of energy (E) and transverse momentum (p_T) are in GeV. The symbol $\oplus$ means a sum in quadrature.

the Inner Detector, the calorimeters, the Muon Spectrometer and the magnet systems. Each of these is in turn made of multiple layers. The detectors are complementary: the Inner Detector tracks charged particles precisely, the calorimeters measure the energy of easily stopped charged particles, and the muon system makes additional measurements of highly penetrating muons. The two magnet systems bend charged particles in the Inner Detector and the Muon Spectrometer, allowing their momenta to be measured.

The only established stable particles that cannot be detected directly are neutrinos; their presence is inferred by measuring a momentum imbalance among detected particles. For this to work, the detector must be "hermetic", meaning it must detect all non-neutrinos produced, with no blind spots. Maintaining detector performance in the high radiation areas immediately surrounding the proton beams is a significant engineering challenge.

In the very forward region of the ATLAS experiment, the Forward Detectors complement the measurement by analysing elastic-scattering at very small angles to better identify the luminosity at the interaction point.

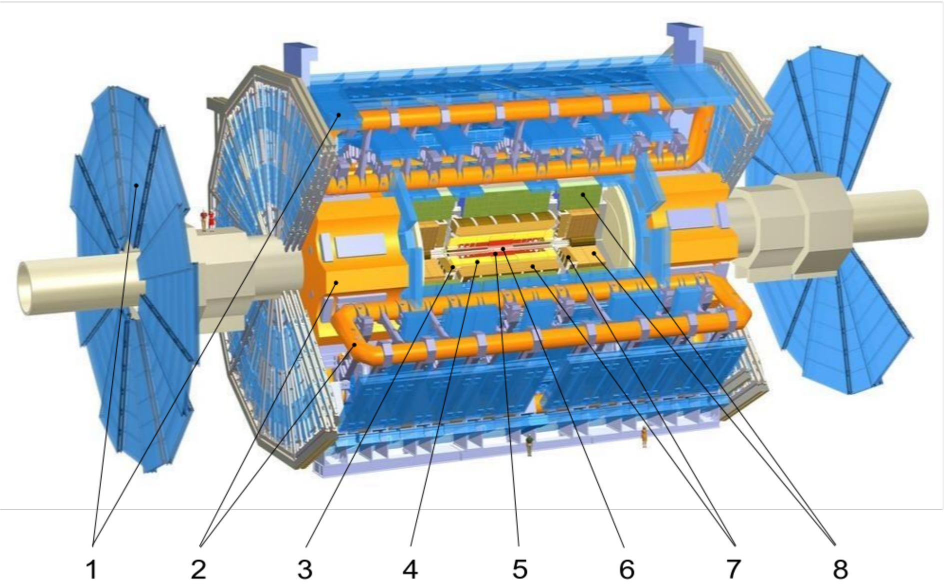

FIGURE 2.2: Computer generated cut-away view of the ATLAS detector [61] showing its various components: (1) Muon Detectors. **Magnet system:** (2) Toroid Magnets, (3) Solenoid Magnet. **Inner Detector:** (4) Transition Radiation Tracker, (5) Semi-Conductor Tracker, (6) Pixel Detector. **Calorimeters**: (7) Liquid Argon Calorimeter, (8) Tile Calorimeter.

Inner Detector

The Inner Detector [48] begins a few centimeters from the proton beam axis, extending to a radius of 1.2 meters. It is 6.2 meters in length along the beam pipe. Its basic function is to track charged particles by detecting their interaction with material at discrete points, revealing detailed information about the types of particles and their momentum [2].

The magnetic field surrounding the entire inner detector causes charged particles to curve, the direction of the curve reveals a particle's charge and the degree of curvature reveals its momentum.

The starting points of the tracks yield useful information for identifying particles, for example, if a group of tracks seem to originate from a point other than the original protonproton collision, this may be a sign that the particles came from the decay of a hadron with a bottom quark.

The Inner detector is composed of three sub-detectors. The Pixel Detector [40], the innermost part, contains three concentric layers and three disks on each end-cap, with a total of 1,744 modules, each measuring 2 cm $\times$ 6 cm. The detecting material is 250 μm thick silicon. Each module contains 16 readout chips and other electronic components.

The smallest unit that can be read out is a pixel (50μm $\times$ 400 μm). There are roughly 47,000 pixels per module. The minute pixel size is designed for extremely precise tracking, very close to the interaction point. In total, the Pixel Detector has over 80 million readout channels, about 50% of the number of channels of the whole experiment. Having such a large count created a considerable design and engineering challenge.

Another challenge was the radiation to which the Pixel Detector is exposed because of its proximity to the interaction point, requiring that all components be radiation hardened in order to continue operating after significant exposures.

The Semi-Conductor Tracker (SCT) [5], is the middle component of the inner detector. It is similar in concept and function to the Pixel Detector but with long, narrow strips rather than small pixels, making coverage of a larger area. Each strip measures 80 μm $\times$ 12 cm. The SCT is the most critical part of the inner detector for perpendicular beam tracking, since it measures particles over a much larger area than the Pixel Detector, with more sampled points and roughly equal (albeit one-dimensional) accuracy. It is composed of four double layers of silicon strips, has 6.3 million readout channels and a total area of 61 square meters.

The Transition Radiation Tracker (TRT) [46], the outermost component of the inner detector, is a combination of a straw tracker and a transition radiation detector. The detecting elements are drift tubes (straws), each 4 mm in diameter and up to 144 cm long. The uncertainty of track position measurements (position resolution) is about 200 μm. Not being as precise as the other two detectors, it was necessary to reduce the cost of covering a larger volume.

The straws work by filling them with gas that becomes ionized when a charged particle passes through. The straws are held at about -1.5 kV, driving the negative ions to a fine wire down the centre of each straw, producing a current pulse (signal) in the wire. The wires with signals create a pattern of *hit* straws that allow the path of the particle to be determined. Between the straws, materials with widely varying indices of refraction cause ultra-relativistic charged particles to produce transition radiation and leave signal, with varying strength, in the straws. Xenon and argon gas is used to increase the number of straws with strong signals. The amount of transition radiation is greatest for highly relativistic particles. Also, particles have a higher speed the lighter they are, for a fixed energy. This means that particle can be identified from the signal strength of its path. Very strong signals are electrons(positrons), weaker signals could be (anti)muons or (anti)taus. The TRT has about 298,000 straws in total.

Calorimeters

The calorimeters [31] are situated outside the solenoid magnet that surrounds the Inner Detector. Their purpose is to measure the energy from particles. There are two basic calorimeter systems: an inner electromagnetic calorimeter and an outer hadronic calorimeter. Both are sampling calorimeters, they absorb energy in high-density material and periodically sample the shape of the resulting particle shower, inferring the energy of the original particle from this measurement.

The electromagnetic calorimeter absorbs energy from particles that interact electromagnetically. It has high precision, both in the amount of energy absorbed and in the precise location of the energy deposited. The barrel EM calorimeter has accordion shaped electrodes and the energy-absorbing materials are lead and stainless steel, with liquid argon as the sampling material. Around the EM calorimeters there is a cryostat to keep it sufficiently cool.

The hadronic calorimeter absorbs energy from particles that interact via the strong force. These particles are primarily hadrons. It is less precise, both in energy magnitude and in accuracy [41]. The energy-absorbing material is steel, with scintillating tiles that sample the energy deposited.

Many of the features of the calorimeter are chosen because of their cost/effectiveness ratio. The detector is large and comprises a huge amount of construction materials. The main part of the calorimeter, the tile calorimeter, is 8 meters in diameter and covers 12 metres along the beam axis. The far-forward sections of the hadronic calorimeter are contained within the forward EM calorimeter's cryostat and use liquid argon, as readout medium, while copper and tungsten are used as absorbers.

Muon Spectrometer

The Muon Spectrometer is an extremely large tracking system, consisting of two parts. A set of 1,200 chambers measuring with high spatial precision the muons' tracks and a set of triggering chambers with accurate time-resolution. The extent of this sub-detector starts at a radius of 4.25 meters, close to the calorimeters, out to the full radius of the detector, 11 meters.

It was designed to measure, standalone, the momentum of 100 GeV muons with 3% accuracy and of 1 TeV muons with 10% accuracy. It was vital to put together such a large detector because a number of interesting physical processes can only be observed if one or more muons are detected, and because the total energy of particles in an event could not be measured if the muons were ignored.

It functions similarly to the Inner Detector, with muons curving so that their momentum can be measured, albeit with a different magnetic field configuration, lower spatial precision, and a much larger volume. Also, very few particles of other types are expected to leave signals in the Muon Spectrometer.

It has roughly one million readout channels, and all the detector's layers sum to a total area of 12,000 square meters.

Magnetic System

The ATLAS detector uses two large superconducting magnet systems [60] to bend charged particles so that their momenta can be measured. The inner solenoid produces a 2 Tesla magnetic field surrounding the Inner Detector. This high magnetic field allows even very energetic particles to curve enough for their momentum to be determined, and its nearly uniform direction and strength allow measurements to be made very precisely. Particles with momenta below roughly 400 MeV will be curved so strongly that they will loop repeatedly in the field and most likely not be measured. However, this energy is very small compared to the energy released in each proton collision.

The outer toroidal magnetic field is produced by eight very large air-core superconducting barrel loops and two end-caps air toroidal magnets, all situated outside the calorimeters and within the muon system. This magnetic field extends in an area of 26m × 20m and it stores 1.6 gigajoules of energy. Its magnetic field is not uniform, because a solenoid magnet of sufficient size would be prohibitively expensive to build. It varies between 2 and 8 Tesla.

Chapter 3

Signal and Background Generation and Simulation

A study of the associated production of top quarks together with a Higgs boson at the LHC, is performed in this thesis, looking for a possible pseudo-scalar component of the top quark Yukawa coupling to the 125 GeV Higgs boson. Signal and background events were generated at a centre-of-mass energy of 13 TeV, at the LHC. Events were then passed through a fast simulation of a typical LHC experiment, in this case ATLAS, which incorporates the effects of realistic acceptances and resolutions.

The generated events described in this section are composed of particles which, at different stages of the Monte Carlo (MC) event history, are identified at parton level, associated to the production of partons immediately following proton-proton collisions, after showering, where QCD and QED radiation effects are taken into account, and after hadronization.

In the SM, the coupling of the Higgs boson to fermions is expected to become more significant with increasing fermion mass, which makes $t\bar{t}H$ production particularly interesting. This thesis will focus on the single lepton decay channel of $t\bar{t}H$ events, where one of the W bosons (originated from the parent top quark) decays leptonicaly and the other hadronically, while the Higgs boson is expected to decay through the dominant decay channel, into $b\bar{b}$. The final state topology includes four bottom and two light jets, a charged lepton and missing transverse energy from the undetected neutrino.

The particle state is the set of particles/objects that is detected/reconstructed after all possible processes of showering, hadronization and jet clustering happen, as consequence of the parton state and clustering algorithm. These include photons, jets and electrically charged leptons.

Gluon fusion and radiation, as well as hadronization are independent[1] QCD effects, which make it impossible to directly associate *particle* states with their original parton counterparts. This makes up the *irreducible* background. For instance, an event where $X = tZ^0$ might generate the same final particle state of a $X = t\bar{t}H$ event.

Consequently, not only it is necessary to generate what is called signal events, that include collisions where a $t\bar{t}H$ vertex exists, but also to generate all other processes that can have the same *particle* state. This will enable performance studies on variables to discern signal events from backgrounds.

Naturally, only single lepton *particle* level states are considered as well, and thus one, and only one, charged lepton must be present. Additionally, it is only accepted events with at least six jets, maintaining in this way the one-to-one correspondence criteria[2].

3.1 Higgs Signals

One of the main goals of this study is to have the capacity to detect signal events, thus signal events have to be generated for the present analysis. Since it is considered a generalization of the

---

[1] Not dependent on the parton level state.

[2] A jet can only be associated with one parton and vice-versa.

Standard Model Higgs coupling to top quarks given in equation (1.67), several signal samples are necessary. Since it is considered that $a_t^2 + b_t^2 = 1$ only one parameter (α) is necessary to unambiguously define the coupling parameters

$$\begin{aligned} a_t &= \sin\alpha \\ b_t &= \cos\alpha \end{aligned} \tag{3.1}$$

The two extreme cases are generated. The scalar Higgs ($h = H$) where $a_t = 1$ and the fully CP violating Higgs ($h = A$) where $b_t = 1$.

3.2 The Standard Model Background

Let us quantify the types of topologies that can add up to the background of this study. Figure 3.1 describes the results obtained by ATLAS [28] at $\sqrt{13}$ TeV for the single lepton channel. It accounts for the different types of event topologies, identified according to the number of lights jets and b jets.

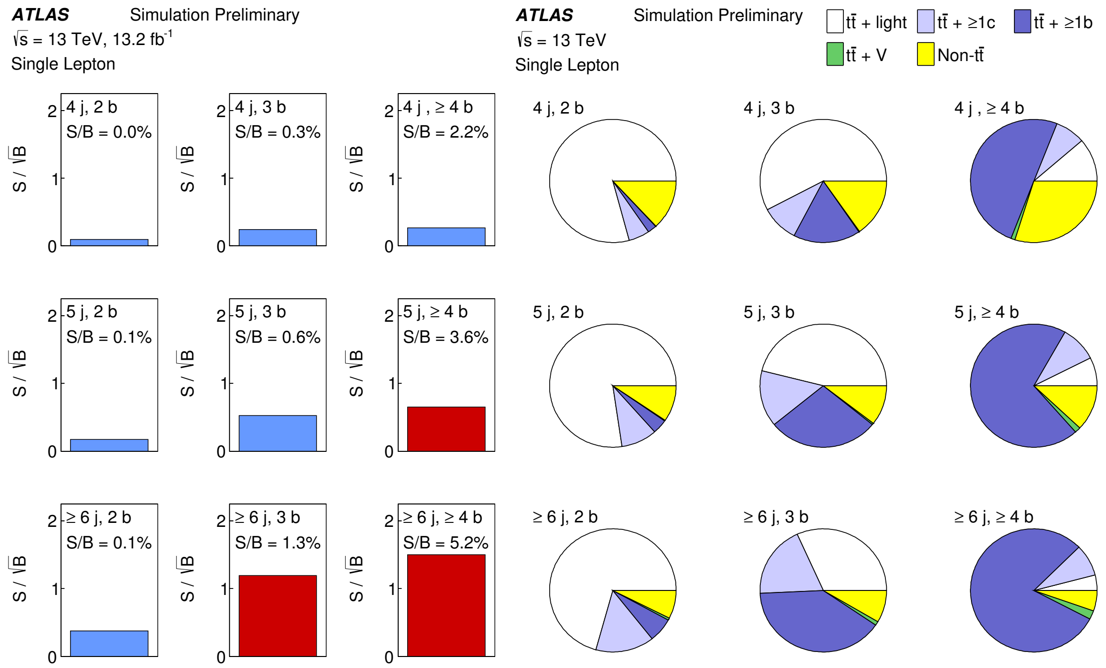

(A) (B)

FIGURE 3.1: Analysis regions for the single-lepton channel for different particle states. Each row corresponds to a different jet multiplicity, while each column corresponds to a different b-jet multiplicity. The signal/background, $S/\sqrt{B}$ and S/B, ratios for each of the regions are shown in (A) [15]. Signal regions are shaded in red, while the control regions are shown in blue. In (B) [14], it is shown the fractional contributions of various parton states to the particle states. These parton states include top pairs produced in association to light quarks, c-, b- quarks or $V = \gamma, g, W^{\pm}, Z^0$, as well as, non- top pair production.

The control regions used for background normalization (in blue) have a fairly weak signal to background ratio. On the other hand, signal enriched regions, where bigger values of signal over background ratios are clearly observed (in red), can be used in the analysis. These include the cases where 5 or more jets (of which at least 4 are b tagged) are present and where 6 or more jets (of which at least 3 are b tagged) are present. The topology where at least 6 jets (of which at least 3 are b tagged) is used for analysis. In any case, the majority of the background is of the form $X = t\bar{t} + \geq 1b$. Since the Higgs boson is expected to decay mainly to a *botton* quark pair [32], the

dominant background is

$$X = t\bar{t}b\bar{b} \tag{3.2}$$

3.3 Event Generation

Each topology has its own characteristics and details but all of them have to go through the same procedure in order to be generated. The process of generating events is accomplished by the `Madgraph5_aMC@NLO` [8] package with the `NNPDF2.3` PDF sets [17] and others packages that complement the generation.

It was chosen `Madgraph5_aMC@NLO` since it provides a framework for BSM simulations, as well as NLO corrections for QCD processes. Furthermore, it provides standard output for most analysis packages.

The generation of events can be summed up in the following:

1. Model Selection: this is where a Lagrangian is inputed. For the background signal: the full SM Lagrangian is considered by using the `sm` model. For Higgs production: The generalization of the SM coupling of the Higgs to fermions, from chapter 1, is considered. This is done by using the `HC_NLO_X0` model [13].

2. Specifying an event: Generate random events of X by Monte-Carlo methods. In turn, the events are reweighted considering their matrix element $|\mathcal{M}|^2$. Rather than analytically computing the $2 \to N$ master scattering formula, given by

$$d\sigma = \frac{1}{2s}\prod_{i=1}^{N} d\Pi_i (2\pi)^4 \delta^{(4)}\left(p_A + p_b - \sum_i p_i\right) \cdot |\mathcal{M}|^2, \qquad d\Pi_i = \frac{d^3\mathbf{p}_i}{(2\pi)^3}\frac{1}{2E_i} \tag{3.3}$$

   the whole phase space spectrum is evenly sampled. A cut is done according to the relative weight of $|\mathcal{M}|^2$. This is the hard-scattering *parton* level with energies of the order of $\sim$ 100 GeV, and distances of $\sim 10^{-16}$ cm.

3. Particles decays: The first decays of the generated partons are going to be computed by adopting spin correlations using `MadSpin` [10]. The top quarks are *forced* to decay into W bosons and b quarks. The W bosons originated from the top quarks are decaying hadronically and leptonically, respectively. The Higgs boson is set to decay to every possibility within the selected model. The set of particles obtained up until now constitutes the **Monte-Carlo (MC) generator level particle set**.

4. Showering and Hadronization: The last step before detector simulation is generating the known process of showering and hadronization that happens for $E \sim 1$ GeV and typical distances of $\sim 10^{-14}$ cm. This step is implemented using the `Pythia6Q` [57] package.

5. Jet Clustering: From the previous step, one ends up with a dramatic increase in number of particles. These come in bunches, leave a multitude of charged tracks on the detector and are not convenient to treat individually. A method is employed that correlates the detected tracks into their respective bunch, called jets. The `FastJet` [20] package is used to implement an anti-kt algorithm [21].

6. Detector's simulation: This is accomplished by implementing the `Delphes` [35] package, which simulates a general detector. A card with the complete set of characteristics of the ATLAS detector (appendix B) is fed to the `Delphes` package. The particles that are detected compose the *particle* level set. The `Delphes` *particles/information* is defined as the *simulated particle* level set of objects.

There are two steps in this procedure that deal with parton radiation and described it differently, namely, the Monte-Carlo (with `MadSpin`) generation and `Pythia6` package for hadronization and showering. Thus, in order to avoid phase-space overlap from these different descriptions in multijet events, a matching procedure is done in the `MLM` scheme [9], which rejects phase-space overlapped events.

Table 3.1 summarizes the information on the generated samples.

Process	QCD order	# Jets	Enabled decays	$\sigma \times$ BR (pb)	# Events
$t\bar{t}H$	NLO	0	$H \to$ all, $t\bar{t} \to$ semileptonic	0.138	1040043
$t\bar{t}A$	NLO	0	$A \to$ all, $t\bar{t} \to$ semileptonic	0.058	645838
$t\bar{t}b\bar{b}$	NLO	0	$t\bar{t} \to$ semileptonic	4.708	1048095
$t\bar{t}+$ jets	LO	3	$t\bar{t} \to$ semileptonic	239.364	166361
$t\bar{t}V+$ jets	LO	1	$t\bar{t} \to$ semileptonic, $V \to$ all	0.324	339865
Single top	LO	0	$t \to$ leptonic	49.055	980000
$W+$ jets	LO	4	$W \to$ leptonic	34500	335224
$Wb\bar{b}+$ jets	LO	2	$W \to$ leptonic	289	311101
$VV+$ jets	LO	3	$V \to$ all	133.1	538138

TABLE 3.1: Generated event samples. For each sample, the table lists the order in QCD at which the sample was generated, the maximum number of additional light-flavoured jets allowed in the production, the enabled decays in `MadSpin`, and the product of cross-section and branching ratio returned by `MadGraph5`. The multi boson reference $V = W, Z$. The cross sections for the top single- and pair production are scaled to the most accurate theoretical results available [30], [19]. Leptonic decays include only electrons and muons, and exclude taus.

3.4 The DELPHES simulation

The last step of the previous list is realizing a physical detector. All of them have limitations in their capabilities, thus reducing the phase space window available for data observation. The knowledge of a detector's behavior is essential to decipher the true data from an actual experiment.

`Delphes` simulates the response of a multi-purpose detector, composed of an inner tracker immersed in an uniform magnetic field, electromagnetic and hadronic calorimeters and a muon detection system. All are organized concentrically with cylindrical symmetry around the beam axis. The detector active volume, calorimeter segmentation and strength of the uniform magnetic field, which is directed along the beam axis, are parameters that can be set by the user. The `Delphes` package has in its library a standard parametrization of the ATLAS detector (appendix B).

It is not in the scope of this study to motivate all properties. Nonetheless, a general overview will be given. The leptons' charged tracks smearing will be given special focus in chapter 5, as it will be essential for event reconstruction.

3.4.1 Particle propagation

The first step of any detector's simulation is to propagate the particles resulting from the process at hand through the inner tracker. Charged particles describe helicoidal trajectories, which depend on their momentum and magnetic field strength. Neutral particles travel in straight lines. Particles are propagated until they reach a calorimeter cell.

3.4.2 Calorimeters

`Delphes` can implement two calorimeters: an electromagnetic one (ECAL) and an hadronic one (HCAL). These calorimeters are segmented in a cylindrical grid of patches (η, ϕ). The patch size can be defined by the user and can depend on η. Segmentation on ϕ is taken as uniform and the granularity is the same for ECAL and HCAL.

The fraction of the particle's total energy that is deposited in the ECAL and HCAL can be defined in the parameters f_{ECAL} and f_{HCAL}, respectively. By default, electrons and photons have $f_{\mathrm{ECAL}} = 1$ and hadrons $f_{\mathrm{HCAL}} = 1$. The exception are kaons and Λ particles which have $f_{\mathrm{ECAL}} = 0.3$ and $f_{\mathrm{HCAL}} = 0.7$. Neutrinos and muons do not deposit any energy in the calorimeters. These values are mere approximations and can be changed to more adequate values, depending on the experiment simulation.

ECAL and HCAL are equally segmented, a straight line coming from the interaction point crosses one ECAL cell and one HCAL cell covering precisely the same (η, ϕ) region. These pairs of cells are called calorimeter towers, and are used in the object reconstruction, together with tracks.

The detected energy in each tower is given by a sum over all particles traveling through that tower. Each particle has an ECAL and HCAL contribution. These are equal to the energy deposited in the corresponding calorimeter after the application of a smearing. For these smearings, the energy resolution used is a function of the particle total energy and η, which is different for each contribution.

3.4.3 Charged leptons and photons

Muons

For muons, the user can define a global reconstruction probability and momentum resolution, which is a function of the muon's p_T and η. The momentum measurement is obtained from a gaussian smearing of the original muon 4-momentum, according to the defined resolution. The muon's reconstruction efficiency is zero outside the tracker acceptance region and for muon momenta below a certain threshold, to avoid looping particles.

Electrons

Typical electron identification requires combining information from the tracking system and the calorimeter. `Delphes` avoids this necessity by parameterizing the electron's reconstruction efficiency as a function of energy and η. The electron's energy resolution is a combination of the tracker and the ECAL resolution, the tracker resolution dominates at low energy, while at high energy, the calorimeter resolution dominates. The electron's identification efficiency is null outside the track acceptance and below a certain energy threshold.

Photons

The reconstruction of photons relies solely on the ECAL. The final photon's energy is obtained from applying the ECAL resolution to the original photon. Photon conversion into a electron/-positron pair is neglected. Electrons with no reconstructed tracks that reach the ECAL are reconstructed as photons.

Currently, `Delphes` does not include a fake rate for electrons, muons or photons. The fake rate parameterizes the possibility of a certain object (for example, a jet) being misidentified as a lepton or photon. In physical analyses with multi-lepton final states, the lepton fake rates are important to correctly determine the expected contribution of each background process to the analysis yield. For a lepton or photon to be reconstructed, an isolation criterion must be met. The isolation variable I of a particle P is defined as the sum of the p_T of all particles with a p_T above a threshold p_T^{min} and within a cone of $\Delta R < R$ around that particle, normalized to the p_T of P. The particle is said to be isolated if the condition $I < I_{\text{min}}$ is verified. The default values of the parameters are $p_T^{\text{min}} = 0.1$ GeV, $R = 0.5$ and $I_{\text{min}} = 0.1$.

3.4.4 Particle-flow reconstruction

The particle-flow approach aims to obtain the best measurements, using information available from all subdetectors. In real experiments, the momentum of a charged particle can be estimated from the particle track or from the calorimeter. The preferred measurement depends on an energy threshold, below which the momentum resolution obtained from the track is better. Above the threshold, the calorimeter energy deposit is more reliable to estimate the momentum. In the particle-flow phase of the simulation, if a track exists for a certain particle, information from the track is always preferred.

The particle-flow algorithm creates two sets of 4-vectors, which will serve as input for the subsequent reconstruction of jets and MET. These 4-vectors include particle-flow tracks and particle-flow towers. A particle-flow track is created for every track in the inner tracker. In turn, for each calorimeter tower the energy deposits originating from particles with reconstructed tracks is subtracted. If the remaining energy E_{tower} is positive, a particle-flow tower is created with this energy and with the direction of the tower (η, ϕ) coordinates.

This definition implies that particle-flow tracks include charged particles, measured with good resolution, and that particle-flow towers include a combination of neutral particles, charged particles without a track, and excesses in deposits originating from the smearing process of the calorimeters, all measured with worse resolution. While very simple when compared to what is actually required in real experiments, this algorithm reproduces well the performance achieved at LHC experiments.

3.4.5 Jets

Jet reconstruction can be performed using one of three different collections of objects as input: the long-lived particles resulting from parton shower and hadronization, the calorimeter towers or the particle-flow tracks and particle-flow towers. `Delphes` integrates the `FastJet` package, making it possible to choose one among the most common jet clustering algorithms and setting the corresponding parameter values. A minimum p_T threshold for a jet to be stored in the final jet collection can also be set. In order to avoid double-counting, `Delphes` automatically removes jets which have already been reconstructed as leptons or photons.

3.4.6 b and τ jets

The algorithm for b and τ jet identification is purely parametric. A jet can potentially be identified as a b or τ candidate if its direction is within a certain ΔR cone relative to a generated b or τ , respectively. Given this condition, the probability for the jet to be identified as a b or τ will be given by user-defined parameterization of the tagging efficiency. A mis-tagging efficiency can also be introduced, leading to the realistic possibility that a particle other than b or τ can be identified as such.

3.4.7 b-Tagging

The following is applied to all the samples generated with `MadGraph5_aMC@NLO` and should be a realistic approximation on the efficiencies obtained at ATLAS. The misidentification rate of non b-jets reads

$$\mathcal{M}(P_t) = 0.002 + 7.3 * 10^{-6} P_t \tag{3.4}$$

For correctly b-tagging a b-jet, the efficiency parametrization reads

$$\mathcal{I}(P_t) = 0.80\tanh(0.003P_t)\left(\frac{30}{1+0.086P_t}\right) \tag{3.5}$$

The only factor that defines these rates is the transverse momenta of the jets. The b-tag identification rate is represented in Figure 3.2.

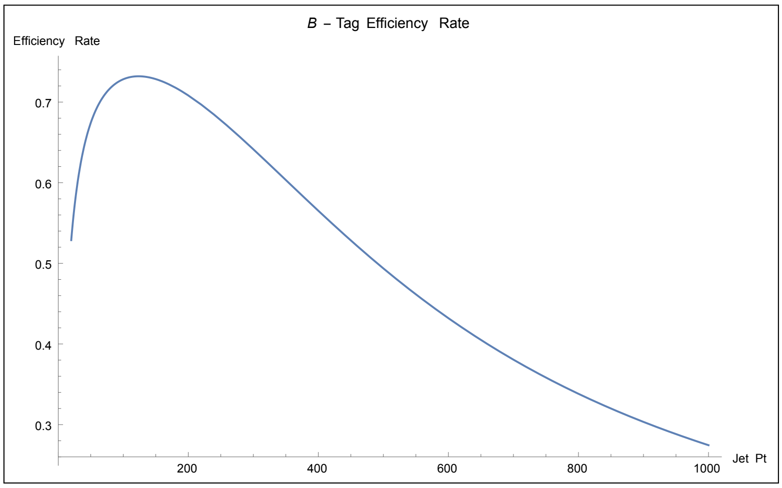

FIGURE 3.2: Identification efficiency of b-jets. It is plotted the efficiency rate vs. the transverse momentum of the b-jet to be tagged.

Chapter 4

Bayesian Approach for Reconstruction

A brief introduction is made in Bayesian analysis in order to introduce the Maximum Likelihood Estimate method. The MLE method is used in this study for event reconstruction and its implementation is based on the development made for the `KLFitter` package [34].

4.1 Bayesian Analysis

The field of Bayesian Analysis [36] consists of methods for making inferences from data by using probability models for observable and unknown quantities, which one wants to know about.

An essential characteristic of these methods is the probabilistic treatment to quantify uncertainties in inferences on statistical data analysis. Furthermore, these uncertainties can be updated as new data is available.

The process of Bayesian data analysis can be divided into the following steps:

1. Setting up a *full probability model*: this is a joint probability distribution for all observable and unobservable quantities in a problem. The model should be consistent with knowledge about the underlying scientific problem and the data collection process.

2. Conditioning on observed data: calculating and interpreting the appropriate *posterior distribution*, the conditional probability distribution of the unobserved quantities of interest, given the observed data.

3. Evaluating the fit of the model and the implications of the resulting posterior distribution: does the model fit the data, are the substantive conclusions reasonable, and how sensitive are the results to the modelling assumptions in step 1? If necessary, one can alter or expand the model and repeat the three steps.

In a typical event from a collider, one wants to know how probable it is for a given event to be the product of some physical process in question.

In turn, one also wants to estimate the parameters that define this physical process by means of the detectable data. Discerning posteriorly if this data was indeed generated by the process one is looking for.

4.1.1 Posterior Probability

As was mentioned in the first point of the previous list, the first step is establishing a full probability model that incorporates the observable set of variables $\{y_i\}$ and the set of parameters to be estimated $\{\theta_i\}$.

For the observable data, a likelihood function is considered. This is a probability density function of the data conditioned to the set of parameters to be estimated.

In this study, each measurable variable (4.8) is independent of each other. This is motivated by the fact that the detectable parameters of the jets, i.e. energy and momentum, depend only on the smearing effects of the detector and not on the specific properties of the other jets.

With this assumption, the likelihood $p(y|\theta)$ can be written as

$$p(y|\theta) = \prod_i p_i(y_i|\theta) \tag{4.1}$$

where $p(\cdot|\cdot)$ describes a conditional probability.

The *prior* density is probability density function of the parameters to be estimated, i.e. before any measurement is done. It is an initial and subjective choice of distribution for these parameters.

These assumptions can be considered either *informative* or *noninformative*. Generally, they correspond to making specific assumptions on these density functions or abstaining from doing so by starting with an equal and constant probability density function for each parameter, respectively.

The joint probability distribution can then be written as the product of the prior distribution $p(\theta)$ and the *sampling* distribution, the likelihood $p(y|\theta)$,

$$p(y, \theta) = p(\theta)p(y|\theta) \tag{4.2}$$

Let us introduces $p(y)$ as the *prior predictive* distribution, given by

$$p(y) = \int_\Theta p(\theta)p(y|\theta)d\theta \tag{4.3}$$

where Θ is the domain of θ. The integral should be replaced with a summation when θ is discrete.

This quantity is called *prior* because it does not depend on previous measurements and *predictive* because it is a density function of quantities that can be measured.

Using the simple property of conditional probability, known as Bayes' rule, the *posterior* density reads

$$p(\theta|y) = \frac{p(y, \theta)}{p(y)} = \frac{p(\theta)p(y|\theta)}{p(y)} \tag{4.4}$$

which gives the probability distribution of the set of parameters conditioned to the measured data.

This distribution can be used for different ends. For instance, one could take as true value the mean or median of the distribution, or one can simply be interested in knowing the probability of the parameters to be in a certain range, defining in this way *credibility* intervals.

For the present study, it is going to be considered a specific application of Bayes' analysis, which *ignores*, in a certain sense, the *prior* and *prior predictive* distributions.

4.2 Maximum Likelihood Estimation

The key point of the analysis developed in this study is to infer the generator level information, of a collision, from the measured data of the detected objects. This cannot be done in a straightforward way since the detectors are not perfect, i.e. they deviate/smear the particle's momentum and NLO effects are also present. In turn, the detection of more objects than gen particles might occur. Hence, some criteria has to come into play. Since these effects are expected to be stochastic, one can apply the concept of Maximum Likelihood Estimation (MLE) [45]. This method is not natively Bayesian but can be interpreted in a Bayesian scope, through (4.4).

In a Bayesian analysis one is concerned in computing the full (or approximate) *posterior* probability. This being a probability density function for the parameters to be estimated.

In contrast, the MLE is a point estimate. No information is injected about the *prior* distribution nor the evidence $p(y)$, these can be *ignored*. This is the case of the present study as the reconstruction algorithm is just concerned with *bridging* detectable jets with generator level objects. There is no need to know how probable it is for a generator level object to have a *specific* value. Rather, one only wants to know how *much* generator level particles deviate from the measured ones.

Being a point estimate method, the MLE gives the most probable solution, which will be considered the *de facto* solution. This solution globally maximizes the likelihood, and can be retrieved by solving

$$\hat{\theta} : \frac{\partial}{\partial \theta} L(y|\theta) = 0 \tag{4.5}$$

retaining only the desired solution. The set of parameters to be estimated are

$$\{\theta\} = \{E^{\text{gen}}_{\text{bHad}}, E^{\text{gen}}_{\text{bLep}}, E^{\text{gen}}_{\text{LJ1}}, E^{\text{gen}}_{\text{LJ2}}, E^{\text{gen}}_{\text{bH1}}, E^{\text{gen}}_{\text{bH2}}, E^{\text{gen}}_{l}, E^{\text{gen},x}_{\nu}, E^{\text{gen},y}_{\nu}, E^{\text{gen},z}_{\nu}\} \tag{4.6}$$

these are the generator level energies of the quarks, of the lepton and all the momentum components of the generator level neutrino. Only the energies of the particles are considered, and not the other Lorentz components, except for the neutrino, due to computational limitations. These could be added but it seems sufficient, for the reconstruction efficiency, to just consider the energy.

Let us consider the measurable data

$$\{\mathcal{Y}\} = \{\{X^{\text{meas}}_{\text{J}_n}\}, X^{\text{meas}}_{l}, E^{\text{meas}}_{\nu,x}, E^{\text{meas}}_{\nu,y}\} \tag{4.7}$$

composed of the 4-momentum of the detected jets (the number of jets varying in each event), of the lepton, as well as the missing transverse momentum components, x and y.

For the jets, there can be ambiguity regarding their connection with generator level partons. The following criteria will be valid hereafter: it is considered that a single generator parton can only give rise to one jet and that one jet can only come from a single parton. Partons are considered to be the generator quarks, associated with the LO naive picture of the process. This means that only events with at least six jets are able to make correspondences with the six generator quarks that might have originated them. Valid events obey these conditions and also include one, and only one, lepton. The case for the neutrino and lepton is simple. In the current topology it is expected only one of each. They will be directly associated with the missing momentum and the detected lepton, respectively.

In a valid event, M permutations of six jets are created to associate with the six generator quarks. In order to verify which permutation of jets better associates with the generator level counterparts we can also use the MLE. To do so, M solutions from the likelihood function are computed, one for each permutation. In each permutation a specific order is considered, which associates the detected jets, in that set, to the generator objects, in a unique way. The definition is as follows: for a particular permutation k, the *permutation* data considered for the likelihood and its respective ordering, is given by

$$\{y\}_k = \{E^{\text{meas}}_{\text{bHad}}, E^{\text{meas}}_{\text{bLep}}, E^{\text{meas}}_{\text{LJ1}}, E^{\text{meas}}_{\text{LJ2}}, E^{\text{meas}}_{\text{bH1}}, E^{\text{meas}}_{\text{bH2}}, E^{\text{meas}}_{l}, E^{\text{meas},x}_{\nu}, E^{\text{meas},y}_{\nu}\} \tag{4.8}$$

the measurable data is permuted and the previous set is filled for the M possibilities.

Assuming the likelihood is well defined and a solution is retrieved, the following scale factor can be defined

$$\xi_i = \sqrt{\frac{(E^{\text{gen}}_i)^2 - m_i^2}{(E^{\text{meas}}_i)^2 - m_i^2}} \tag{4.9}$$

where i indexes the gen quark, and corresponding detected jet (of the solution permutation), or the singular lepton. In turn, this will set the remaining components of the gen objects

$$\vec{p}^{\,\text{gen}}_i = \xi_i \vec{p}^{\,\text{meas}}_i \tag{4.10}$$

Comparing $\{\theta\}$ (4.6) and $\{y\}_k$ (4.8), there is a variable that is not coincident between the sets, namely the z momentum component of the neutrino. This component is set from the following kinematic constrain

$$m_W^2 = (\vec{p}_\nu + \vec{p}_l)^2 \tag{4.11}$$

which forces the invariant mass of the lepton+neutrino system to be equal to their W progenitor. The cases where there are two solutions will be discussed below. When there is none, the longitudinal component will be set to 0 GeV.

To construct the likelihood, Transfer Functions (TFs) are needed. These carry the information about smearing and deviation of all detectable objects. The detected missing transverse momenta and lepton are very simply related to their generator counterpart. Unfortunately, NLO effects and lost jets create mismatching cases for the quarks. These affect the stochastic behavior of the quarks' TFs, leading to difficulties in retrieving the generator quark information.

Mismatching effects happen since, in order for these TFs to be computed, one has to develop an algorithm that reconstructs an event with the corresponding *true* (known *ab initio*) generator information. This is called a truth-matching reconstruction and is responsible for relating both levels (generator and particle). This is developed and explained in full in chapter 5.

Even though one has the information of both levels, multiple jets may have the same parton progenitor, due to NLO effects, or some might get lost, due to detector's blind spots. Even though these effects can be studied and reduced, 100% matching efficiency is impossible to achieve, thus, the TFs will not be fully accurate.

The Transfer Functions of the ATLAS detector, their development and study is described in full in Chapter 5. For now, let us assume that they exist and are given by

$$\begin{aligned} p_i(E_i^{\text{meas}}|E_i^{\text{gen}}) &\equiv W_i^{\text{jet}}(E_i^{\text{meas}}|E_i^{\text{gen}}) \\ p_l(E_l^{\text{meas}}|E_l^{\text{gen}}) &\equiv W_l(E_l^{\text{meas}}|E_l^{\text{gen}}) \\ p_{\text{miss}}(E_{\text{miss,j}}^{\text{meas}}|E_{\nu,j}^{\text{gen}}) &\equiv W_{\text{miss}}(E_{\text{miss,j}}^{\text{meas}}|E_{\nu,j}^{\text{gen}}) \end{aligned} \tag{4.12}$$

where i is the gen object and corresponding paired detected jet (of the kth permutation) index. The index j corresponds to either component of transverse momentum. The last two TF's correspond to the lepton and neutrino, respectively.

For quarks these transfer functions need not be all different. E.g., the TF for the hadronic and leptonic b quarks might be the same (and will be). If there are at least two similar TFs, then the likelihood loses sensitivity to the permutation of jets in those positions.

To solve this, one patches up the likelihood with Breit-Wigner distributions

$$B(m|m_0,\Gamma) = \frac{b}{(m^2 - m_0^2)^2 + m_0^2\Gamma^2} \tag{4.13}$$

where m, m_0 are the measuread invariant and pole mass of a certain system, respectively. The decay width for that particular resonance is given by Γ.

These functions will incorporate the decayed W boson, t quarks and the Higgs information into the likelihood, making it fully sensitive to the permutation considered. Moreover, it will help in situations where the *true* jet(s) is(are) lost or not present, as it will not allow large invariant mass deviations.

When there are two neutrino solutions, the corresponding Breit-Wigner for the leptonic top will decide which one is most probable and that is the solution considered.

The likelihood function then reads

$$
\begin{aligned}
p(y|\theta) \equiv L(y|\theta) = {} & B(m_{(\text{bHad,LJ1,LJ2})}|m_{\text{top}}, \Gamma_{\text{top}}) \cdot B(m_{(\text{LJ1,LJ2})}|m_W, \Gamma_W) \\
& \times B(m_{(\text{bLep},l,\nu)}|m_{\text{top}}, \Gamma_{\text{top}}) \cdot B(m_{(l,\nu)}|m_W, \Gamma_W) \\
& \times B(m_{(\text{bH1,bH2})}|m_H, \Gamma_H) \\
& \times \prod_{i=1}^{6} W_i^{\text{jet}}(E_i^{\text{meas}}|E_i^{\text{gen}}) \cdot W_l(E_l^{\text{meas}}|E_l^{\text{gen}}) \\
& \times W_{\text{miss}}(E_{\text{miss,x}}^{\text{meas}}|E_{\nu,x}^{\text{gen}}) \cdot W_{\text{miss}}(E_{\text{miss,y}}^{\text{meas}}|E_{\nu,y}^{\text{gen}})
\end{aligned}
\tag{4.14}
$$

where $m_{(q_1,q_2,\ldots)}$ is the mass of the reconstructed system composed of the $X_{q_1} + X_{q_2} + \ldots$ objects.

Everything is in place to estimate the generated particle four-momenta, for any given event. Since the Breit-Wigners have just one maximum and the Transfer Functions will be shown to have just one as well, there can only be one global maximum for the likelihood function too. Therefore, there is only one possible solution, given by the estimators (4.5). Moreover, these estimators are proven to be consistent, a general property of the MLE.

The most probable generator values of energy at the absolute maximum of the likelihood, for the permutation chosen as the correct solution, conditioned to the measured data, are analogous to the global maximum of the *posterior* probability (4.4) in Bayes' analysis. The generator values considered in this analysis are taken as *true* values.

Chapter 5

Event Selection and Reconstruction

This chapter will describe in detail the event selection process, as well as the reconstruction methods.

The reconstruction of an event means inferring the four-momentum of a particle, at *parton*[1] level, from the available information after simulation where experimental effects, like acceptance and E/p resolutions are taken into account.

A method was developed to perform event reconstructed based on the available simulated information. This method involves the following steps:

- Pre-selection.
- Truth Match Reconstruction.
- Non-Truth Match Reconstruction.

The Pre-selection is done to retain events with the right generator topology.

In order to create a reconstruction method without truth match based on the Maximum Likelihood Estimate (MLE), the energy/momentum response information of the detected particles and of the missing transverse energy is necessary and is given by the transfer functions (TFs). Leptons response behavior is directly obtained from the ATLAS card.

On the other hand, the interaction of the quarks' shower and hadronization products with the detector is not trivial. Quarks generate several neutral and charged particles, the latter generates tracks in the detector and are handled individually. These charged and neutral particles will be bundled together into jets, through a jet clustering algorithm. This algorithm is independent of the detector's resolution effects. In turn, it is not possible to obtain the quarks' TFs directly from the collision generation information. Moreover, there is lack of information on the response of the missing transverse energy. This motivates the creation of a truth match (TM) analysis.

The TM analysis relates the hard-scattering- (parton) with `Delphes` jets and leptons of an event. As the collision simulator generates *next-to-leading-order* (NLO) processes, non-trivial phenomena is present in the events[2]. Also, the `Delphes` simulation incorporates the ATLAS blind spots, meaning that some objects might not be present in the `Delphes` sample. To study the events, reduce undesired phenomena and best correlate the information to create accurate TFs of the quarks and MET is within the TM analysis domain.

With the TFs set, the non-truth match reconstruction method can be implemented. This will enable the analysis of information that can be detected in an actual experiment and, as such, the last step for finding sensitive variables to the CP properties of the Higgs boson.

---

[1] Parton information refers to the hard-scattering part of a collision process at the LHC and its first subsequent decay products, before any showering/hadronization occurs.

[2] Gluon emission at the parton level.

5.1 Pre-selection

A pre-selection is necessary for the TM analysis. Only events with twelve partons at generator level are selected, these being two *top* quarks, four *bottom* quarks, two light quarks, two W gauge bosons, one charged lepton and one neutrino.

Additionally, events are required to have jets and leptons reconstructed after `Delphes` simulation. Some of the generated and simulated events will not pass this specific criteria.

5.2 Event Selection

Following the pre-selection, additional criteria is applied to the events to increase the signal to noise ratio. This selection can be applied to different parts of the reconstruction process (truth or non-truth match) and will have an impact on the percentage of events that are retained, analyzed, as well as on *purity*[3] of the sample.

Leptons (electrons and muons) and jets (including jets from the hadronization of b-quarks), are selected if they fall within specific acceptance regions of pseudo-rapidity and transverse momentum, given in Table 5.1. Events which do not pass any of these criteria are rejected.

Object	$\lvert\eta\rvert <$	$Pt >$ (GeV)
Leptons	2.5	20
b-tag Jets	2.5	20
non b-tag Jets	4.5	20

TABLE 5.1: Acceptance region of pseudo-rapidity and transverse momenta of the detectable particles at ATLAS. The b-tag Jets efficiency formula is only valid for $\lvert\eta\rvert < 2.5$.

Applying acceptance cuts[4] before kinematic reconstruction may impact on the overall performance of the algorithm (purity and efficiency) by removing objects which would match better the parton level objects, and would be the most probable choice of the reconstruction algorithm. A lower purity is then expected following this procedure. Applying cuts after, will make the best assignment out of all objects but a fraction of these events will not survive the cuts. As the reconstruction process always returns a solution, it is expected fewer events in the solution sample, comparing with the previous way.

Figure 5.1 shows the multiplicities of jets and leptons (electrons and muons), before any cuts are applied for a $t\bar{t}H$ signal sample after `Delphes` simulation.

The event selection for the truth match analysis revolves around defining the best transfer functions. That is attainable when the considered solution objects are the ones that best match with the parton level quarks and leptons. Furthermore, it is necessary to know if these TFs applied to the non-truth match reconstruction are able to maximize the reconstruction efficiency. To this end, one applies cuts before and after truth-match reconstruction, ending up with two different samples. Testing how much the TFs differ from one another will lead to knowledge on the impact of cuts.

Event selection a non-truth match level is always done before the non-truth match reconstruction procedure. This is to mimic a true detector's response. Different topologies will be selected at a time to study the reconstruction efficiency individually. As expected, different topologies have different efficiencies.

---

[3] Purity is defined as how close the solution sample (obtained from the `Delphes` sample) it to the true generator level information.

[4] The term *cut* refers to filtering particles in a event by retaining only the ones that are within their acceptance region.

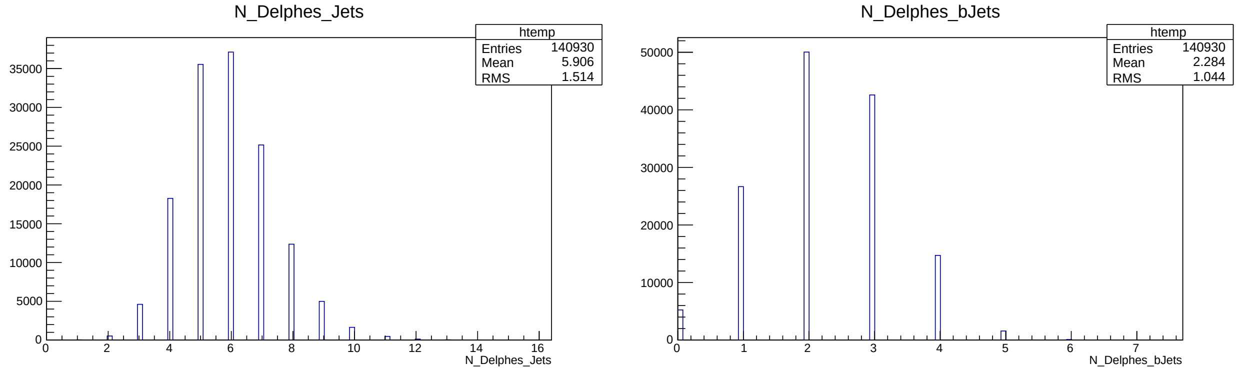

(A) Total number of Jets

(B) Number of *b-tagged* Jets

FIGURE 5.1: Distribution of the number of jets and b-jets of a `Delphes` sample, before any cuts.

5.3 Reconstruction with Truth Match

The aim of the truth match reconstruction is to define the transfer functions. Thus only $t\bar{t}H$ signal events are reconstructed with truth match.

The reconstruction with truth match was build using `MadAnalysis5` [29]. There are several ways to implement reconstruction methods with truth match, each with its *pros* and *cons*. Nevertheless, all of them are focused on relating the detectable `Delphes` objects of an event with the hard-scattering partons at generator level. This section will explain the method chosen and corresponding results and efficiencies.

Let us start by displaying some example algorithms:

- Finding the combination of partons and `Delphes` objects (jets and leptons) that minimizes the modulus of the difference of four-momentum[5] between them

  $$P_{ij}^2 = (P^{\mu}_{i,\text{gen}} - P^{\mu}_{j,\text{delphes}})(P^{\nu}_{i,\text{gen}} - P^{\nu}_{j,\text{delphes}}) \tag{5.1}$$

  where i and j are the objects' indexes.

- The combination of objects that minimizes ΔR instead, given by

  $$\Delta R_{ij} = \sqrt{(\eta_i^{\text{gen}} - \eta_j^{\text{delphes}})^2 + (\phi_i^{\text{gen}} - \phi_j^{\text{delphes}})^2} \tag{5.2}$$

  with η and ϕ being the pseudo-rapidity and azimuthal angle of the respective `Delphes` objects.

The $\mathbf{\Delta R}$ method was the one used in this study. It is faster then the method of *momenta* in terms of computational speed since it deals with less variables. In terms of efficiency it is less powerful than the former as several objects might have the same direction. Nevertheless, it is adequate for additional imposed criteria, as will be seen.

The *sum* algorithm was developed to incorporate the one-to-one correspondence criteria for jets[6]. The algorithm permutes the set of jets, generating all possible pairs between partons and jets. Then for each permutation ξ the sum of ΔR is computed

$$\Delta R^{\xi}_{\text{total}} = \sum_i \Delta R^{\xi}_i \equiv f(\xi) \tag{5.3}$$

---

[5] On a perfect detector and with a fixed LO process $P_{ij}^2 = 0$.

[6] A jet can only be associated with one parton and vice-versa.

where i is the pair index in permutation ξ. The solution is the permutation $\xi^\star$ which has the minimum value in $\{\Delta R_{\text{total}}\}$,

$$\xi^\star = f^{-1}(\min(\{\Delta R_{\text{total}}\})) \tag{5.4}$$

Only events with one `Delphes` charged lepton are selected. This lepton is always considered the solution.

The set of `Delphes` objects that form a solution are called matched. A matched particle is considered valid if

$$\Delta R_{ij} \leq 0.4 \tag{5.5}$$

There will be seven matched objects in a solution. One matched lepton that is identified with the generator charged lepton and six matched jets that are identified with the six final state partons. The jets taken as solution will inherit the following nomenclature:

- **Matched light-quark** - for either jet that is associated with one of the generator light quarks.
- **Matched Higgs b-quark** - for either jet that is associated with one of the generator b-quarks from the Higgs decay.
- **Matched leptonic b-quark** - for the jet that is associated with the generator b-quark from the same top quark of the leptonically decaying W boson.
- **Matched hadronic b-quark** - for the jet that is associated with the generator b-quark from the same top quark of the hadronically decaying W boson.

To complement the algorithm, the jets b-tag information and the *isolation* of the solutions is evaluated. A reconstructed object is *isolated* if no other jet is within its corresponding parton's matching cone[7].

Let us verify the b-tagging distribution of the solutions. There is a small percentage of cases were a reconstructed light-quark is b-tagged. This happens 0.4% of the times and it is relatively constant through the values of transverse momentum. This ratio is higher than expected from the misidentification rate formula (3.4). On the other hand, Figure 5.2 shows that isolated matched solutions have a b-tag distribution slightly lower to the `Delphes` identification rate. This is due to mismatching since it is expected partons of the light kind to be taken as of the *bottom* kind and vice-versa. In turn, the matched identification rates are altered by a small fraction from their `Delphes` values.

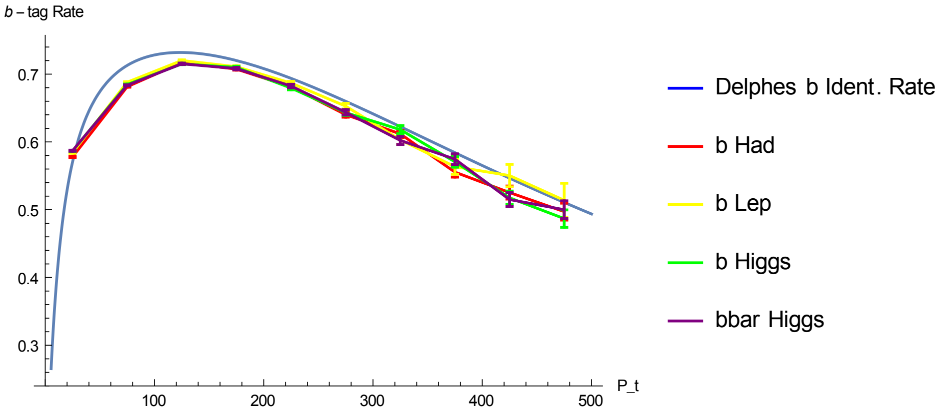

FIGURE 5.2: b jet identification rate and ratio of b-tag for reconstructed b-jets imposing the solution to be unique for comparison.

---

[7] The solid angle around a generator particle that defines the matched region for `Delphes` objects.

Figure 5.3 shows the matched objects' ΔR distributions for isolated and correct b-tag assignment events, without any cuts applied (in p_T or η).

The matched b-quarks follow a similar distribution between themselves. The jets associated to the light quarks do too.

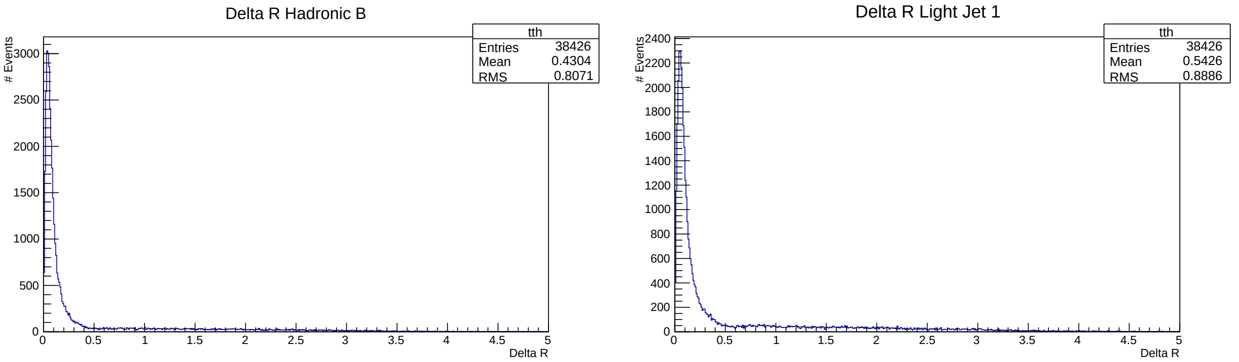

(A) Hadronic B (B) Light Jet 1

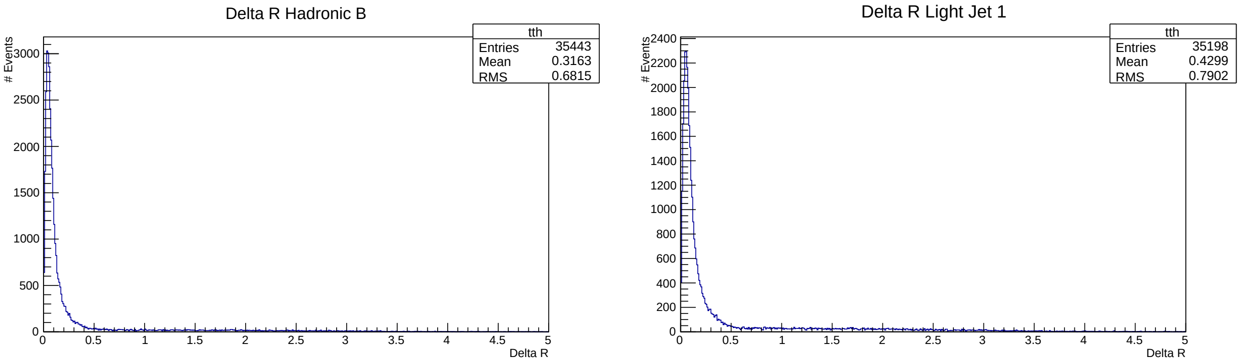

(C) Hadronic B (unique) (D) Light Jet 1 (unique)

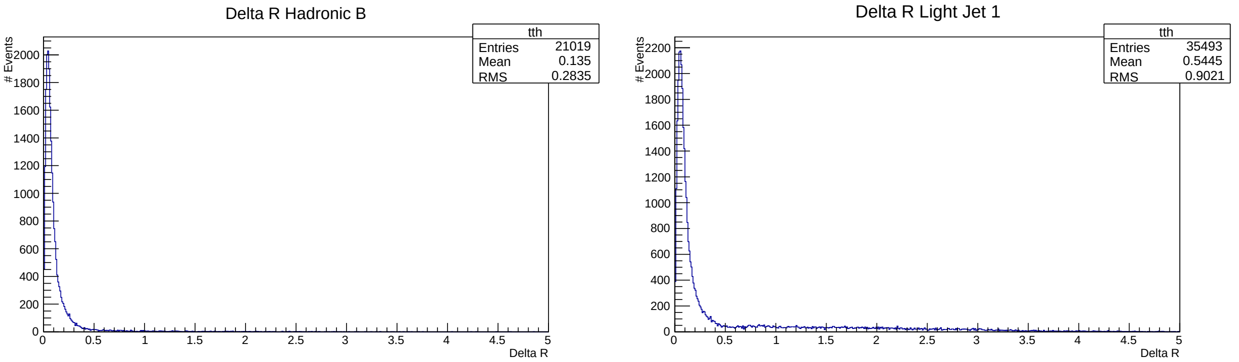

(E) Hadronic B (b-tag) (F) Light Jet 1 (non b-tag)

FIGURE 5.3: ΔR distributions of the matched hadronic b-quark (left) and of a matched light-quark (right) under different filtering. The first row is the complete set of solutions, on the second it is filtered to just consider isolated solutions and the third with the correct b-tag.

Table 5.2 lists the mean values of the ΔR distributions. All the distributions are similar to an exponential decay, the values hint on how much the tails extend.

Filtering matched object by correctly assigned b-tag does not reduce the mean ΔR values for matched light-quarks, they reduce only with isolated solutions. On the other hand, even though isolated solutions reduce the ΔR mean values for matched b-quarks, the matching efficiency is best when selecting events with right b-tag.

Objects	*Sum* method	*Sum* method (isolated)	*Sum* method (b-tag)
Hadronic b	0.4510	0.3378	0.1581
Leptonic b	0.4324	0.3348	0.1480
Light jet	0.5444	0.4476	0.5438
Light anti-jet	0.5430	0.4395	0.5425
Higgs b	0.4893	0.3921	0.1572
Higgs $\bar{b}$	0.4868	0.3916	0.1604

TABLE 5.2: Mean values of the ΔR distributions when filtering the solutions with different criteria. The first column on the left has no filtering, the middle refers to isolated solutions, on the right one the matched jets have the right b-tag.

In order to evaluate the truth-match reconstruction procedure, one can cross check with other tests. Let us verify the differences in the momentum components between partons and matched objects. To quantify these differences a reduced Pearson's χ^2 test is used with 1000 random events for all possible *scenarios*, i.e. in events with the right b-tag, with isolated solutions, etc. Table 5.3 gives the test values for the matched leptonic b-quark and light-quark .

Figure 5.4, 5.5 and 5.6, 5.7 shows the comparison of the different scenarios for the matched b-quarks and light-quarks, respectively. Analogously, the previous scenarios eliminate events far away from the linear regression line. On the other hand, it is not verifiable that solutions with the right b-tag are the best ones.

Leptonic b-quark	χ^2	χ^2_B	χ^2_M	χ^2_{MB}	χ^2_{iM}	χ^2_{iMB}
P_x	1.32	5.18	0.82	5.18	1.53	2.02
P_y	7.94	1.25	1.42	0.91	1.41	2.86
P_z	1.17	1.79	1.74	1.67	1.18	1.23
E	2.67	1.69	3.08	0.77	0.81	2.01
Light quark	χ^2	χ^2_B	χ^2_M	χ^2_{MB}	χ^2_{iM}	χ^2_{iMB}
P_x	1.23	1.26	0.49	0.49	0.69	0.70
P_y	0.98	0.96	0.71	0.69	0.41	0.42
P_z	3.01	3.21	4.11	4.26	4.02	4.10
E	0.55	0.53	0.42	0.43	0.66	1.06

TABLE 5.3: Person's reduced χ^2 test values of the closeness of fit of the momentum components of the leptonic b quark and light quark results to the ($m = 1$) linear regression line. The test is done with 1000 random events for each criteria. The subscript indicates the criteria selected: *B* for b-tagged, non-b tagged for the light jet, *M* for matched, *iM* for isolated and matched.

For the case of matched leptonic b-quark and light-quarks the b-tag information does not always improve the χ^2 results. The best set of values are given when choosing the isolated matched case. This tells that criteria for the events used to construct the TFs should be the isolated matched case. This is convenient since it enables the TFs of b-quarks to cover a larger region of pseudo-rapidity. TFs for b-quarks can now be defined up to $|\eta| \leq 4.5$, this enables non-truth match reconstruction of jets coming from b-quarks that are not b-tagged due to being outside the $\eta \leq 2.5$ window.

It should be stressed that for the non-truth match reconstruction the b-tag information will be crucial to remove combinatorial background.

Let us evaluate the survival rates and the effects of cuts on the solutions. Table 5.4 and Table 5.5 display, in terms of ratios, the event survival rate at each step and with different criteria. Both tables use the following definitions:

Level	Fraction	Value
(a) Total *Delphes* Sample	a/a	1
(b) MC Event Selection	b/a	~0.70
(c) Solutions No Cuts	c/a	~0.19
(d) Solutions With Cuts	d/a	~0.17

TABLE 5.4: Truth Match Reconstruction event survival rates.

No Cuts Events			With Cuts Events		
	Fraction	Value		Fraction	Value
(c) Events	c/a	~0.19	**(d)** Events	d/a	~0.17
(e) Cuts After Rec.	e/a	~0.16	**(h)** Same Sol. No Cuts	h/d	~0.99
(f) W/ criteria (no btag)	f/e	~0.18	**(i)** W/ crit. (no btag)	i/d	~0.17
(g) W/ criteria (w/ btag)	f/e	~0.03	**(j)** W/ crit. (w/ btag)	j/d	~0.05

TABLE 5.5: Differences in survival rates between applying cuts before or after the reconstruction process.

- **(a)** - Percentage of events in a generic *Delphes* sample, represents the total number of events considered.
- **(b)** - Percentage of events that passed the MC Event Selection. Only `Delphes` events with 12 generetor level particles of the required type are accepted.
- **(c)** - Percentage of truth-match solutions without cuts. Referred to as No Cuts.
- **(d)** - Percentage of truth-match solutions after applying cuts. Referred to as With Cuts.
- **(e)** - Percentage of No Cut events (c) that passes cuts after truth match reconstruction is done.
- **(f)** - Percentage of No Cut events (c) that passes cuts after truth match reconstruction and are isolated matched.
- **(g)** - Percentage of No Cut events (c) that passes cuts after truth match reconstruction, are uniquely matched and b-tag is correctly assigned.
- **(h)** - Percentage of With Cut Events (d) that have the same solution as the No Cut events (c) counterpart.
- **(i)** - Percentage of With Cut Events (d) that are isolated matched.
- **(j)** - Percentage of With Cut Events (d) that are isolated matched and the b-tag is correctly assigned.

One can draw the final conclusions considering this method and having in mind the non-truth match analysis ahead. First of all, let us go through the effects of applying cuts: 99% of *With Cuts* events (d) are the same as *No Cuts* events (c). This means that the TFs constructed with *No Cuts* events (c) will be applicable to jets, which pass the cuts, 99% of the times.

Finally, one can predict the maximum efficiency of the non-truth match reconstruction. As the isolated matched *With Cuts* events (i) account for 17% of events that pass cuts (d), one can only expect to get a maximum of 3% of efficiency, with respect to the total number of events. If it is also used b-tag information the maximum possible number of well reconstructed events drops to slightly below of 1% of the total number of events.

5.3.1 Transfer Functions

Let us start with leptons, their TFs are defined in the ATLAS cards of the `Delphes` fast simulator. The information about leptons reconstruction is embedded in their energy parametrization (transverse momentum for muon's case) which is usually taken from real data. The case for jets is more complex since not only the individual particles of a jet are parametrized but they are bundled together with a jet clustering algorithm. The jets' TFs can be obtained using the previous truth matching procedure.

Electrons

The parametrization of energy, for electron, and transverse momentum, for muons, can be attained directly from the ATLAS card in `Delphes` (Appendix **??**). These can be directly translated into TFs. The transfer functions for electrons are gaussian ones

$$G(E^{\text{meas}}, E^{\text{true}}) = \frac{1}{\sqrt{2\pi\sigma^2(E^{\text{true}})}} \exp\left[\frac{(E^{\text{meas}} - E^{\text{true}})^2}{2\sigma^2(E^{\text{true}})}\right] \tag{5.6}$$

where E^{meas} and E^{true} are the measured energy and true energy respectively. Due to the TFs form, the variance for electrons must have units of energy $[E]$.

There are four regimes, given in Table 5.6. The variance in each regime, i.e. as function of E and η, is given by

$$\sigma^i(x) = (C_1^i x)^2 + C_2^{i2} x + C_3^{i2} \tag{5.7}$$

with i the regime index and C_1^i, C_2^i and C_3^i being parameters which differ for each regime. The parameters are displayed in Table 5.6.

	$0.1 \leq E < 25$ GeV	$E \geq 25$ GeV
$0 \leq \eta < 2.5$	1	2
	$0 \leq E < \infty$ GeV	
$2.5 \leq \eta < 3$	3	
$\eta \geq 3$	4	

Regime	C_1	C_2	C_3
1	0	0.015	0
2	0.005	0.05	0.25
3	0.005	0.05	0.25
4	0.107	2.08	0

TABLE 5.6: (Left) Indexing of the electron regimes. Each one of the regimes has a different transfer function. (Right) Electron's TF parameters for each regime.

Muons

The muons' case is similar to the electrons' one. The TFs for muons are also gaussian functions but depend on the transverse momentum,

$$G(P_t^{\text{meas}}, P_t^{\text{true}}) = \frac{1}{\sqrt{2\pi\sigma^2(P_t^{\text{true}})}} \exp\left[\frac{(P_t^{\text{meas}} - P_t^{\text{true}})^2}{2\sigma^2(P_t^{\text{true}})}\right] \tag{5.8}$$

The variance is also dependent on the regime of transverse momentum, and must have units of momentum $[P_t]$.

The variance is constant per regime of momentum considered. Table 5.7 displays the values.

Transverse Momentum	$1-50$ GeV	$50-100$ GeV	≥ 100 GeV
$0 \leq \eta < 1.5$	0.03	0.04	0.07
$1.5 \leq \eta < 2.5$	0.04	0.05	0.1

TABLE 5.7: Muon's variance per regime considered. The variance is now constant and independent of the lepton's true energy.

5.3.2 Jets

The TM analysis showed that applying cuts before or after the reconstruction has a minimal impact on which `Delphes` objects are taken as solution. Hence, TFs will be based on solutions which are isolated matched and with cuts applied after the truth match reconstruction process. This makes sure that the solutions retained are the correct ones, as often as possible. Also, since cuts will be applied individually to each jet and not to the whole set of solutions this will have a higher number of retained events than considering solutions where cuts are applied before truth match reconstruction.

As was described in Chapter 4, the likelihood function depends only on the energy transfer functions of the reconstructed objects and on Breit-Wigners.

It was verified that TFs at the DØ experiment follow double gaussian distributions [34]. The same was verified at the `Delphes` simulation of ATLAS. These TFs are double gaussians

$$D(R) = \frac{1}{\sqrt{2\pi}} \left\{ \frac{C_1}{\sigma_1} e^{-\frac{(R-\mu_1)^2}{2\sigma_1^2}} + \frac{C_2}{\sigma_2} e^{-\frac{(R-\mu_2)^2}{2\sigma_2^2}} \right\} \tag{5.9}$$

where C_1, C_2, μ_1, μ_2, σ_1, σ_2 are the integrals, mean values and standard deviations of the individual gaussians, respectively. They constitute the fitting parameters to be evaluated. The dependency is on the energy of the matched and generator objects, given by R. In order to obtain the most accurate double gaussian fit, several energy dependences were tested, the following proved to be the best found

$$R(E^{\text{true}}_{\text{jet},i}, E^{\text{meas}}_{\text{jet},i}) = \frac{E^{\text{meas}}_{\text{jet},i} - E^{\text{true}}_{\text{jet},i}}{\sqrt{E^{\text{true}}_{\text{jet},i}}} \tag{5.10}$$

which sets the mean values μ_1, μ_2 and the standard deviations σ_1, σ_2 to have units of $[\sqrt{E}]$.

The TFs will have to be normalized and so C_1 and C_2 will be transformed in such a way that the ratio between them remains invariant and

$$C_1 + C_2 = 1 \tag{5.11}$$

A priori, these TFs may depend on which jet is being evaluated and also on which window of pseudo-rapidity and transverse momentum is considered. For that end, subsets of solution events in blocks of 100 GeV of reconstructed energy, starting at 20 GeV, and of 0.5 of absolute value of reconstructed pseudo-rapidity, starting at 0, were created. Consequently, the corresponding TFs were computed for each of the six reconstructed jets for each regime block.

Two distinctive patterns emerged, one for the b-quarks and another for the light-quarks. The histogram differences were checked, in each window, for all the possible pairs and computed the maximum relative difference in each bin. There were considerable discrepancies between b-quarks and light-quarks. But within each of these groups the maximum relative difference in each bin did not go beyond 2%. This seems an indicator that there are two effective transfer functions per object kind, one for the light-quarks and another for the b-quarks. Therefore, only two transfer functions for each energy and pseudo-rapidity window were created.

The full distribution of Transfer Functions and their corresponding best double Gaussian' fitting parameters and χ^2 values are available in Appendix A.

5.3.3 Missing Transverse Momentum

In the expected final state topology, the missing transverse energy (MET) will have a direct relationship with the missing neutrino since it should be the only undetectable particle. Nevertheless, contributions to the MET are also expected from particles that fall outside the detector acceptance.

One expects that the TF for the MET gives the information regarding how much the MET differs itself from the transverse energy of the generator neutrino.

Since it is impossible to have access to the longitudinal momentum component of the missing momentum, the transfer function will only be able to relate the transverse components. With all the other particles, the MET should sum to zero.

The MET follows an analogous distribution with that of jets, given in equation (5.9) but with a different dependency

$$R(P_i^{\nu_{\text{gen}}}, P_i^{\text{miss}}, \psi \equiv \sum_{\text{rec}} P_t) = \frac{P_i^{\text{miss}} - P_i^{\nu_{\text{gen}}}}{\psi^{1/2}} \tag{5.12}$$

where ψ is the sum of the modulus of the transverse momentum component of all the detected particles. The argument for choosing this particular dependency was to best fit the MET TF to a double gaussian.

The data was partitioned into regions of sum of reconstructed transverse momenta. The parameters of the fit remained constant for each regime. This means that the numerator and denominator of (5.12) scale by the same factor. This, as well as the fact that there were no significant differences between the two components makes it possible to have a singular transfer function to describe the missing transverse momentum behavior.

Shown in Figure 5.9 is the fitting of the TF for the MET with $\chi^2 = 7790.55$, showing that the fit is very good, considering the number of events. The fitting values of the two gaussians are: $\mu_1 = -0.0007$, $\mu_2 = 0.0054$, $\sigma_1 = 1.164$, $\sigma_2 = 2.720$, and the ratio $\frac{C_1}{C_2} = \zeta = 0.212$.

5.4 Non-Truth Match Reconstruction

A non-truth match reconstruction method addresses a detected event sample by reconstructing it purely based on the transfer functions (TFs). This enables reconstruction of events from data collected by a real experiment at the LHC.

The TFs were created upon the one-to-one correspondence criteria[8]. Thus, this criteria is also valid in this reconstruction level as well. This makes this non-truth match analysis a LO type reconstruction.

This reconstruction level is based on the Maximum Likelihood Estimate (MLE), the likelihood function considered is given in (4.14). Not only should the reconstruction be able to find the best match between detected jets and partons of the hard scattering process of the topology in study, it should also be able to estimate the partons' true four-momentum (4.6).

The solution particles are: the leptonic and hadronic b-quark, the light quarks from the W boson decay, the b-quarks from the Higgs' decay, the charged lepton and the neutrino. These correspond to the most probable `Delphes` objects of being associated to their parton' counterparts. The solution also includes momentum changes from the TFs to rollback smearing effects. The rest of the initial parton state is retrieved from these.

The algorithm works as follows:

- Only events that pass selections are accepted for non-truth match reconstruction.

---

[8] A jet can only be associated with one parton and vice-versa.

- A full set of permutations is considered of the selected jets. In each permutation a detected jet occupies a specific position in the ordered list of generator partons. Permutations are performed according to b-tag and redundancy. One may opt to just have b-tagged jets occupying b-quark positions, vetoing the other possibilities. Or having b-tagged jets occupy all positions but not non-b jets ones, etc. Redundancy has to do with the swap of particles between positions that do not generate a different solution[9].
- For each permutation, a likelihood function is computed to estimate the best set of parameters. For each permutation a set of solution particles is created, which correspond to the permutation selected but with the correction of the considered parameters.
- For each permutation the likelihood value is evaluated and the solution chosen is the one associated with the permutation with highest value of the likelihood.

Due to the small Higgs decay width, the Higgs mass is fixed to the pole. The top quark mass is also assumed at its pole which generates better results in terms of reconstruction efficiency.

The developed method was based on the `KLFitter` package [34]. The `KLFitter` is in turn set upon the `BAT`, *Bayesian Analysis Toolkit* [22], which is a C++ library for parameter estimation, Bayesian inference and other statistical methods.

For the reconstruction of $t\bar{t}H$ semileptonic final states, algorithmic modules were created/altered to incorporate the specific decay process under study,to describe the TFs for the ATLAS experiment, to handle data interfaces, etc.

---

[9] For instance, exchanging two detected jets between the light jets slots will not alter the outcome since the corresponding Breit-Wigner of the hadronic W boson will be the same.

This was assembled as shown in Figure 5.10, where the key modules and how are described as follows

Fitter (1) The Fitter has to keep track of the modules memory address, check for status report of them. It also handles the permutation table for the Selected Particles (c) and calls on the Bayesian modules to perform the parameter estimation for each permutation.

Input Int. (2) Manages the reading procedure of the `MadAnalysis5` data, i.e. the simulated truth and detected information.

Sel. Tool (3) Module responsible for selecting events based on transverse momentum and pseudo-rapidity cuts. Also filters events selection the final topology (b). It returns a set of selected objects that fulfil the requirements.

Match. Tool (4) This module evaluates the selected particles (c) based on the *truth* information (a). It is responsible for evaluating the efficiency of the method by checking if a set of selected particles is uniquely truth matched and if the fitter gave the correct permutation as solution in that case.

Detector (5) Here the transfer functions information can be found. It works in parallel with the Likelihood (6) module. Each permutation will call on different transfer functions for each selected particle that is being evaluated at a model position.

Likelihood (6) It incorporates the Likelihood function, calls on the Detector's Interface (5) to fetch the corresponding transfer functions, sets the parameters to be estimated, sets the rules to modify the permutation table and generates the model particles for each permutation.

Out. Inter. (7) The final module collects the whole set of data (a), (b) and (c) and stores in a root format file. It also computes the efficiency obtained with the information used for the TFs and the topology selected.

5.4.1 Performance Studies

Let us evaluate the results from the kinematic fit. As was pointed out, this will be subdivided into different final state topologies. As a rule, the b-tag information will be used to veto cases where b-tagged jets are on light-quark positions. It was then selected cases with $n \geq 6$ jets, from which $0 \leq n_b \leq 4$ are b-tagged.

The following table will present the results obtained. The *reconstructed efficiency* is defined as the fraction of matched events for which the chosen permutation is the correct one.

	Reconstruction Efficiency [%]				
Topology	Overall	b_{had}	b_{lep}	W_{had}	Higgs
6 Jets (4-btagged)	54.4	84.8	54.4	100	63.0
7 Jets (4-btagged)	26.2	60.6	55.7	79.5	44.3
6 Jets (3-btagged)	41.4	59.4	62.7	73.3	52.0
6 to 8 Jets (3 to 4 btagged)	30.1	51.2	57.1	68.0	43.1

TABLE 5.8: Reconstructed efficiencies of the Maximum Likelihood Method on a KLFitter implementation. The values represent the *reconstructed efficiency* which is defined as the fraction of matched events for which the chosen permutation is the correct one.

A solution is always found when an event survives the several cuts. Table 6.4 and 6.5 display the full cut flow for the non-truth match reconstruction.

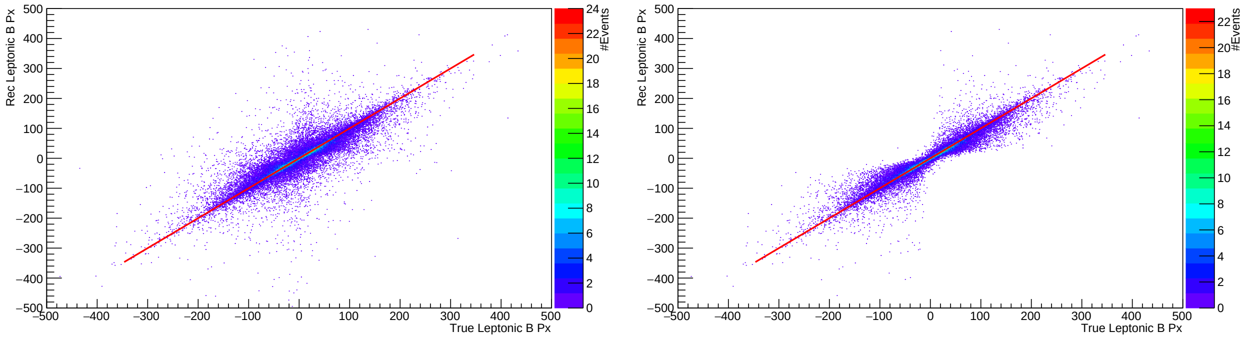

(A) P_x component (B) P_x comp. ($\Delta R < 0.4$)

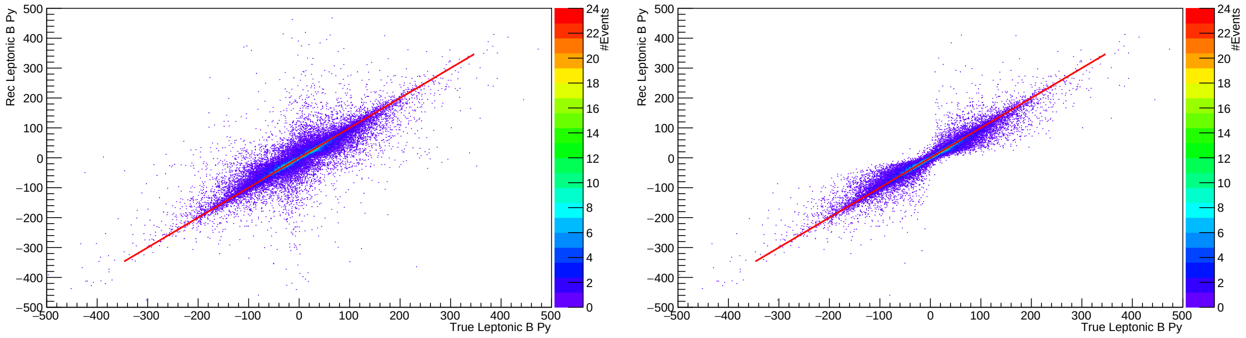

(C) P_y component (D) P_y comp. ($\Delta R < 0.4$)

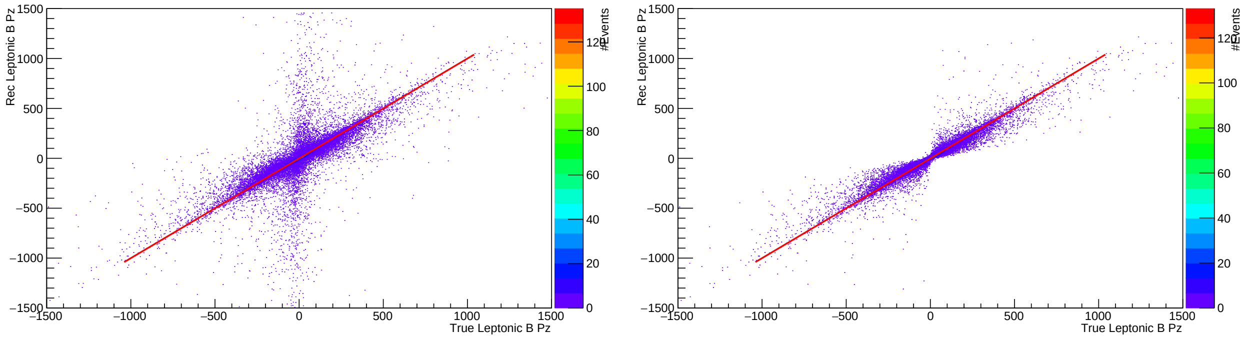

(E) P_z component (F) P_z comp. ($\Delta R < 0.4$)

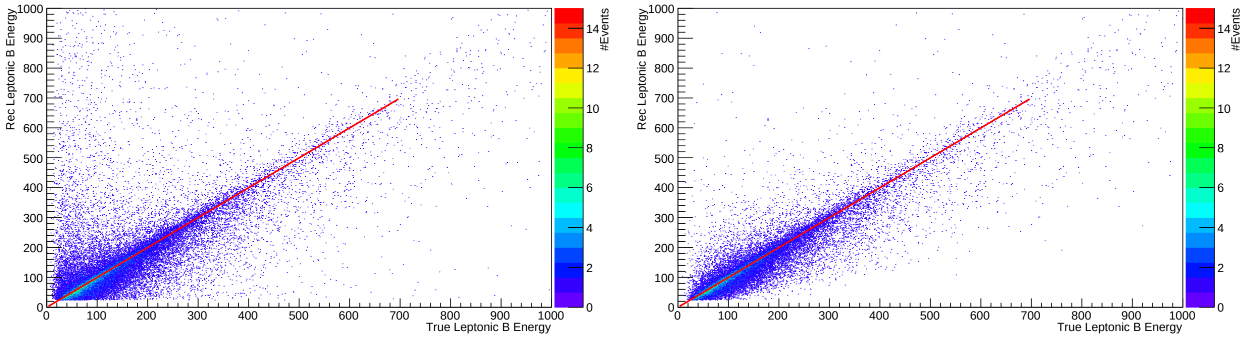

(G) E component (H) E comp. ($\Delta R < 0.4$)

FIGURE 5.4: 2D Plots of all momentum components of the Leptonic b jet. The vertical axis corresponds to the reconstructed object component and, the horizontal one, the true component. The red line indicates the linear ($m = 1$) regression line. Each row corresponds a different component. Starting with P_x and ending with the E component. Each column a different selection criteria. The first column corresponds to plain reconstructed objects by the *sum* algorithm, the second to objects that satisfy the matched criteria.

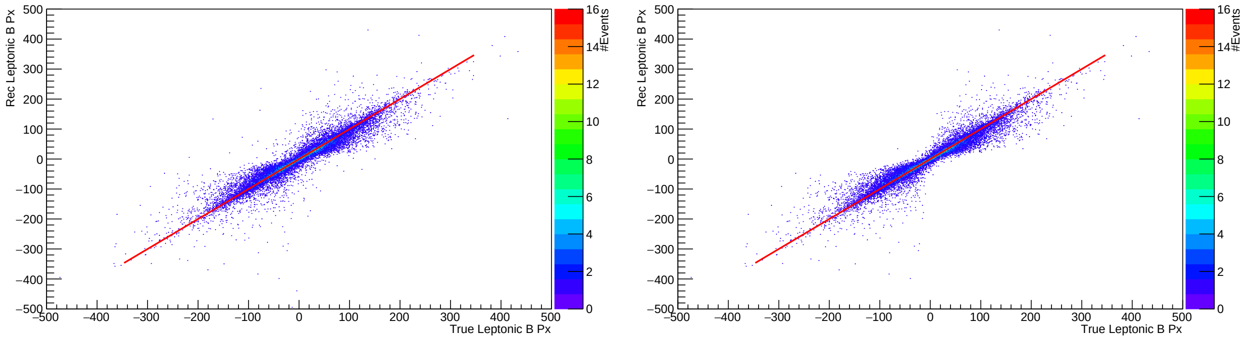

(A) P_x comp. (b-tagged)

(B) P_x comp. (both)

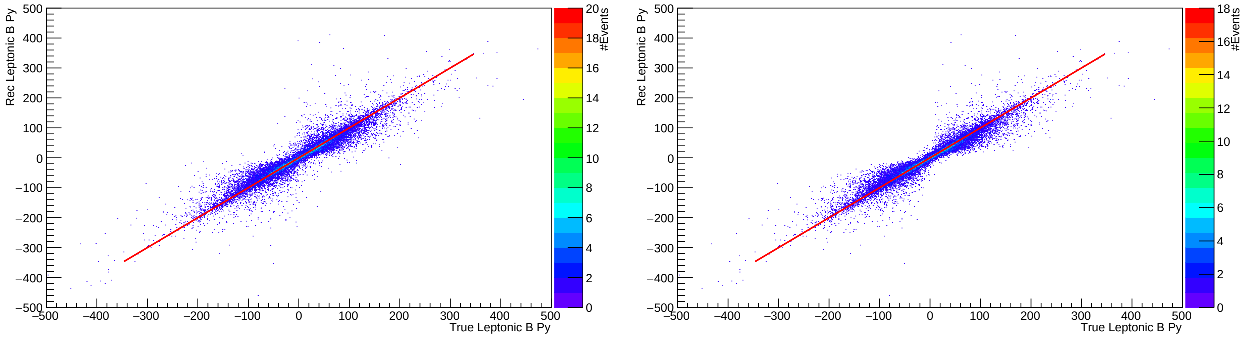

(C) P_y comp. (b-tagged)

(D) P_y comp. (both)

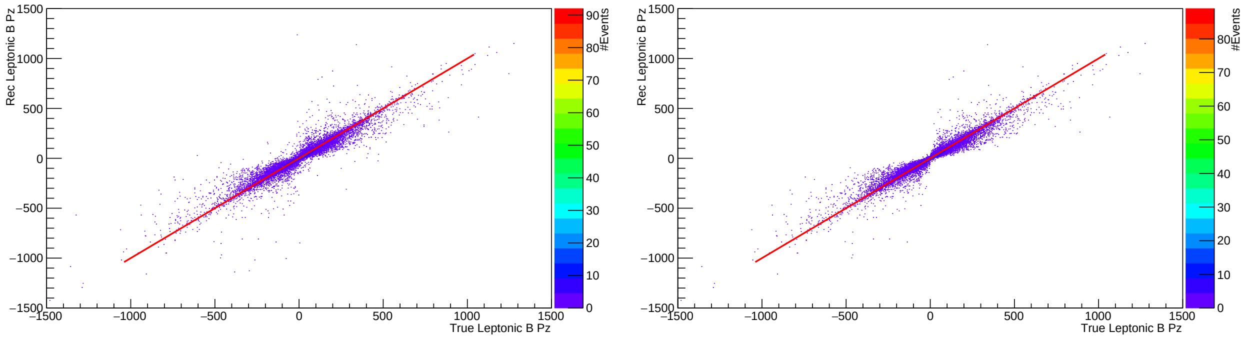

(E) P_z comp. (b-tagged)

(F) P_z comp. (both)

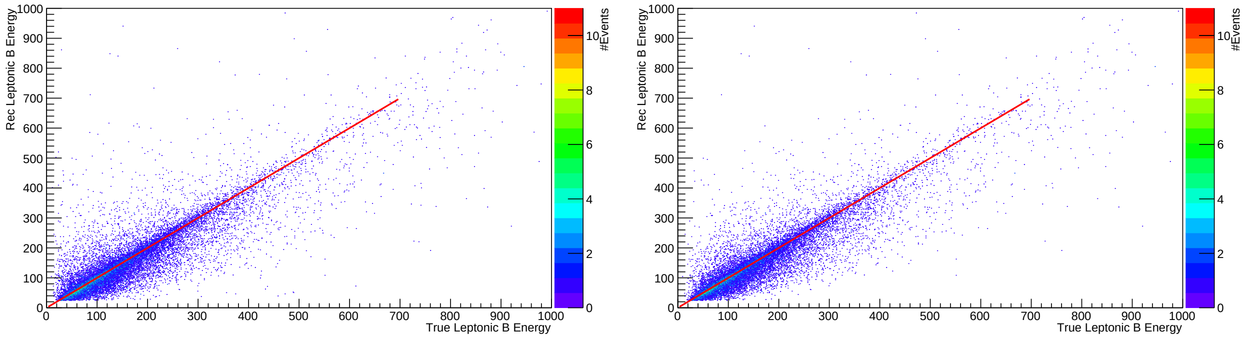

(G) E comp. (b-tagged)

(H) E comp. (both)

Figure 5.5: 2D Plots of all momentum components of the Leptonic b jet. The vertical axis corresponds to the reconstructed object component and, the horizontal one, the true component. The red line indicates the linear ($m = 1$) regression line. Each row corresponds a different component. Starting with P_x and ending with the E component. Each column a different selection criteria. The first column corresponds to b-tagged reconstructed objects, the second to b-tagged ones that also satisfy the matching condition.

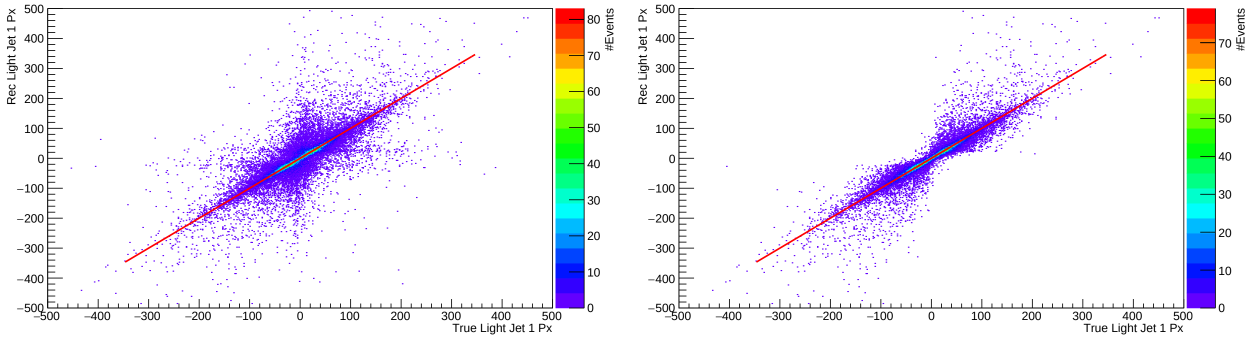

(A) P_x component (B) P_x comp. ($\Delta R < 0.4$)

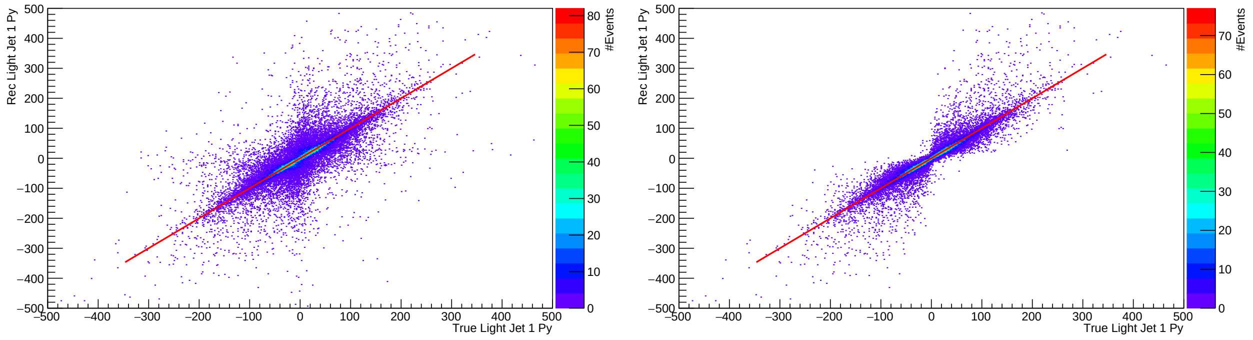

(C) P_y component (D) P_y comp. ($\Delta R < 0.4$)

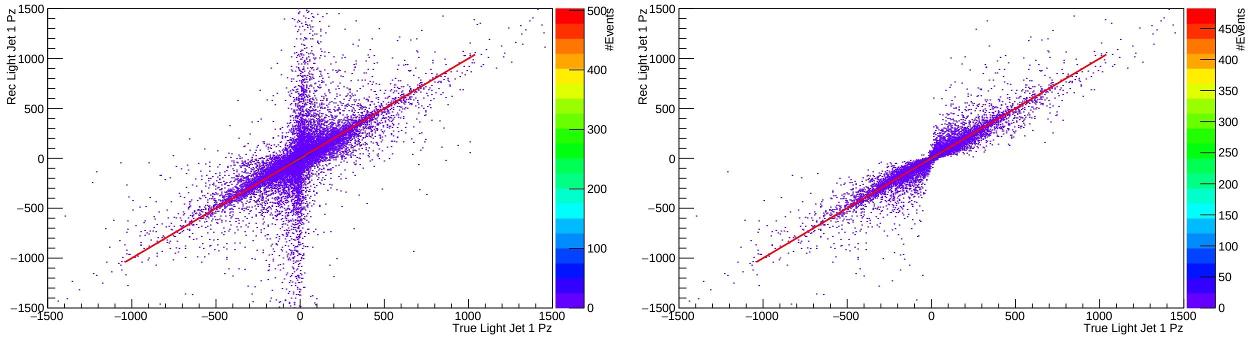

(E) P_z component (F) P_z comp. ($\Delta R < 0.4$)

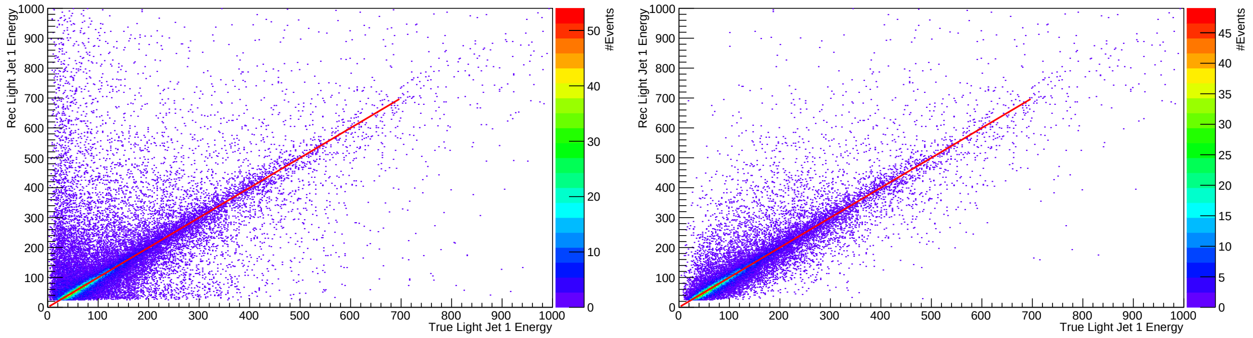

(G) E component (H) E comp. ($\Delta R < 0.4$)

FIGURE 5.6: 2D Plots of all momentum components of the Light Jet solution. The vertical axis corresponds to the reconstructed object component and, the horizontal one, the true component. The red line indicates the linear ($m = 1$) regression line. Each row corresponds a different component. Starting with P_x and ending with the E component. Each column a different selection criteria. The first column corresponds to plain reconstructed objects by the *sum* algorithm, the second to objects that satisfy the matched criteria.

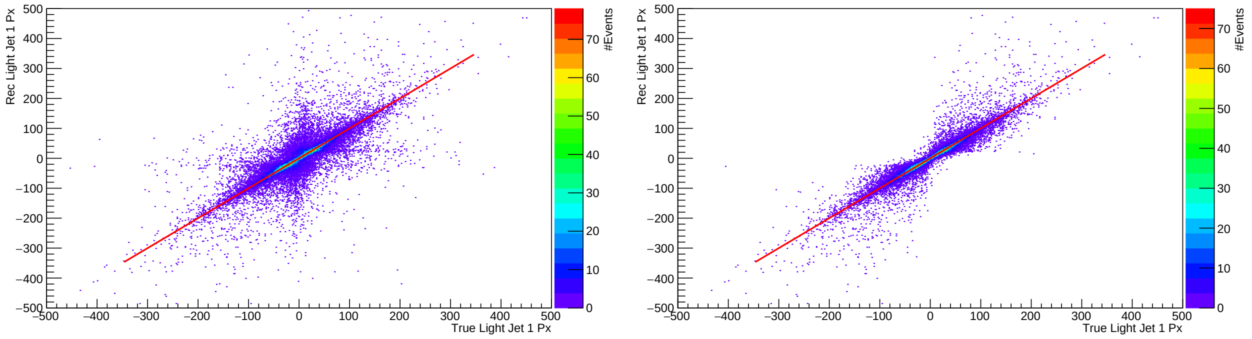

(A) P_x comp. (non b-tag)

(B) P_x comp. (both)

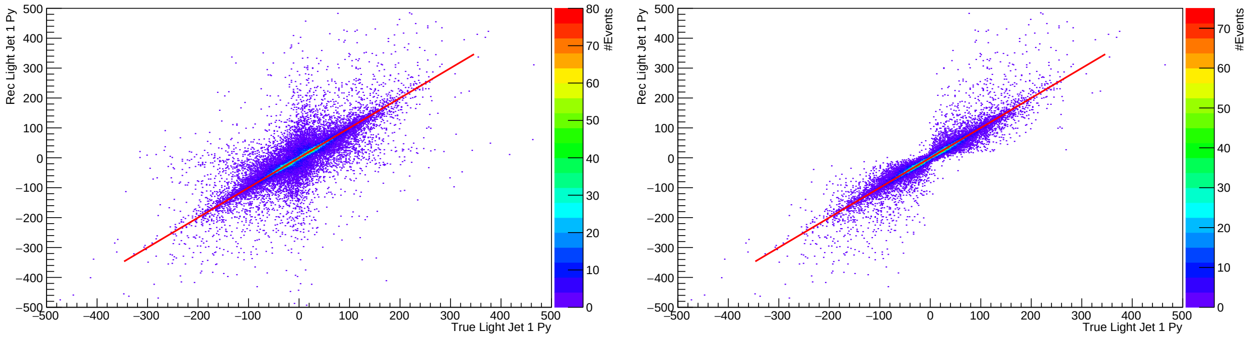

(C) P_y comp. (non b-tag)

(D) P_y comp. (both)

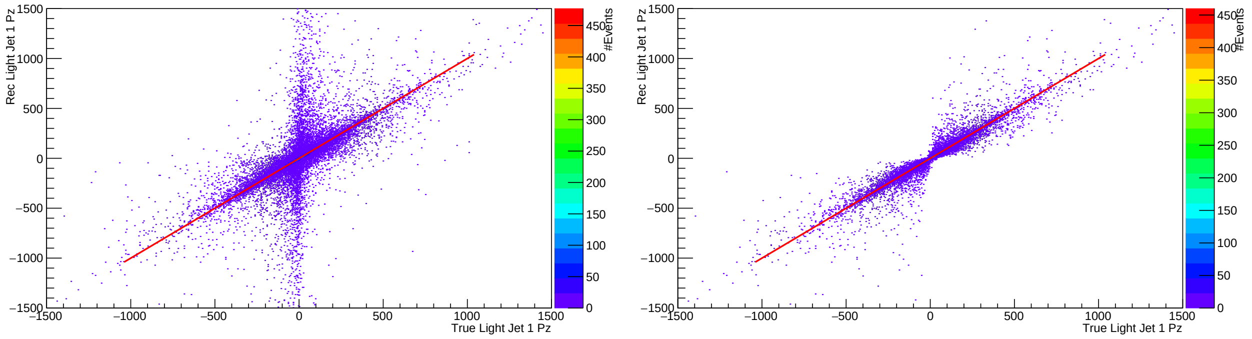

(E) P_z comp. (non b-tag)

(F) P_z comp. (both)

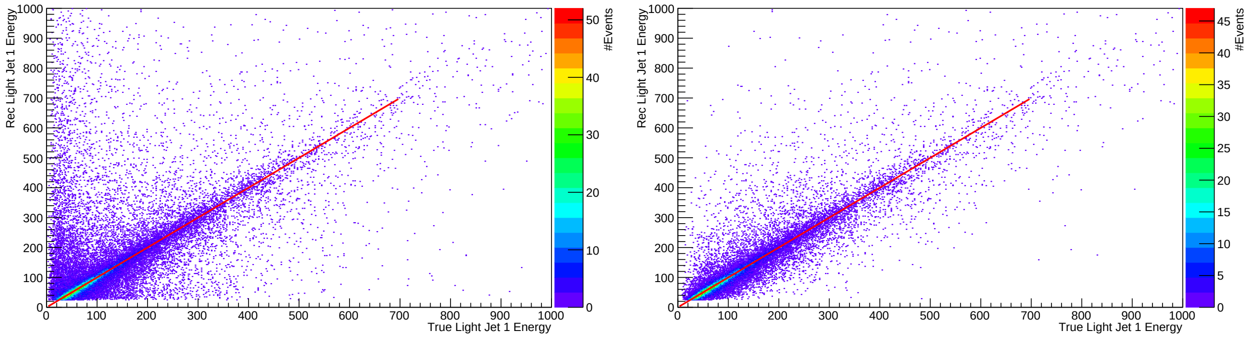

(G) E comp. (non b-tag)

(H) E comp. (both)

FIGURE 5.7: 2D Plots of all momentum components of the Light Jet solution. The vertical axis corresponds to the reconstructed object component and, the horizontal one, the true component. The red line indicates the linear ($m = 1$) regression line. Each row corresponds a different component. Starting with P_x and ending with the E component. Each column a different selection criteria. The first column corresponds to b-tagged reconstructed objects, the second to b-tagged ones that also satisfy the matching condition.

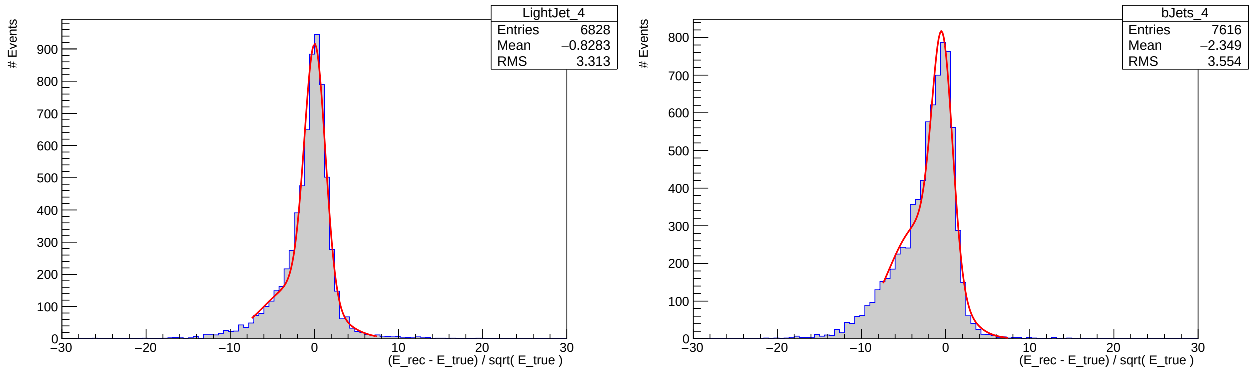

(A) Light Jets

(B) b Jets

FIGURE 5.8: Example of Transfer Functions for the light-quarks and b-quarks for the same regime of pseudorapidity and energy. In blue, the binned data from the events and, in red, a fitted double gaussian.

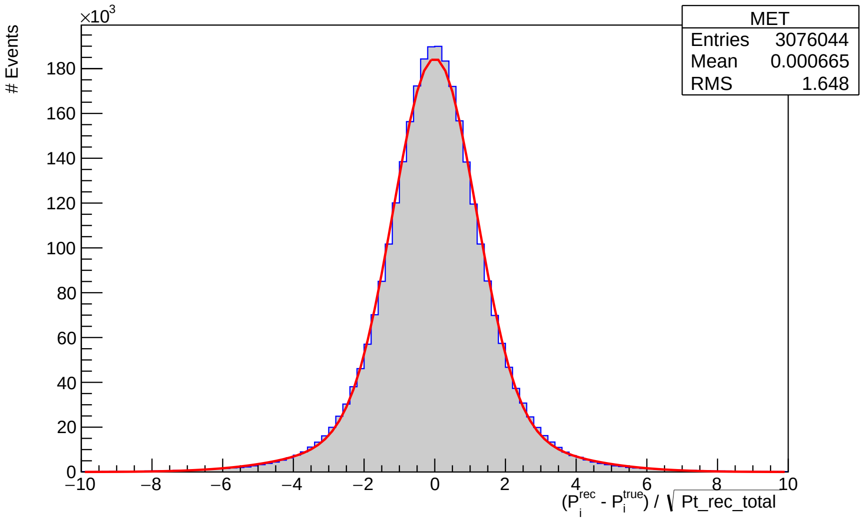

FIGURE 5.9: Transfer Function for the Missing Transverse Momentum. In blue, the binned data from the events and, in red, a fitted double gaussian.

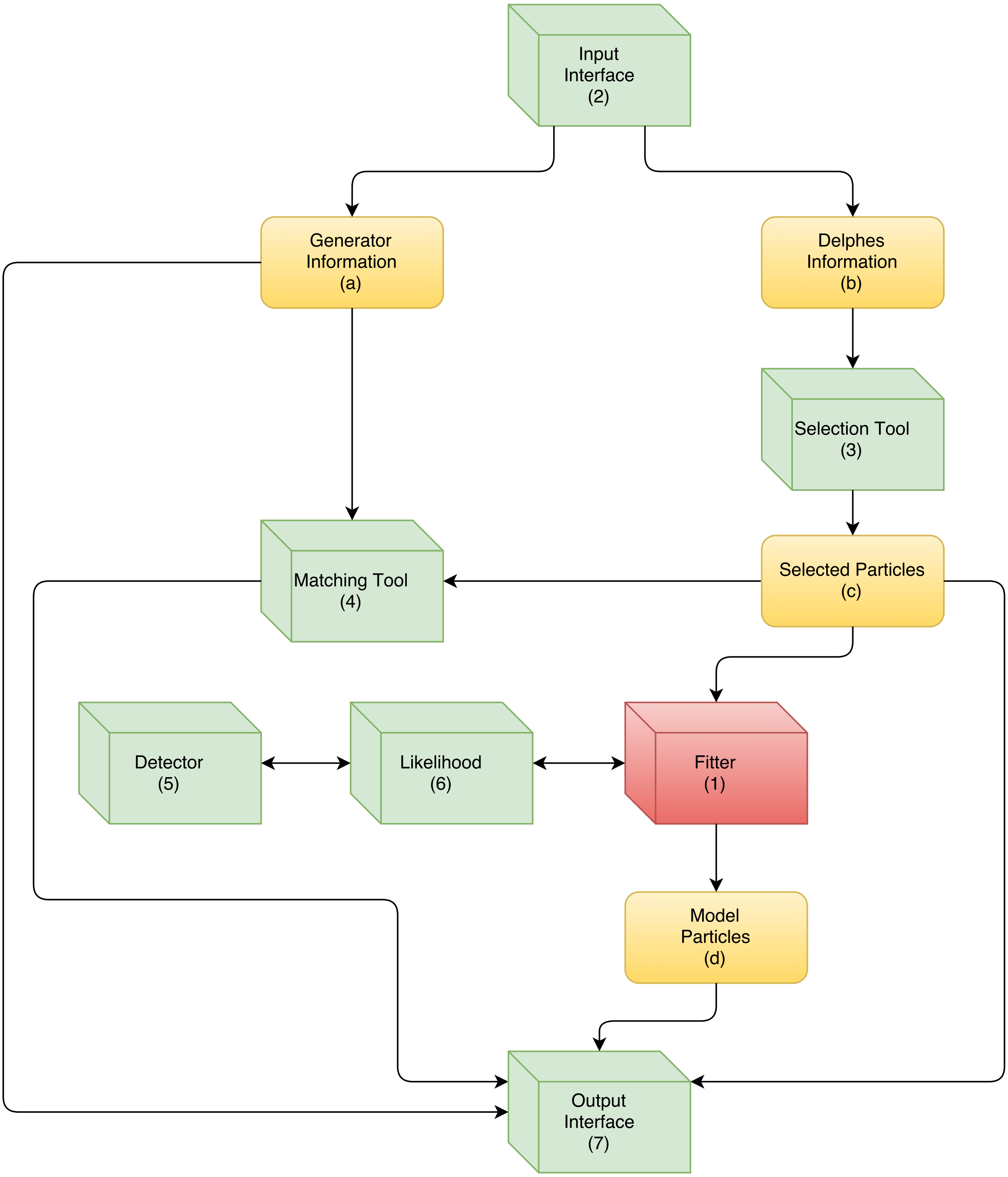

FIGURE 5.10: Diagrammatic representation of the modular structure and corresponding connections between the modules of the non-truth match reconstruction based on the KLFitter package. Boxes represent the moduli C++ objects while rectangles represent the corresponding event data.

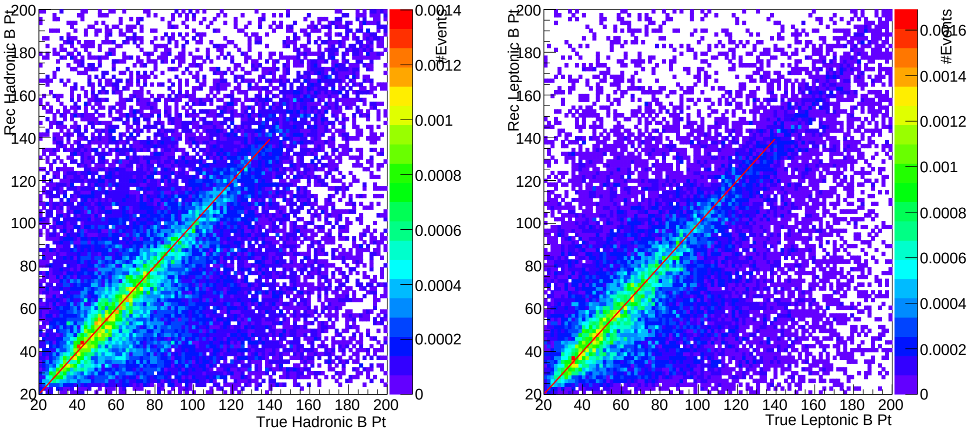

(A) Hadronic B

(B) Leptonic B

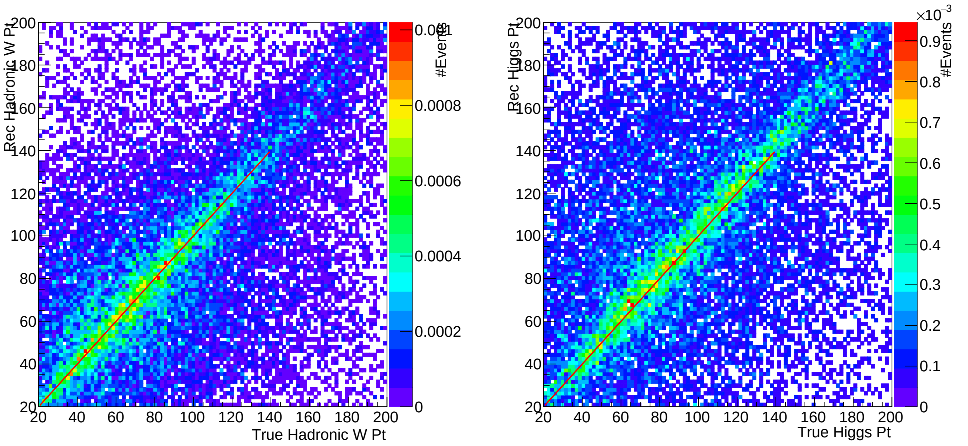

(C) Hadronic W

(D) Higgs

FIGURE 5.11: 2D Plots of the non-truth match reconstructed transverse momentum of the Hadronic b quark and W boson, Leptonic B and Higgs vs. their true counterparts. The colour scheme indicates the density of events per bin. The red line is the linear regression one, where perfect solutions would lay.

Chapter 6

CP Sensitive Variables

Following the event kinematic reconstruction, described in the previous chapter, it is possible to delve into variables that are sensitive to the scalar and pseudo-scalar components of the Higgs couplings to fermions, as well as, to their main backgrounds. The methodology is to set variables that are good in distinguishing samples of pure scalar, pure pseudo-scalar and background from each other. Following up with the use of a multivariate analysis. It will then be possible to draw 95% Confidence Level (CL) limits on the background hypothesis only. This will be the last step onto comparing the information with the ATLAS data.

6.1 Helicity Formalism

A common feature found in all known physical interactions is the conservation of energy and momentum. These imply time and translation invariance of the laws of physics in each reference frame[1], respectively. This is not the only conservation law found in nature, total angular momentum is another and has an important role. An intrinsic form of angular momentum is spin, which is carried out by all particles. Spin adds up to the total angular momentum of a particle, as such, conservation of total angular momentum imposes constrains on the particles' kinematics. This means that there is additional information to improve the detection of different processes, as the particles involved have different spins.

The helicity formalism [55] is a powerful tool to compute the angular distributions. The helicity operator

$$h = \vec{S} \cdot \hat{p} \tag{6.1}$$

is the projection of the spin vector operator along the direction of the particle's momentum. When a particle is at rest the helicity is, by convention, the spin projection along an arbitrary axis.

Let us start with the case of a two-body decay

$$a \to 1 + 2 \tag{6.2}$$

In the CM frame, the state of particle a, with mass m_a, spin J and spin projection along an arbitrary z-axis M is

$$|a\rangle = |\vec{p}_a = 0; JM\rangle \tag{6.3}$$

We are going to consider plane-wave states for the decay products $1+2$. If the decayed particles' momenta are $\vec{p}_1 = -\vec{p}_2 = \vec{p}$ in the CM system and their helicities λ_1 and λ_2, respectively, the state is just a direct product of the individual states

$$|\vec{p}_1\lambda_1; \vec{p}_2\lambda_2\rangle \equiv |\vec{p}_1; s_1, \lambda_1\rangle \otimes |\vec{p}_2; s_2, \lambda_2\rangle \tag{6.4}$$

The spin of each particle is fixed, thus can be omitted.

---

[1] One cannot say that energy or momentum are invariant though, as they depend on the reference frame considered.

There is a better way of representing this state. As the objects are back-to-back in the CM system, we can rewrite as

$$|p, \theta\varphi\lambda_1\lambda_2\rangle = |\vec{p}_1\lambda_1; \vec{p}_2\lambda_2\rangle \tag{6.5}$$

where the unit vector $\hat{n}(\theta,\varphi) = \hat{p}$ is along the decay axis, pointing to the direction of particle 1.

It is useful to factor out $|P^\alpha\rangle$ because the two-particle CM plane-wave states are eigenstates of the total 4-momentum $P^\alpha = P_1^\alpha + P_2^\alpha = (E,0,0,0)$ in the CM frame

$$|p, \theta\varphi\lambda_1\lambda_2\rangle = 8\pi^3 \left[\frac{4\sqrt{s}}{p}\right]^{\frac{1}{2}} |\theta\varphi\lambda_1\lambda_2\rangle \otimes |P^\alpha\rangle \tag{6.6}$$

where s is the *s-channel* Mandelstam's invariant, in this case $\sqrt{s} = m_a$.

The interaction responsible for the decay will, most likely, be dependent on the total momentum of the system. Angular momentum conservation, on the other hand, will only affect the direction of the decay products.

The amplitude for this process can now be written as

$$\mathcal{A}(a \to 1+2) = \langle\theta\varphi\lambda_1\lambda_2| U |JM\rangle\, S(P^\alpha) \tag{6.7}$$

where U is the interaction term that sets the helicities[2] of the new states and $S(P^\alpha)$ is related to the hard scattering part of the interaction, hence, can be ommited.

For a complete transition amplitude, the hard scattering function can always be multiplied to the respective angular distribution.

To exploit the conservation of angular momentum we have to change the basis to one of definite total angular momentum $|J_f M_f \lambda_1\lambda_2\rangle$, here the subscript f is referent to the final state particles, namely the system $1+2$.

$$\begin{aligned}\mathcal{A}(a \to f) &= \sum_{J_f, M_f} \langle\theta_f\varphi_F\lambda_1\lambda_2|J_f M_f\lambda_1\lambda_2\rangle \langle J_f M_f \lambda_1\lambda_2| U |JM\rangle \\ &= \sum_{J_f,M_f} \sqrt{\frac{2J+1}{4\pi}} D^{J_f *}_{M_f,\lambda_1-\lambda_2}(\varphi_f, \theta_f, -\varphi_f)\delta_{J_f,J}\delta_{M_f,M} \langle\lambda_1\lambda_2| U |M\rangle\end{aligned} \tag{6.8}$$

The pre-factors are normalization ones and the $D^j_{m',m}(\alpha,\beta,\gamma)$ functions are defined as

$$D^j_{m',m}(\alpha,\beta,\gamma) = e^{-i\alpha m'} d^j_{m'm}(\beta) e^{-i\gamma m} \tag{6.9}$$

$$\begin{aligned}d^j_{m'm}(\beta) = \sum_n \Bigg[&\frac{(-1)^n \sqrt{(j+m)!(j-m)!(j+m')!(j-m')!}}{(j-m'-n)!(j+m-n)!(n+m'-m)!n!} \\ &\times (\cos^{1/2}(\beta))^{2j+m-m'-2n}(-\sin^{1/2}(\beta))^{m'-m+2n}\Bigg]\end{aligned} \tag{6.10}$$

the sum is over all integers n where the arguments of the factorials are positive.

The $d^j_{m'm}(\beta)$ are given by the Wigner's formula which, along with the detailed procedure, is derived in the original reference. The subscripts m and m' in these functions are meant to be projections indexes (along a given axis) of spin j, as such, are restricted to the values $m, m' = -j, -j+1, \cdots, j$.

It is considered that every interaction preserves total angular momentum, thus, the matrix element $\langle\lambda_1\lambda_2| U |M\rangle$ is rotationally invariant by construction. We can simply write it as A_{λ_1,λ_2}. Then,

---

[2] Sets the chiralities in case the particles are massless.

simplifying the expression above we get

$$\boxed{\mathcal{A}(a \to f) = \sqrt{\frac{2J+1}{4\pi}} D^{J*}_{M,\lambda}(\varphi_f, \theta_f, -\varphi_f) A_{\lambda_1,\lambda_2}} \tag{6.11}$$

with $\lambda = \lambda_1 - \lambda_2$.

It is going to be enumerated some of the important functions given by the Wigner's formula in Table 6.1. The rest of the functions for each total spin J category can be obtained by the identity

$$d^j_{m',m}(\beta) = (-1)^{m'-m} d^j_{m,m'}(\beta) = d^j_{-m',-m}(\beta) \tag{6.12}$$

$J = 0$	$J = \frac{1}{2}$	$J = 1$
$d^0_{0,0} = 1$	$d^{1/2}_{1/2,1/2} = \cos\left(\frac{\beta}{2}\right)$ $d^{1/2}_{1/2,-1/2} = -\sin\left(\frac{\beta}{2}\right)$	$d^1_{1,1} = \frac{1+\cos(\beta)}{2}$ $d^1_{1,0} = -\frac{\sin(\beta)}{\sqrt{2}}$ $d^1_{1,-1} = \frac{1-\cos(\beta)}{2}$ $d^0_{0,0} = \cos(\beta)$

TABLE 6.1: The Wigner's formula for the first three spin categories. It is only necessary to consider these since no considered pair of elementary particle combines to form a higher value of total spin.

We may regard $t\bar{t}H$ production at the LHC as a decay chain of sucessive one-to-two processes, necessarily true at least for some of the Feynman diagrams of $t\bar{t}H$, as exemplified in Figure 6.1.

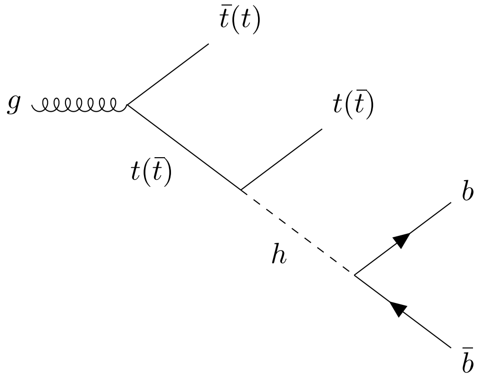

FIGURE 6.1: View of $t\bar{t}H$ events from a decay chain point of view.

The advantage of this formalism is that the full amplitude of some process is the product of amplitudes of the individual decay processes. For the one presented in Figure 6.1 the full decay amplitude is

$$\mathcal{A}(g \to t\bar{t}b\bar{b}) = \mathcal{A}(g \to t\bar{t})\mathcal{A}(t(\bar{t}) \to ht(\bar{t}))\mathcal{A}(h \to b\bar{b}) \tag{6.13}$$

For each decay, the flight direction of the decaying particle defines the spin quantization axis, in its CM frame. Maintaining the helicity states coherent in each decay step.

The cross-section is proportional to the modulus square of the full decay amplitude.

Since the helicities are not measurable at the LHC nor are the particles expected to be in definite helicites states, a sum of the cross sections over all helicities states is necessary. This returns the averaged angular distributions expected to be obtained.

6.2 Angular Variables

From the process depicted in Figure 6.1 we have three successive decays. These will define the three quantities related to the polar angles in the individual decay amplitudes in the helicity formalism. Figure 6.2 shows the angles' definition.

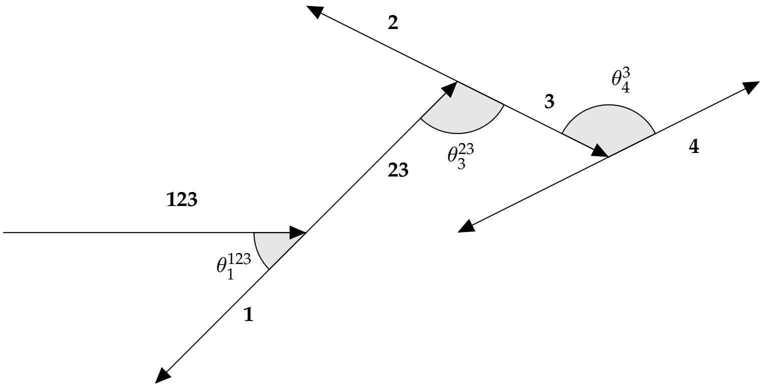

FIGURE 6.2: Diagrammatic representation of the $t\bar{t}H$ production as a decay chain, in the helicity formalism.

The first decay starts from the $t\bar{t}H$ center-of-mass system (123) which gives rise to system (1), recoiling from (23), in the (123) center-of-mass system. System (23) can, in turn, decay to system (3), that recoils back-to-back with system (2), in the (23) center-of-mass system. Finally, particle (4) decays along with another from particle (3). The particle's angles are the angles between particles' direction of flight, measured in the center-of-mass system of its mother, with respect to the axis defined by the mother's direction of flight in its own mother's center-of-mass.

From the top decay spin correlation[3] (1.11), and from the structure of the individual decay amplitudes[4], it is expected a product of trigonometric functions of these angles for the cross section of $t\bar{t}H$ production.

Upon survey of the full phase-space, two large families of functions showed better discriminant power between signal and background,

$$f(\theta_1^{123})g(\theta_4^3) \quad \text{and} \quad f(\theta_3^{23})g(\theta_4^3) \tag{6.14}$$

where both $f(x)$ and $g(x)$ are trigonometric functions to the power of an arbitrary integer.

The purpose is twofold. First, to find a set of functions that allow good discriminating between $h = H$, a pure scalar Higgs, and $h = A$, a pure pseudo scalar Higgs. Secondly, to find another set that allows to distinguish effectively scalar Higgs signal from dominant background.

Mathematically, the angles are defined by reference systems, hence, we can permute the different particles through the positions of those systems. Furthermore, since the top quarks will decay weakly, their products can also be taken to compute the best set of distributions.

There is an undressed ambiguity on how the systems are obtained from the reconstructed objects. To compute the angles, several Lorentz boosts are necessary to obtain the different CM systems from the laboratory frame (LAB).

Since the generators of the Lorentz boosts do not commute

$$[K_i, K_j] = -i\epsilon_{ijk}J_k \tag{6.15}$$

---

[4] Derived from the helicity formalism.

[4] Idem.

boosting to another CM system from the LAB frame directly or through sequential boosts leads to different values for the angular variables. Both direct and sequential boosts were studied and used. The (seq) prefix indicates that the objects necessary to compute θ_4^3 were boosted *sequentially*. The objects evaluated in the LAB frame, are boosted through each one of the systems before reaching the CM reference frame (3).

The choice of variables was based on the best forward-backward asymmetry, as well as, the set of variables that presented the lowest correlation among them. The angular variables used are

$$\begin{aligned}
A_1 &= \text{(seq) } \sin\theta_h^{t\bar{t}h} \times \cos\theta_{b_h}^{\bar{t}} \\
A_2 &= \text{(seq) } \sin\theta_h^{t\bar{t}h} \times \sin\theta_{W+}^{h} \\
A_3 &= \cos\theta_h^{\bar{t}h} \times \sin\theta_{l^-}^{h} \\
A_4 &= \text{(seq) } \sin\theta_h^{t\bar{t}h} \times \sin\theta_{b_{\bar{t}}}^{\bar{t}} \\
A_5 &= \text{(seq) } \sin\theta_{\bar{t}}^{t\bar{t}h} \times \sin\theta_{b_h}^{h} \\
A_6 &= \sin\theta_h^{t\bar{t}h} \times \sin\theta_{\bar{t}}^{t\bar{t}}
\end{aligned} \tag{6.16}$$

In general, the values of the angles in each event will be in the range $0 \leq \theta \leq \pi$. As such, the A_n will inherit the corresponding domain. Hence, histograms will be created representing the number of events per bin $[x, x+\delta[\in \mathcal{D}(A_n)$. In Figure 6.3 the angular distributions are shown.

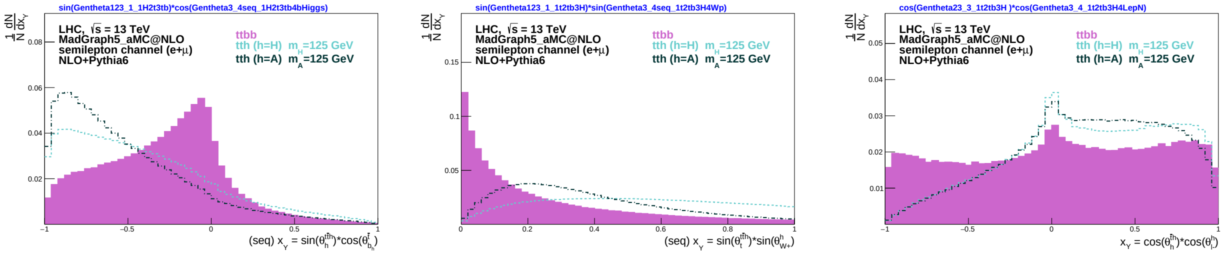

(A) First Distribution (B) Second Distribution (C) Third Distribution

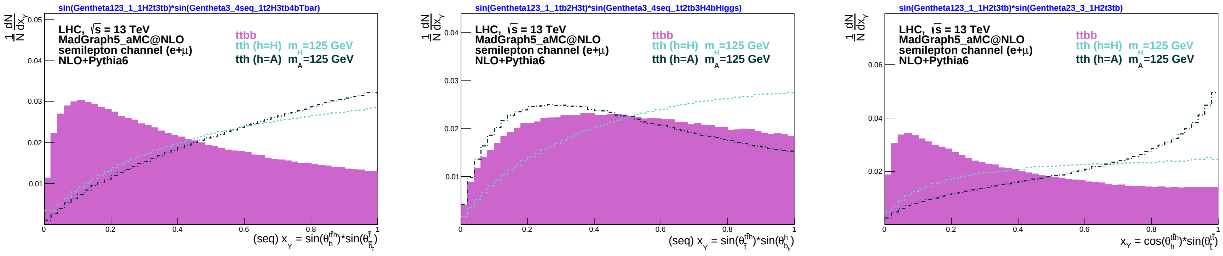

(D) Fourth Distribution (E) Fifth Distribution (F) Sixth Distribution

FIGURE 6.3: Gen. angular distributions. There are several Plots that distinguish between the Higgs components and dominant background, others that distinguish between types of Higgs signal. Distributions are normalized.

A forward-backward asymmetry, A_{FB}, associated to each one of the angular distributions, is the difference between the cross section above a specific cut-off value x^* and the cross section below that value, normalized to the total cross section,

$$A_{\text{FB}} = \frac{\sigma(x > x^*) - \sigma(x < x^*)}{\sigma(x > x^*) + \sigma(x < x^*)} \tag{6.17}$$

For distributions containing only product of sines, one has $x^* = 0.5$ otherwise $x^* = 0$.

Figure 6.4 shows the forward-backward asymmetries, A_{FB}, to both signals and dominant background. The way in which the variables correlations is computed is given in the next section.

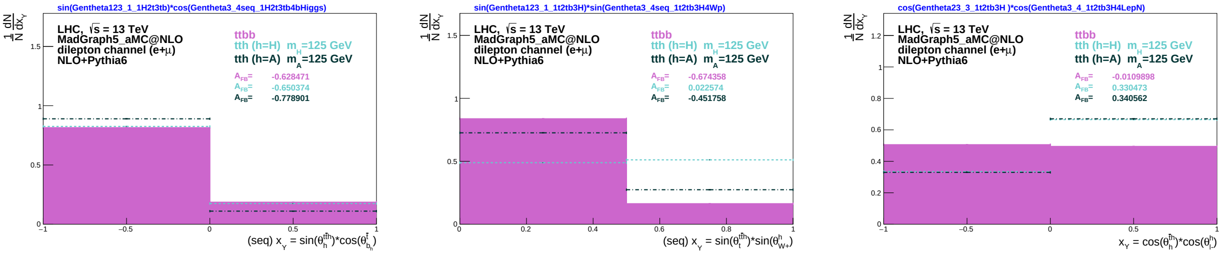

(A) First Distribution (B) Second Distribution (C) Third Distribution

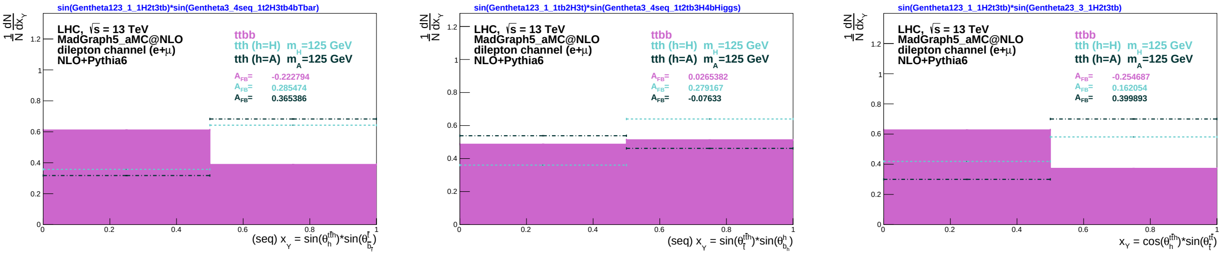

(D) Fourth Distribution (E) Fifth Distribution (F) Sixth Distribution

FIGURE 6.4: Gen. angular distributions with just two bins for asymmetry study. There are several Plots that distinguish between the Higgs components and dominant background, others that distinguish between types of Higgs signal. Distributions are normalized.

The angular distributions were computed for the parton level, reconstruction with and without truth match levels. For each level, one observes a decrease in quality of the distributions, which was expected. In general they flatten up, making the reconstructed without truth match distributions less discriminant. Nevertheless, all chosen distributions preserve a good level of differentiability. Figure 6.5 shows the distributions after reconstruction without truth match.

Figure 6.6 shows the forward-backward asymmetries where the same flattening is observed.

Despite the visible deterioration, the distributions kept some discriminant power between signal and background. It should be stressed that no optimization of the true analysis was done, to best separate signals from background. These studies stay largely outside the scope of this thesis.

6.3 Additional CP Variables

Another set of variables was also studied in this thesis [38]. These variables are theoretically sensitive to the $a_t^2 - b_t^2$ term, which come from the spin average cross section, where a_t and b_t are the scalar and pseudo-scalar components of the $t\bar{t}H$ coupling, respectively. The variables are

$$\begin{aligned} a_1 &= \frac{(\vec{p}_t \times \hat{n}) \cdot (\vec{p}_{\bar{t}} \times \hat{n})}{|(\vec{p}_t \times \hat{n}) \cdot (\vec{p}_{\bar{t}} \times \hat{n})|} & a_2 &= \frac{p_t^x p_{\bar{t}}^x}{|p_t^x p_{\bar{t}}^x|} \\ b_1 &= \frac{(\vec{p}_t \times \hat{n}) \cdot (\vec{p}_{\bar{t}} \times \hat{n})}{p_t^T p_{\bar{t}}^T} & b_2 &= \frac{(\vec{p}_t \times \hat{n}) \cdot (\vec{p}_{\bar{t}} \times \hat{n})}{|\vec{p}_t||\vec{p}_{\bar{t}}|} \\ b_3 &= \frac{p_t^x p_{\bar{t}}^x}{p_t^T p_{\bar{t}}^T} & b_4 &= \frac{p_t^z p_{\bar{t}}^z}{|\vec{p}_t||\vec{p}_{\bar{t}}|} \end{aligned} \tag{6.18}$$

with $\hat{n}$ being the direction along the beam pipe (the z-axis).

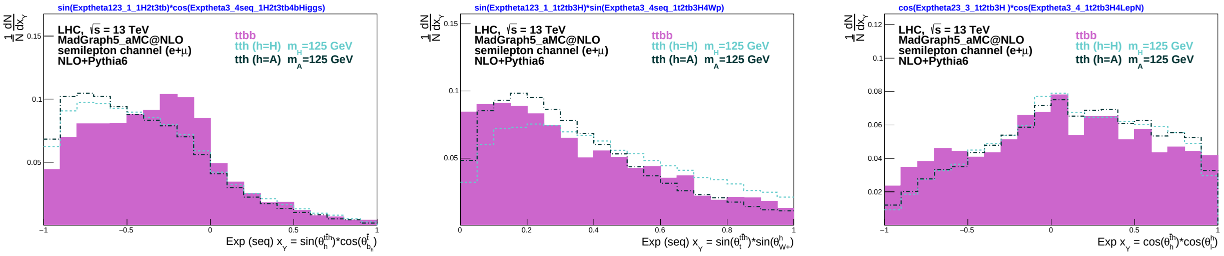

(A) First Distribution (B) Second Distribution (C) Third Distribution

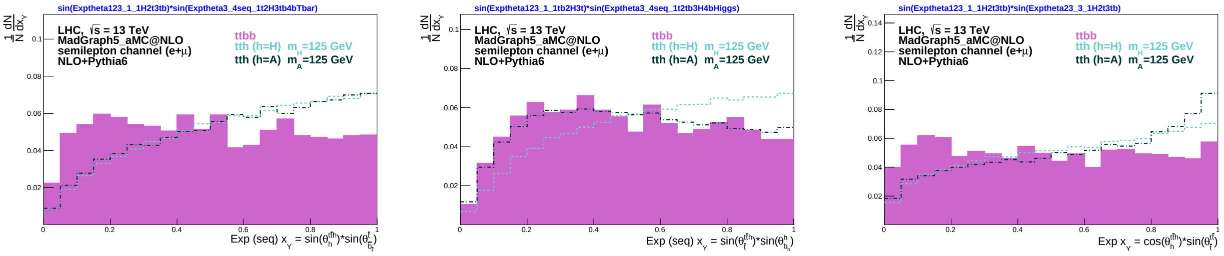

(D) Fourth Distribution (E) Fifth Distribution (F) Sixth Distribution

FIGURE 6.5: Model level angular distributions. There are several Plots that distinguish between the Higgs components and dominant background, others that distinguish between types of Higgs signal. Distributions are normalized.

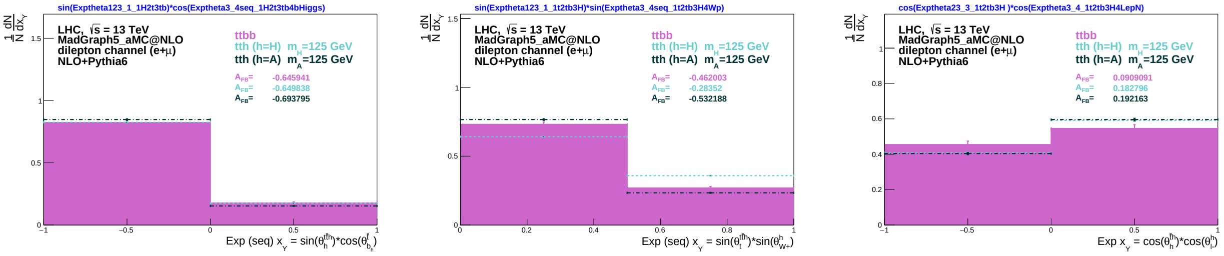

(A) First Distribution (B) Second Distribution (C) Third Distribution

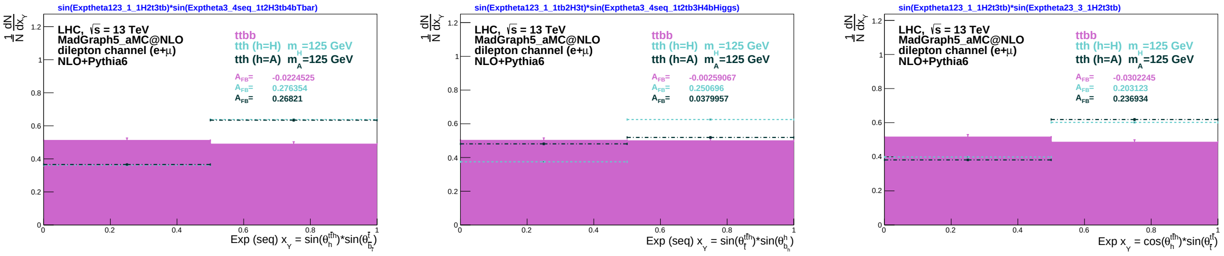

(D) Fourth Distribution (E) Fifth Distribution (F) Sixth Distribution

FIGURE 6.6: Model level angular distributions. There are several Plots that distinguish between the Higgs components and dominant background, others that distinguish between types of Higgs signal. Distributions are normalized.

For this specific analysis, the only variable that shows good discrimination between signal and background is b_4. Figure 6.7 shows the parton level distribution of this variable and Figure 6.8 the reconstructed without truth match level counterpart.

Analogously to the angular variables studied already, the discriminant power is retained to some extent. In this case it adds an important piece of information to distinguish CP even/odd Higgs couplings. Hence, it will be added to the set used in multivariate analysis.

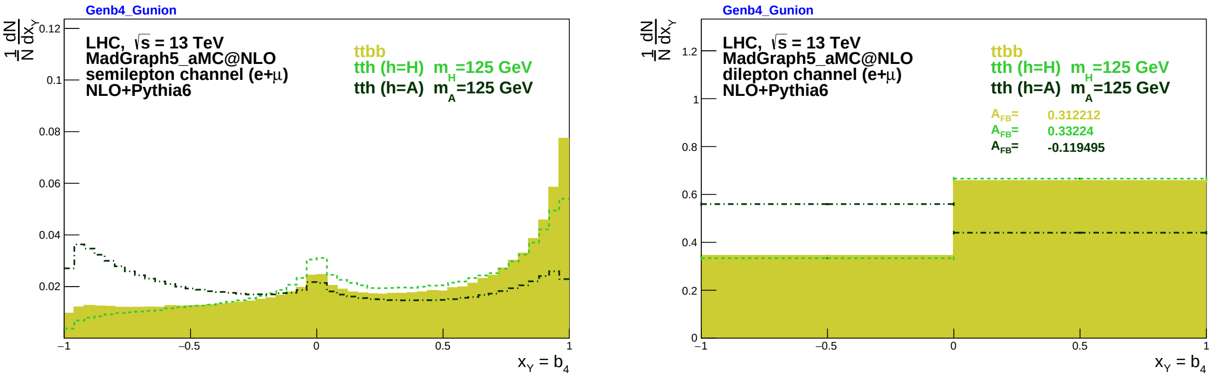

(A) Full b_4 Distribution

(B) A_{FB} values of the b_4 Distribution

FIGURE 6.7: Parton Level b_4 variable for the different samples. On the left, the full distribution. On the right, the forward backward asymmetry of the distribution

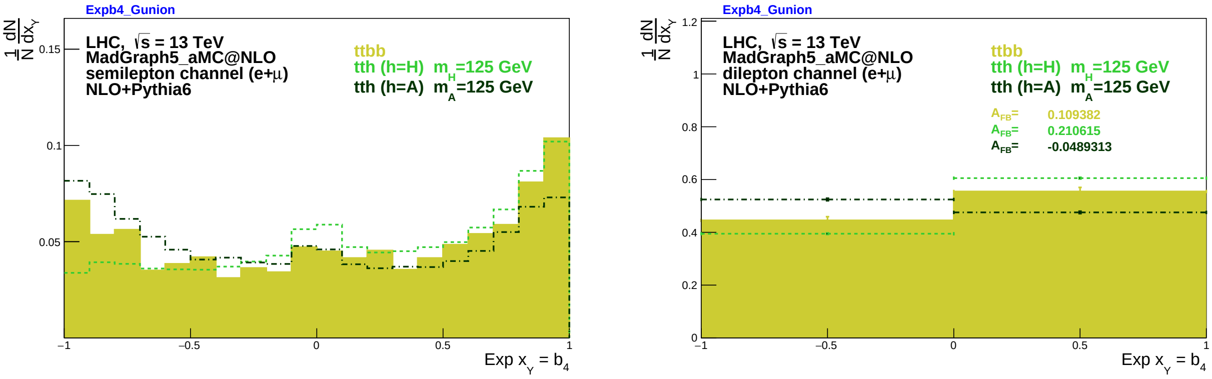

(A) Full b_4 Distribution

(B) A_{FB} values of the b_4 Distribution

FIGURE 6.8: Exp. Level b_4 variable for the different samples. On the left, the full distribution. On the right, the forward backward asymmetry of the distribution

To summarize, the forward-backward asymmetries obtained are presented in Table 6.2, at parton level and after reconstruction without truth match.

Asymmetry	Generator Level		Experimental Level	
	$t\bar{t}H/t\bar{t}A$	$t\bar{t}b\bar{b}$	$t\bar{t}H/t\bar{t}A$	$t\bar{t}b\bar{b}$
$A_{\text{FB}}^{l^-(h)}$	+0.330/+0.341	-0.011	+0.104/+0.166	-0.005
$A_{\text{FB}}^{b_{\bar{t}}(\bar{t})}$ (seq.)	+0.285/+0.365	-0.223	+0.204/+0.186	-0.086
$A_{\text{FB}}^{b_h(\bar{t})}$ (seq.)	-0.650/-0.779	-0.223	-0.672/-0.717	-0.650
$A_{\text{FB}}^{W^+}$ (seq.)	+0.023/-0.452	-0.674	-0.327/-0.512	-0.513
$A_{\text{FB}}^{b_h(h)}$ (seq.)	+0.279/-0.076	+0.027	+0.184/+0.015	-0.050
$A_{\text{FB}}^{\bar{t}(t\bar{t})}$	+0.162/+0.400	-0.255	+0.156/+0.154	-0.107
$A_{\text{FB}}^{b_4}$	+0.332/-0.119	+0.312	+0.167/-0.076	+0.058

TABLE 6.2: Summarized table with forward-backward asymmetries of the chosen variables for parton (generator) and reconstructed without truth match (experimental) levels.

6.4 Background Contributions

Let us see the individual contribution of each of the backgrounds to the different values of the chosen signal/background and CP sensitive variables. All cross sections used are computed in `MadGraph5_aMC@NLO`, except for the top quark single- and pair production, as more accurate theoretical results are available at NNLO+NNLL with gluon resummation for top quark pair production [30] and NNLO for single top production [19]. The cross sections of these generated processes were normalized to the most precise theoretical predictions.

We can use the parametrisation of the mass dependence of the cross section, given by

$$\sigma(m) = \sigma(m_{\text{ref}}) \left(\frac{m_{\text{ref}}}{m}\right)^4 \left(1 + a_1 \frac{m - m_{\text{ref}}}{m_{\text{ref}}} + a_2 \left[\frac{m - m_{\text{ref}}}{m_{\text{ref}}}\right]^2\right) \tag{6.19}$$

with $m_{\text{ref}} = 172.5$ GeV, to compute the most accurate value of the production cross sections of the top quark (single and pair production). The value of the top mass used in this study is $m_t = 173$ GeV. Table 6.3 displays the computed values of σ_{ref}, a_1 and a_2 using the `NNPDF2.3` PDF sets, for both the $t\bar{t}$ and single top.

Channel	σ_{ref} (pb)	a_1	a_2
Single top (s-channel)	6.3651	0.4211	-0.1931
Single anti-top (s-channel)	4.0138	0.2466	-0.1909
Single top (t-channel)	137.4581	2.645	1.831
Single anti-top (t-channel)	83.0066	2.567	1.657
Top pair	843.483	-0.745	0.127

TABLE 6.3: Reference values of the cross section and respective mass parametrization parameters for the top quark single- and pair production computed with `NNPDF2.3`. Reference mass is $m_{\text{ref}} = 172.5$ GeV. Mass used for generation is $m_t = 173$ GeV.

The single lepton branching ratio value is

$$\text{BR(Single Lepton)} = 2 \cdot \text{BR}(W^\pm \to \text{light jets}) \cdot \text{BR}(W^\pm \to l^\pm \nu) \tag{6.20}$$

where the factor two takes into account both top and anti-top quark decays. The most accurate results are given in by the Particle Data Group [50]:

$$\text{BR(Single Lepton)} = 0.2877 \tag{6.21}$$

Table 6.4 enumerates the generated background with their respective cross sections per cut.

Only events that survive all cuts are taken for analysis. Table 6.5 shows the cross section of the surviving events after all cuts, with the respective *efficiency*, which is just the ratio of selected events with respect to the total number of generated events. The weight per event is defined as

$$w(\mathcal{L}) = \frac{\mathcal{L}\sigma}{N_{\text{gen}}} \tag{6.22}$$

where N_{gen} is the generated number of events of a certain process, $\mathcal{L}$ the integrated luminosity and σ the cross section of that process.

If the luminosity of the collisions is taken as

$$\mathcal{L} = 100 \text{ fb}^{-1} \tag{6.23}$$

Parton State	Generated Cross section (pb)	$N_j > 6$ & $N_l = 1$ Cross section (pb)	E/P_t & η cuts Cross section (pb)
(NLO) $t\bar{t}b\bar{b}$	$\sigma_{t\bar{t}b\bar{b}} = 4.708 \times 10^0$	8.984×10^{-1}	7.470×10^{-1}
(LO) $t\bar{t}3j$	$\sigma_{t\bar{t}3j} = 2.393 \times 10^2$	2.488×10^1	2.061×10^1
(LO) $t\bar{t}Vj$	$\sigma_{t\bar{t}Vj} = 3.243 \times 10^0$	7.490×10^{-2}	6.498×10^{-2}
(LO) sT (s-chan)	$\sigma_{sts} = 2.192 \times 10^0$	7.773×10^{-3}	6.219×10^{-3}
(LO) sT (t-chan)	$\sigma_{stt} = 4.686 \times 10^1$	4.852×10^{-1}	3.725×10^{-1}
(LO) $w4j$	$\sigma_{w4j} = 3.450 \times 10^4$	3.293×10^0	2.779×10^0
(LO) $wbb2j$	$\sigma_{wbb2j} = 2.893 \times 10^2$	7.097×10^{-1}	5.648×10^{-1}
(LO) $ww3j$	$\sigma_{ww3j} = 8.424 \times 10^1$	1.927×10^{-1}	1.627×10^{-1}
(LO) $wz3j$	$\sigma_{wz3j} = 3.793 \times 10^1$	9.420×10^{-2}	7.926×10^{-2}
(LO) $zz3j$	$\sigma_{zz3j} = 1.100 \times 10^1$	8.662×10^{-3}	5.962×10^{-3}
(NLO) $t\bar{t}H$	$\sigma_{t\bar{t}H} = 1.384 \times 10^{-1}$	2.661×10^{-2}	2.237×10^{-2}
(NLO) $t\bar{t}A$	$\sigma_{t\bar{t}A} = 5.822 \times 10^{-2}$	1.893×10^{-2}	1.524×10^{-2}

TABLE 6.4: Generated Background and successively applied cuts. The initial cross sections and for each cut. For comparison there is the two Higgs signals at the end of the table.

Parton State	Prev. Cuts + $N_j \leq 8$ & $3 \leq N_b \leq 4$ Cross section (pb)	Efficiency
(NLO) $t\bar{t}b\bar{b}$	$\sigma_{t\bar{t}b\bar{b}} = 1.656 \times 10^{-1}$	3.518×10^{-2}
(LO) $t\bar{t}3j$	$\sigma_{t\bar{t}3j} = 5.655 \times 10^{-1}$	2.362×10^{-3}
(LO) $t\bar{t}Vj$	$\sigma_{t\bar{t}Vj} = 4.133 \times 10^{-3}$	1.276×10^{-2}
(LO) sT (s-chan)	$\sigma_{sts} = 1.508 \times 10^{-4}$	6.88×10^{-5}
(LO) sT (t-chan)	$\sigma_{stt} = 4.780 \times 10^{-3}$	1.023×10^{-4}
(LO) $w4j$	$\sigma_{w4j} = 0$	0
(LO) $wbb2j$	$\sigma_{wbb2j} = 3.716 \times 10^{-3}$	1.286×10^{-5}
(LO) $ww3j$	$\sigma_{ww3j} = 0$	0
(LO) $wz3j$	$\sigma_{wz3j} = 4.529 \times 10^{-4}$	1.195×10^{-5}
(LO) $zz3j$	$\sigma_{zz3j} = 5.095 \times 10^{-5}$	4.632×10^{-6}
(NLO) $t\bar{t}H$	$\sigma_{t\bar{t}H} = 8.846 \times 10^{-3}$	6.394×10^{-2}
(NLO) $t\bar{t}A$	$\sigma_{t\bar{t}A} = 6.067 \times 10^{-3}$	1.042×10^{-1}

TABLE 6.5: Surviving events' cross sections after all cuts were applied. The efficiency, defined as the ratio of the all cuts cross section with its original value, of each background and signal is also shown.

it is possible to predict the total event yields by multiplying the cross section values of Tables 6.4 and 6.5. Figure 6.9 shows the expected angular distributions for $\mathcal{L} = 100$ fb^{-1}. After all cuts there are only a few events remaining in some backgrounds

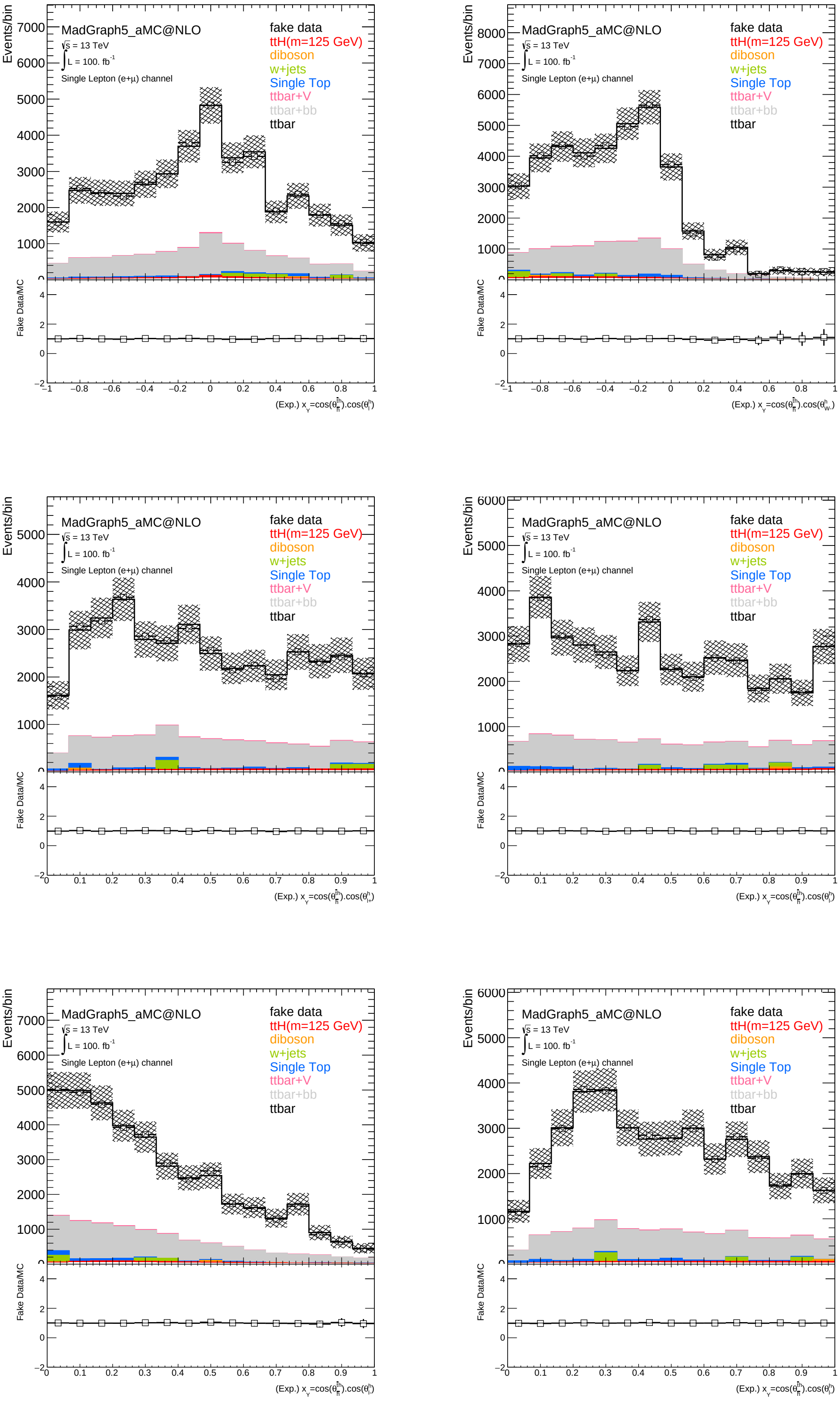

FIGURE 6.9: Angular variables computed for all backgrounds and scalar signal with their expected relative contributions.

6.5 Multivariate Analysis

A multivariate analysis was used to combine the different angular distributions to generate multivariate probability distributions for signal and SM background. Several methods exists to construct these functions, some more powerful than others. For the chosen set of variables, several multivariate methods were implemented, using the `TMVA` toolkit [39]. The ones with better performance are:

- The likelihood method.
- Fisher's method [11].
- Several boosted decision trees (BDT) methods [62].

The set of variables chosen to build the discriminating variable were the ones that showed the highest discriminating power between signal and background and were less correlated. Figure 6.10 depicts the correlation between the chosen set of variables for the $t\bar{t}H$ signal and $t\bar{t}b\bar{b}$ dominant background.

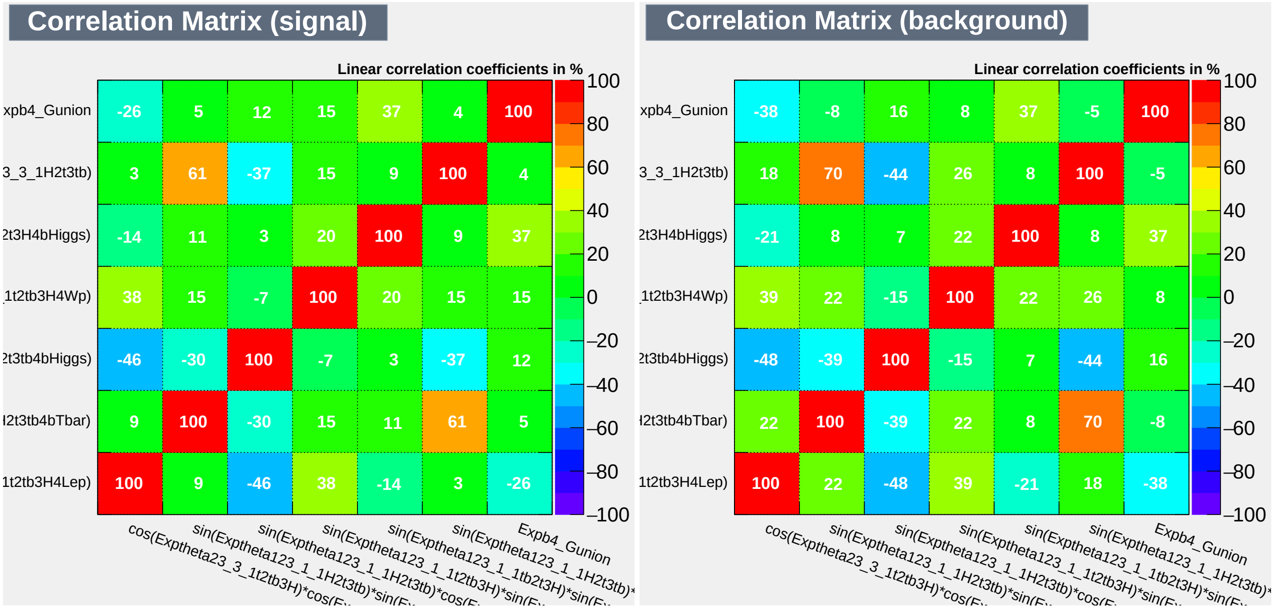

(A) Signal (B) Background

FIGURE 6.10: Correlation matrices of the set of chosen variables for (A) signal- and (B) background events.

Only $t\bar{t}b\bar{b}$ events are considered as background to train the multivariate methods. This is motivated by being the dominant background and by the fact that considering more than one type of background may mix different samples with unknown cross sections.

For each multivariate method, the signal and background samples are divided in two parts with equal number of events. The first part is used to *train* the methods, namely, to construct the probability distribution functions that distinguish signal and background, considering only events from this set. The second set validates the training in case the second sample follows the distribution constructed from the first one.

All of the methods can be used as binary classifiers. A certain event will either be considered signal or background depending if it has a larger or smaller value of a specific defined cut. The receiver operating characteristic (ROC) curve, illustrates the performance of each method, by displaying the relation of signal efficiency (taking a signal event as signal) vs. background rejection (taking a background event as background) for each possible threshold. Figure 6.11 shows these curves and the best method: the Fisher one.

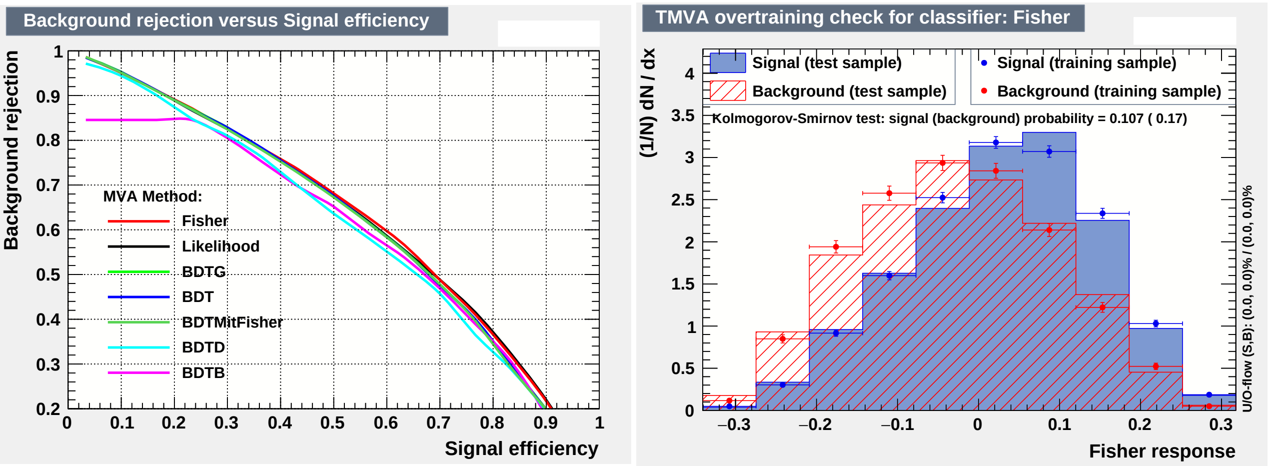

(A) ROC curve (B) Overtraining with Fisher

FIGURE 6.11: Receiver operating characteristic curve (A) and Multivariate training sample and over-training test sample for the Fisher methods (B). The background is represented in red and the signal in blue. Points and uncertainties represent the training samples, filled bins represent the test samples.

6.6 95% Confidence Level Limits

Expected limits at 95% confidence level (CL) can be derived in the absence of $t\bar{t}H(A)$ signal. With data, these upper limits on the number of signal events can be determined by fitting the discriminant variables obtained from the data events with those for the hypothesis of signal plus background [54]. For that purpose, a test-statistic, which characterizes the data (background and signal), was done

$$X_d = \sum_i n_i \log\left(1 + \frac{s_i}{b_i}\right) \tag{6.24}$$

where i runs over all the bins of the discriminant variable and n_i , s_i and b_i are the number of events in bin i of the discriminant variable in the data, the expected background and the signal events, respectively. When data events are more similar to the signal events, the X_d variable takes higher values.

The X_d statistical test is then compared with similar statistical tests obtained for the hypotheses of signal plus background (X_{s+b}) and background only (X_b). For the signal plus background hypothesis, the X_{s+b} distribution was computed iteratively, by simulating statistically compatible distributions with the sum of the signal and the background discriminant variables. The statistical fluctuations were performed with Poisson distributions and in each iteration X_{s+b} was computed as

$$X_{s+b} = \sum_i n_i^{(s+b)} \log\left(1 + \frac{s_i}{b_i}\right) \tag{6.25}$$

where, $n_i^{(s+b)}$ is the total number of events in the simulated distribution. A similar method was used to obtain the X_b statistical test

$$X_b = \sum_i n_i^{(b)} \log\left(1 + \frac{s_i}{b_i}\right) \tag{6.26}$$

in which $n_i^{(b)}$ is the total number of events in the simulated distributions of the background discriminant variables.

In the modified frequentist likelihood method, the confidence level (CL) of the extracted limit is defined as

$$1 - CL = \frac{\int_0^{X_d} P_{s+b}(X)dX}{\int_0^{X_d} P_b(X)dX} \tag{6.27}$$

where P_{s+b} and P_b are the X_{s+b} and X_b distributions, respectively. The 95% CL observed limit is the value for which expression (6.27) is equal to 0.05.

Let us compute the 95% confidence limits for $\sigma_{t\bar{t}h} \times \text{BR}(h \to b\bar{b})$ in the background only scenario, using this best multivariate distribution. Figure 6.12 shows the values for different luminosities.

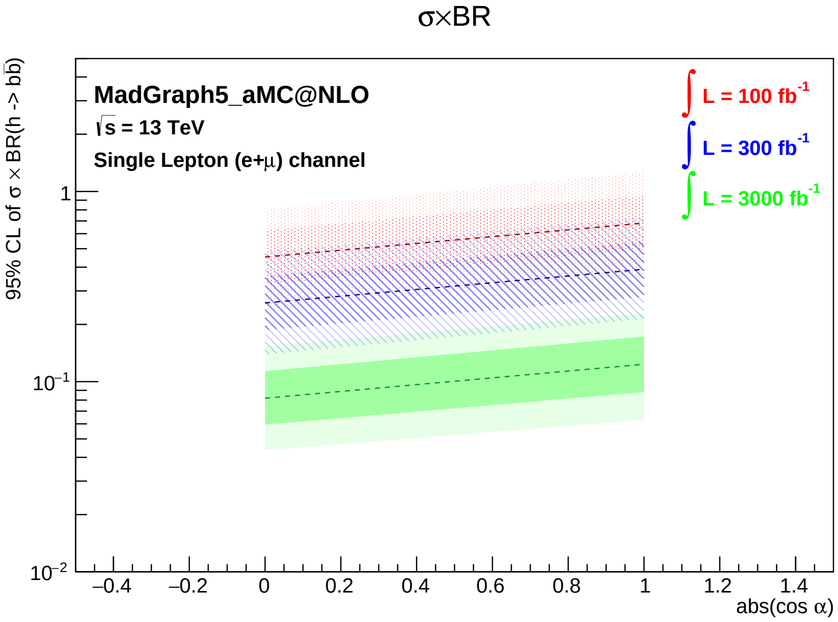

FIGURE 6.12: The 95% confidence limit values for $\sigma_{t\bar{t}H} \times \text{BR}(h \to b\bar{b})$ on the background only scenario. The different colours correspond to different integrated luminosities. Dashed lines refer to medians, narrower (wider) bands to the $1\sigma(2\sigma)$ intervals.

Conclusions

In this thesis I have proposed to exploit angular momentum conservation in order to obtain CP sensitive variables of the Higgs coupling to the top quarks. To do so, a kinematic fit was developed using `MadAnalysis5` and `KLFitter`. Finally, a limit at the 95% confidence level was computed.

It is concluded that a non-truth match reconstruction based on the Maximum Likelihood Estimate using `KLFitter` is very efficient for $t\bar{t}H$ single lepton final state events (see Table 5.8). This is partly because of the chosen final topology itself, since the algorithm takes tremendous advantages from b-tagging to reduce combinatorial background by means of the transfer functions. Furthermore, the efficiencies obtained in this work are slightly improved with regards to the results presented by *Erdmann, Johannes and Guindon, Stefan and Kroeninger* [34] for top-quark pairs reconstruction with the same method. This can be explained by the use of multiple transfer functions.

Secondly, it seems possible to probe the CP nature of the Higgs coupling to top quarks at ATLAS through the new variables studied here. The helicity formalism provides tools to compute these variables by using conservation of angular momentum. These variables showed to be very promising and if the existence of a non-pure scalar Higgs is to be true, it could provide valuable clues for the matter/antimatter asymmetry problem, among others.

Finally, this thesis was able to verify the sensitivity at ATLAS for two extremes hypotheses, namely for the pure scalar- and pure pseudo-scalar Higgs doublets and to compute the 95% confidence limits on their cross sections on the absence of signal.

A natural follow up for this work would be to provide further simulation for the whole range of the coupling parameters, i.e. to study the same CP sensitive variables for the full range of mixed CP even/odd Higgs couplings. Upon this, a detailed analysis of actual ATLAS data should follow. This would enable the comparison between simulated and detected data, hopefully converging on one of the studied possibilities.

Bibliography

[1] G. Aad et al. "The ATLAS Experiment at the CERN Large Hadron Collider". In: *JINST* 3 (2008), S08003. DOI: `10.1088/1748-0221/3/08/S08003`.

[2] G. Aad et al. "The ATLAS Inner Detector commissioning and calibration". In: *Eur. Phys. J.* C70 (2010), pp. 787–821. DOI: `10.1140/epjc/s10052-010-1366-7`. arXiv: `1004.5293 [physics.ins-det]`.

[3] Georges Aad et al. "Measurements of the Higgs boson production and decay rates and coupling strengths using pp collision data at $\sqrt{s} = 7$ and 8 TeV in the ATLAS experiment". In: *Eur. Phys. J.* C76.1 (2016), p. 6. DOI: `10.1140/epjc/s10052-015-3769-y`. arXiv: `1507.04548 [hep-ex]`.

[4] Georges Aad et al. "Observation of a new particle in the search for the Standard Model Higgs boson with the ATLAS detector at the LHC". In: *Phys. Lett.* B716 (2012), pp. 1–29. DOI: `10.1016/j.physletb.2012.08.020`. arXiv: `1207.7214 [hep-ex]`.

[5] Georges Aad et al. "Operation and performance of the ATLAS semiconductor tracker". In: *JINST* 9 (2014), P08009. DOI: `10.1088/1748-0221/9/08/P08009`. arXiv: `1404.7473 [hep-ex]`.

[6] K. Aamodt et al. "The ALICE experiment at the CERN LHC". In: *JINST* 3 (2008), S08002. DOI: `10.1088/1748-0221/3/08/S08002`.

[7] A. Augusto Alves Jr. et al. "The LHCb Detector at the LHC". In: *JINST* 3 (2008), S08005. DOI: `10.1088/1748-0221/3/08/S08005`.

[8] J. Alwall et al. "The automated computation of tree-level and next-to-leading order differential cross sections, and their matching to parton shower simulations". In: *JHEP* 07 (2014), p. 079. DOI: `10.1007/JHEP07(2014)079`. arXiv: `1405.0301 [hep-ph]`.

[9] Johan Alwall et al. "Comparative study of various algorithms for the merging of parton showers and matrix elements in hadronic collisions". In: *Eur. Phys. J.* C53 (2008), pp. 473–500. DOI: `10.1140/epjc/s10052-007-0490-5`. arXiv: `0706.2569 [hep-ph]`.

[10] Johan Alwall et al. "MadGraph 5 : Going Beyond". In: *JHEP* 06 (2011), p. 128. DOI: `10.1007/JHEP06(2011)128`. arXiv: `1106.0522 [hep-ph]`.

[11] T. W. Anderson. "R. A. Fisher and multivariate analysis". In: *Statist. Sci.* 11.1 (Jan. 1996), pp. 20–34. DOI: `10.1214/ss/1032209662`. URL: `http://dx.doi.org/10.1214/ss/1032209662`.

[12] G. Anelli et al. "The TOTEM experiment at the CERN Large Hadron Collider". In: *JINST* 3 (2008), S08007. DOI: `10.1088/1748-0221/3/08/S08007`.

[13] P. Artoisenet et al. "A framework for Higgs characterisation". In: *JHEP* 11 (2013), p. 043. DOI: `10.1007/JHEP11(2013)043`. arXiv: `1306.6464 [hep-ph]`.

[14] ATLAS. *Analysis regions for the single-lepton channel, background ratios.* 2016. URL: `https://atlas.web.cern.ch/Atlas/GROUPS/PHYSICS/CONFNOTES/ATLAS-CONF-2016-080/fig_03b.eps`.

[15] ATLAS. *Analysis regions for the single-lepton channel, ratio signal/background.* 2016. URL: `https://atlas.web.cern.ch/Atlas/GROUPS/PHYSICS/CONFNOTES/ATLAS-CONF-2016-080/fig_03a.eps`.

[16] Combined Top Data [ATLAS]. *Summary of LHC and Tevatron measurements of the top-pair production cross-section as a function of the centre-of-mass energy compared to the NNLO QCD calculation complemented with NNLL resummation (top++2.0).* 2016. URL: `https://atlas.web.cern.ch/Atlas/GROUPS/PHYSICS/CombinedSummaryPlots/TOP/tt_xsec_vsroots/tt_xsec_vsroots.pdf`.

[17] Richard D. Ball et al. "Parton distributions with LHC data". In: *Nucl. Phys.* B867 (2013), pp. 244–289. DOI: `10.1016/j.nuclphysb.2012.10.003`. arXiv: `1207.1303 [hep-ph]`.

[18] W. Bernreuther et al. "Top quark pair production and decay at hadron colliders". In: *Nucl. Phys.* B690 (2004), pp. 81–137. DOI: `10.1016/j.nuclphysb.2004.04.019`. arXiv: `hep-ph/0403035 [hep-ph]`.

[19] Mathias Brucherseifer, Fabrizio Caola, and Kirill Melnikov. "On the NNLO QCD corrections to single-top production at the LHC". In: *Phys. Lett.* B736 (2014), pp. 58–63. DOI: `10.1016/j.physletb.2014.06.075`. arXiv: `1404.7116 [hep-ph]`.

[20] Matteo Cacciari, Gavin P. Salam, and Gregory Soyez. "FastJet User Manual". In: *Eur. Phys. J.* C72 (2012), p. 1896. DOI: `10.1140/epjc/s10052-012-1896-2`. arXiv: `1111.6097 [hep-ph]`.

[21] Matteo Cacciari, Gavin P. Salam, and Gregory Soyez. "The Anti-k(t) jet clustering algorithm". In: *JHEP* 04 (2008), p. 063. DOI: `10.1088/1126-6708/2008/04/063`. arXiv: `0802.1189 [hep-ph]`.

[22] A. Caldwell, D. Kollár, and K. Kröninger. "BAT - The Bayesian analysis toolkit". In: *Computer Physics Communications* 180 (Nov. 2009), pp. 2197–2209. DOI: `10.1016/j.cpc.2009.06.026`. arXiv: `0808.2552 [physics.data-an]`.

[23] B. C. Canas et al. "The weak mixing angle from low energy neutrino measurements: a global update". In: *Phys. Lett.* B761 (2016), pp. 450–455. DOI: `10.1016/j.physletb.2016.08.047`. arXiv: `1608.02671 [hep-ph]`.

[24] Marcela Carena et al. "Electroweak baryogenesis and new TeV fermions". In: *Nucl. Phys.* B716 (2005), pp. 319–351. DOI: `10.1016/j.nuclphysb.2005.03.025`. arXiv: `hep-ph/0410352 [hep-ph]`.

[25] S. Chatrchyan et al. "The CMS experiment at the CERN LHC". In: *JINST* 3 (2008), S08004. DOI: `10.1088/1748-0221/3/08/S08004`.

[26] Serguei Chatrchyan et al. "Observation of a new boson at a mass of 125 GeV with the CMS experiment at the LHC". In: *Phys. Lett.* B716 (2012), pp. 30–61. DOI: `10.1016/j.physletb.2012.08.021`. arXiv: `1207.7235 [hep-ex]`.

[27] Serguei Chatrchyan et al. "Observation of the associated production of a single top quark and a W boson in pp collisions at $\sqrt{s}$ =8 TeV". In: *Phys. Rev. Lett.* 112.23 (2014), p. 231802. DOI: `10.1103/PhysRevLett.112.231802`. arXiv: `1401.2942 [hep-ex]`.

[28] The ATLAS collaboration. "Search for the Standard Model Higgs boson produced in association with top quarks and decaying into $b\bar{b}$ in pp collisions at $\sqrt{s}$ = 13 TeV with the ATLAS detector". In: (2016).

[29] Eric Conte, Benjamin Fuks, and Guillaume Serret. "MadAnalysis 5, A User-Friendly Framework for Collider Phenomenology". In: *Comput. Phys. Commun.* 184 (2013), pp. 222–256. DOI: `10.1016/j.cpc.2012.09.009`. arXiv: `1206.1599 [hep-ph]`.

[30] Micha Czakon, Paul Fiedler, and Alexander Mitov. "Total Top-Quark Pair-Production Cross Section at Hadron Colliders Through $O(\frac{4}{S})$". In: *Phys. Rev. Lett.* 110 (2013), p. 252004. DOI: `10.1103/PhysRevLett.110.252004`. arXiv: `1303.6254 [hep-ph]`.

[31] D. Dannheim and for the ATLAS Liquid Argon Calorimeter Group. "Commissioning and Performance of the ATLAS Liquid Argon Calorimeters". In: *ArXiv e-prints* (Sept. 2008). arXiv: `0809.2672 [physics.ins-det]`.

[32] A. Denner et al. "Standard Model Higgs-Boson Branching Ratios with Uncertainties". In: *Eur. Phys. J.* C71 (2011), p. 1753. DOI: `10.1140/epjc/s10052-011-1753-8`. arXiv: `1107.5909 [hep-ph]`.

[33] Joshua Ellis. "TikZ-Feynman: Feynman diagrams with TikZ". In: *Comput. Phys. Commun.* 210 (2017), pp. 103–123. DOI: `10.1016/j.cpc.2016.08.019`. arXiv: `1601.05437 [hep-ph]`.

[34] Johannes Erdmann et al. "A likelihood-based reconstruction algorithm for top-quark pairs and the KLFitter framework". In: *Nucl. Instrum. Meth.* A748 (2014), pp. 18–25. DOI: `10.1016/j.nima.2014.02.029`. arXiv: `1312.5595 [hep-ex]`.

[35] J. de Favereau et al. "DELPHES 3, A modular framework for fast simulation of a generic collider experiment". In: *JHEP* 02 (2014), p. 057. DOI: `10.1007/JHEP02(2014)057`. arXiv: `1307.6346 [hep-ex]`.

[36] Andrew Gelman. *Bayesian data analysis*. Boca Raton, Fla: Chapman & Hall/CRC, 2004. ISBN: 978-1584883883.

[37] David Griffiths. *Introduction to electrodynamics*. Singapore: Prentice Hall, 1999. ISBN: 9789814024440.

[38] John F. Gunion and Xiao-Gang He. "Determining the CP Nature of a Neutral Higgs Boson at the CERN Large Hadron Collider". In: *Phys. Rev. Lett.* 76 (24 1996), pp. 4468–4471. DOI: `10.1103/PhysRevLett.76.4468`. URL: `http://link.aps.org/doi/10.1103/PhysRevLett.76.4468`.

[39] A. Hoecker et al. "TMVA - Toolkit for Multivariate Data Analysis". In: *ArXiv Physics e-prints* (Mar. 2007). eprint: `physics/0703039`.

[40] F. Hugging. "The ATLAS Pixel Detector". In: *IEEE Transactions on Nuclear Science* 53 (June 2006), pp. 1732–1736. DOI: `10.1109/TNS.2006.871506`. eprint: `physics/0412138`.

[41] N. V. Krasnikov and V. A. Matveev. "Physics at LHC". In: *Phys. Part. Nucl.* 28 (1997). [Fiz. Elem. Chast. Atom. Yadra28,1125(1997)], pp. 441–470. DOI: `10.1134/1.953049`. arXiv: `hep-ph/9703204 [hep-ph]`.

[42] Combined Higgs Data [LHC]. *Higgs-boson production cross sections (theoretical) as a function of centre-of-mass energies*. 2014. URL: `https://twiki.cern.ch/twiki/pub/LHCPhysics/HiggsEuropeanStrategy2012/Higgs_XS_7-100TeV_HH.eps`.

[43] Gregory Mahlon and Stephen J. Parke. "Spin Correlation Effects in Top Quark Pair Production at the LHC". In: *Phys. Rev.* D81 (2010), p. 074024. DOI: `10.1103/PhysRevD.81.074024`. arXiv: `1001.3422 [hep-ph]`.

[44] F Mandl. *Quantum field theory*. Hoboken, N.J: Wiley, 2010. ISBN: 978-0-471-49683-0.

[45] R. B. Millar. *Maximum likelihood estimation and inference : with examples in R, SAS and ADMB*. Chichester, West Sussex, United Kingdom: John Wiley & Sons, Ltd, 2011. ISBN: 978-0470094822.

[46] Vasiliki A. Mitsou. "The ATLAS transition radiation tracker". In: *Astroparticle, particle and space physics, detectors and medical physics applications. Proceedings, 8th Conference, ICATPP 2003, Como, Italy, October 6-10, 2003*. 2003, pp. 497–501. DOI: `10.1142/9789812702708_0073`. arXiv: `hep-ex/0311058 [hep-ex]`. URL: `http://weblib.cern.ch/abstract?ATL-CONF-2003-012`.

[47] M. Mohammadi Najafabadi. "Single Top production at LHC". In: *Proceedings, 41st Rencontres de Moriond, 2006 QCD and High Energy Hadronic Interactions: La Thuile, Val d'Aoste, Italy, Mar 18-25, 2006*. 2006, pp. 173–178. arXiv: `hep-ex/0605034 [hep-ex]`. URL: `https://inspirehep.net/record/716809/files/arXiv:hep-ex_0605034.pdf`.

[48] Regina Moles-Valls. "Alignment of the {ATLAS} inner detector tracking system". In: *Nuclear Instruments and Methods in Physics Research Section A: Accelerators, Spectrometers, Detectors and Associated Equipment* 617.13 (2010). 11th Pisa Meeting on Advanced DetectorsProceedings of the 11th Pisa Meeting on Advanced Detectors, pp. 568 –570. ISSN: 0168-9002. DOI: `http://dx.doi.org/10.1016/j.nima.2009.09.101`. URL: `http://www.sciencedirect.com/science/article/pii/S016890020901883X`.

[49] S. F. Novaes. "Standard model: An Introduction". In: *Particles and fields. Proceedings, 10th Jorge Andre Swieca Summer School, Sao Paulo, Brazil, February 6-12, 1999*. 1999, pp. 5–102. arXiv: `hep-ph/0001283 [hep-ph]`. URL: `http://alice.cern.ch/format/showfull?sysnb=2173689`.

[50] C. Patrignani et al. "Review of Particle Physics". In: *Chin. Phys.* C40.10 (2016), p. 100001. DOI: `10.1088/1674-1137/40/10/100001`.

[51] Antonio Pich. "The Standard model of electroweak interactions". In: *High-energy physics. Proceedings, European School, Aronsborg, Sweden, June 18-July 1, 2006*. [,1(2007)]. 2007, pp. 1–49. arXiv: `0705.4264 [hep-ph]`. URL: `http://doc.cern.ch/yellowrep/2007/2007-005/cern-2007-005.pdf`.

[52] James Pinfold et al. "Technical Design Report of the MoEDAL Experiment". In: (2009).

[53] Chris Quigg. *Gauge theories of the strong, weak, and electromagnetic interactions*. Reading, Mass: Addison-Wesley, 1997. ISBN: 978-0201328325.

[54] A L Read. "Modified frequentist analysis of search results (the CL_s method)". In: CERN-OPEN-2000-205 (2000). URL: `https://cds.cern.ch/record/451614`.

[55] Jeffrey D. Richman. "An Experimenter's Guide to the Helicity Formalism". In: (1984).

[56] Timo van Ritbergen and Robin G. Stuart. "On the precise determination of the Fermi coupling constant from the muon lifetime". In: *Nucl. Phys.* B564 (2000), pp. 343–390. DOI: `10.1016/S0550-3213(99)00572-6`. arXiv: `hep-ph/9904240 [hep-ph]`.

[57] Torbjorn Sjostrand, Stephen Mrenna, and Peter Z. Skands. "PYTHIA 6.4 Physics and Manual". In: *JHEP* 05 (2006), p. 026. DOI: `10.1088/1126-6708/2006/05/026`. arXiv: `hep-ph/0603175 [hep-ph]`.

[58] R. G. Suarez. *Single top production mechanism, respective theoretical predictions and CMS experimental values.* 2014. URL: `https://github.com/rebecacern/singleTopPlot/blob/master/plots/singletopDec6.pdf`.

[59] A. Tricomi. "The LHCf experiment at LHC". In: *Nuovo Cim.* 33 (2010), pp. 21–25. DOI: `10.1393/ncc/i2011-10749-5`.

[60] P. Védrine. "Large Superconducting Magnet Systems". In: *Proceedings, CAS - CERN Accelerator School : Course on Superconductivity for Accelerators (CAS 2013): Erice, Italy, April 24-May 4, 2013*. 2014, pp. 559–583. DOI: `10.5170/CERN-2014-005.559`. arXiv: `1501.07169 [physics.acc-ph]`. URL: `http://inspirehep.net/record/1341663/files/arXiv:1501.07169.pdf`.

[61] Wikipedia. *ATLAS Experiment with labels*. 2012. URL: `https://upload.wikimedia.org/wikipedia/commons/9/9c/ATLAS_Drawing_with_Labels.svg`.

[62] Graham Williams. *Data mining with Rattle and R : the art of excavating data for knowledge discovery*. New York: Springer, 2011. ISBN: 978-1-4419-9890-3.

Appendix A

Transfer Functions

A.1 Light Jets

The full list of Transfer Functions and their best fitting values for the Light Jets is presented. The distributions have the following regime indexing table

η	**0 - 0.5**	**0.5 - 1**	**1 - 1.5**	**1.5 - 2**	**2 - 2.5**	**2.5 - 3**	**3 - 3.5**	**3.5 - 4**	**4 - 4.5**
20 $\geq$ E $<$ 120	0	1	2	3	4	5	6	7	8
120 $\geq$ E $<$ 220	9	10	11	12	13	14	15	16	17
220 $\geq$ E $<$ 320	18	19	20	21	22	23	24	25	26
320 $\geq$ E $<$ 420	27	28	29	30	31	32	33	34	35
420 $\geq$ E $<$ 520	36	37	38	39	40	41	42	43	44
520 $\geq$ E $<$ 620	45	46	47	48	49	50	51	52	53
620 $\geq$ E $<$ 720	54	55	56	57	58	59	60	61	62

TABLE A.1: Regime indexing for the Light Jets transfer functions. In green it's regimes with at least 1000 events, in red it's regimes with less than 1000 events.

The colouring scheme in table A.1 shows the regimes in which at least 1000 events can be found, in green, and where it can not, in red. A regime is just considered if it meets the criteria of having at least 1000 events, in that case it is considered statistically relevant.

Since it's required the transfer functions to be normalized through

$$C_1 + C_2 = 1 \tag{A.1}$$

It's only necessary five parameters to fully parametrize them: μ_1, μ_2, σ_1, σ_2, ζ. Namely, the mean and standard deviation of the first gaussian, mean and standard deviation of the second gaussian and the ratio between the norms of the two, respectively.

$$\zeta = \frac{C_2}{C_1} \tag{A.2}$$

The full list of parameters is found in table A.2.

Index	μ_1	μ_2	σ_1	σ_2	ζ	χ^2
0	-0.621329	-0.164365	2.75628	0.918157	0.627688	4705.42
1	-0.804869	-0.130092	2.95218	0.938065	0.619796	3677.94
2	-1.16922	-0.0658149	3.23256	0.995849	0.606693	2111.01
3	-1.64045	0.000887835	3.65824	1.09882	0.611609	878.747
4	-2.13927	0.0671648	3.83462	1.23385	0.599935	173.319
9	0.172627	0.853048	1.51767	0.0128946	0.205263	2355.25
10	1	0.00980519	3.85093	1.0005	0.648871	2678.3
11	0.198525	-0.00839367	4.0488	1.01901	0.643357	2452.49
12	-0.780023	0.0188437	3.94597	1.09835	0.599645	1690.73
13	-1	0.0469356	4.04025	1.17783	0.557826	1443.11
14	-2.07327	0.157584	4.12662	1.27875	0.508966	250.252
18	3.28219	0.231425	4.03626	1.1314	0.466242	626.156
19	3.0101	0.222642	4.54173	1.18396	0.578266	783.204
20	1.89286	0.112073	4.88756	1.14782	0.629471	1143.07
21	0.548073	0.0212417	5.03601	1.21993	0.644014	1106.52
22	-1	-0.0223004	4.82525	1.27828	0.595108	778.235
23	-2	0.0323353	4.52291	1.3571	0.513523	399.504
24	-2.14876	0.0945757	5.12212	1.4448	0.501766	65.3984
27	5.00177	0.965145	4.78919	1.81429	0.538422	200.076
28	4.38107	0.605128	5.06271	1.46884	0.468958	300.673
29	3.15913	0.286832	5.39722	1.32665	0.579985	538.946
30	1.66395	0.112969	5.56897	1.36494	0.651322	669.071
31	-0.595365	-0.0441515	5	1.32842	0.582129	498.845
32	-2	-0.106883	5.27618	1.42252	0.576362	334.448
33	-2.39096	1.33705e-09	4.78951	1.54364	0.457076	141.404
37	5.19626	1	5.41285	1.82643	0.49639	122.334
38	4.52411	0.40518	5.75484	1.26466	0.457294	244.103
39	2.71936	0.185444	6.21978	1.5249	0.63039	323.69
40	0.0938809	-0.0521869	5.21142	1.42748	0.60824	431.906
41	-1.75332	-0.192641	5	1.4919	0.55169	250.47
42	-2	-0.243189	4.58508	1.51712	0.432123	141.774
47	5.46344	0.773122	5.80287	1.88653	0.446619	159.326
48	3.50379	0.364708	6.19869	1.56329	0.56384	206.148
49	0.992727	0.00758888	6.01965	1.57752	0.600613	215.063
50	-1.47042	-0.150251	5.04868	1.41449	0.519585	166.435
51	-1	-0.465652	5	1.75092	0.609993	130.77
57	4.48987	0.536377	6.54106	1.73667	0.498776	133.332
58	2.39063	-0.0498562	7.03224	1.89903	0.678571	149.341
59	-0.876304	-0.182443	4.90801	1.3985	0.498921	159.045
60	-1	-0.474892	5	1.70367	0.482977	102.628

TABLE A.2: Parameter table for the b Jets and χ^2 test value of the fit (not normalized). The middle rules indicate indexing gaps due to regions where not sufficient statistics is found.

A.2 b Jets

The full list of Transfer Functions and their best fitting values for the b Jets is presented. The distributions have the following regime indexing table

η	**0 - 0.5**	**0.5 - 1**	**1 - 1.5**	**1.5 - 2**	**2 - 2.5**	**2.5 - 3**	**3 - 3.5**	**3.5 - 4**	**4 - 4.5**
$\mathbf{20 \geq E < 120}$	🟩 0	🟩 1	🟩 2	🟩 3	🟩 4	🟥 5	🟥 6	🟥 7	🟥 8
$\mathbf{120 \geq E < 220}$	🟩 9	🟩 10	🟩 11	🟩 12	🟩 13	🟩 14	🟥 15	🟥 16	🟥 17
$\mathbf{220 \geq E < 320}$	🟩 18	🟩 19	🟩 20	🟩 21	🟩 22	🟩 23	🟩 24	🟥 25	🟥 26
$\mathbf{320 \geq E < 420}$	🟩 27	🟩 28	🟩 29	🟩 30	🟩 31	🟩 32	🟩 33	🟥 34	🟥 35
$\mathbf{420 \geq E < 520}$	🟥 36	🟩 37	🟩 38	🟩 39	🟩 40	🟩 41	🟩 42	🟥 43	🟥 44
$\mathbf{520 \geq E < 620}$	🟥 45	🟥 46	🟩 47	🟩 48	🟩 49	🟩 50	🟩 51	🟥 52	🟥 53
$\mathbf{620 \geq E < 720}$	🟥 54	🟥 55	🟥 56	🟩 57	🟩 58	🟩 59	🟩 60	🟥 61	🟥 62

TABLE A.3: Regime indexing for the b Jets transfer functions. In green it's regimes with at least 1000 events, in red it's regimes with less than 1000 events.

The colouring scheme in table A.3 shows the regimes in which at least 1000 events can be found, in green, and where it can not, in red. A regime is just considered if it meets the criteria of having at least 1000 events, in that case it is considered statistically relevant.

Since it's required the transfer functions to be normalized through

$$C_1 + C_2 = 1 \tag{A.3}$$

It's only necessary five parameters to fully parametrize them: μ_1, μ_2, σ_1, σ_2, ζ. Namely, the mean and standard deviation of the first gaussian, mean and standard deviation of the second gaussian and the ratio between the norms of the two, respectively.

$$\zeta = \frac{C_2}{C_1} \tag{A.4}$$

The full list of parameters is found in table A.4.

Index	μ_1	μ_2	σ_1	σ_2	ζ	χ^2
0	-1.73202	-0.409803	2.57814	0.929645	0.479312	6495.13
1	-2.01745	-0.40366	2.76682	0.978793	0.478769	4824.03
2	-2.54	-0.386673	3.02139	1.03211	0.466295	2907.14
3	-3.34926	-0.408615	3.34458	1.15719	0.47029	1191.39
4	-3.32	-0.386958	3.47665	1.21596	0.417132	232.628
9	-0.252887	-0.0953843	3.20639	0.901293	0.570129	4670.29
10	-0.672368	-0.0853421	3.33451	0.909484	0.547301	5180.49
11	-1	-0.0639886	3.50883	0.916157	0.4897	5230.79
12	-2.19	-0.042873	3.70269	1.00993	0.460271	2555.54
13	-2.853	-0.101749	3.96439	1.14483	0.425562	1373.93
14	-3.487	-0.171625	4.02849	1.29386	0.377883	324.795
18	1.17453	0.0527359	3.78355	1.02658	0.561787	1234.04
19	0.45304	0.0240197	3.87941	0.964672	0.551321	1834.61
20	-0.43598	0.0253593	4.02678	0.955891	0.531182	2544.81
21	-1.49153	0.0692439	4.17299	1.01033	0.489919	1981.77
22	-2.65739	0.0223791	4.56403	1.19969	0.474234	1142.54
23	-3.14	0.0162638	4	1.2418	0.385859	769.21
24	-3.75	-0.331304	4.59266	1.49306	0.395671	122.245
27	2.81801	0.210867	4.39515	1.14576	0.45013	244.211
28	1	0.131908	3.81322	0.937318	0.454191	654.65
29	0.472641	0.097078	4.39811	0.990427	0.515526	1111.52
30	-0.863725	0.105657	4.33604	1.01995	0.492406	1368.32
31	-2.15535	0.0948812	4.82587	1.21426	0.483913	826.135
32	-2.8	0.0406665	4.59634	1.29132	0.401405	581.987
33	-3.5	-0.241742	4.62448	1.58905	0.380578	197.501
37	2.635	0.393184	4.80961	1.17243	0.428127	180.772
38	1.58	0.141113	4.84544	1.1267	0.52885	495.73
39	-0.579	0.166756	4.59564	1.09454	0.500939	761.157
40	-1.78316	0.0702802	4.97506	1.24465	0.500129	588.311
41	-2.9754	-0.081122	5	1.48164	0.462971	301.62
42	-3.169	-0.200287	5	1.613	0.407358	179.48
47	2.39681	0.279682	5	1.09144	0.429646	221.545
48	0.457648	0.182762	4.77378	1.21667	0.492581	408.67
49	-0.973561	-0.02	5.16325	1.25587	0.50144	396.611
50	-2.106	0.0741621	4.57036	1.23393	0.387582	307.388
51	-2.884	0.0815051	4.86768	1.42392	0.35608	124.635
57	1.37764	0.189977	5	1.31848	0.502143	225.423
58	-0.587314	0.091941	5	1.27354	0.489538	277.884
59	-1.98023	-0.114589	5	1.43899	0.448286	219.189
60	-2.63	0.0399036	5	1.42485	0.328405	105.781

TABLE A.4: Parameter table for the b Jets and χ^2 test value of the fit (not normalized). The middle rules indicate indexing gaps due to regions where not sufficient statistics is found.

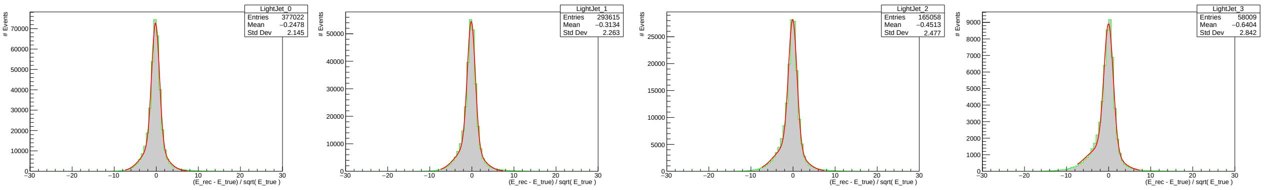

(A) L-Jets 0 (B) L-Jets 1 (C) L-Jets 2 (D) L-Jets 3

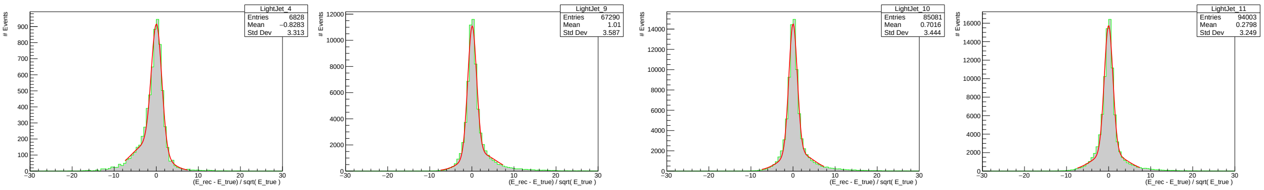

(E) L-Jets 4 (F) L-Jets 9 (G) L-Jets 10 (H) L-Jets 11

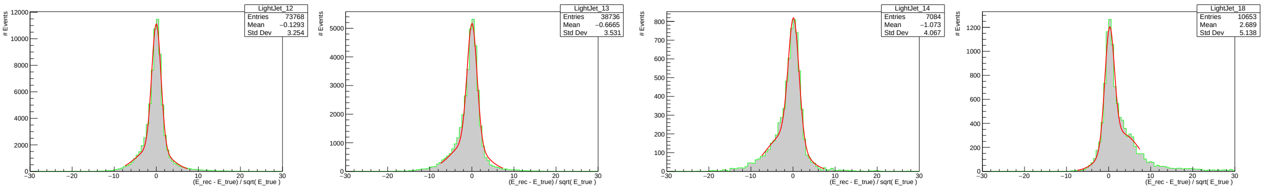

(I) L-Jets 12 (J) L-Jets 13 (K) L-Jets 14 (L) L-Jets 18

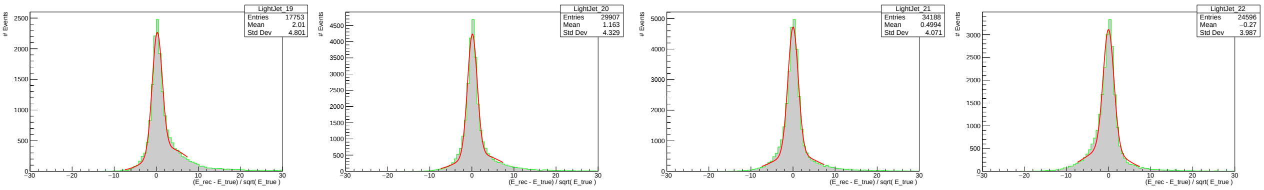

(M) L-Jets 19 (N) L-Jets 20 (O) L-Jets 21 (P) L-Jets 22

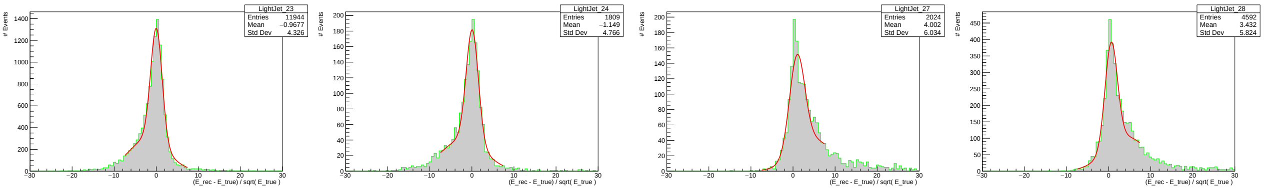

(Q) L-Jets 23 (R) L-Jets 24 (S) L-Jets 27 (T) L-Jets 28

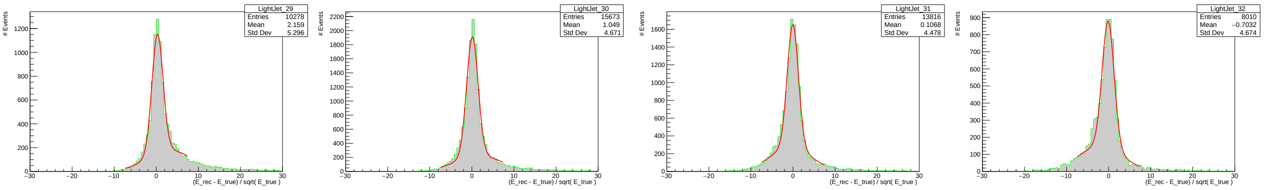

(U) L-Jets 29 (V) L-Jets 30 (W) L-Jets 31 (X) L-Jets 32

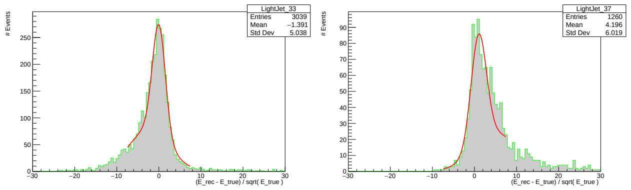

(Y) L-Jets 33 (Z) L-Jets 37

FIGURE A.1: Transfer functions for the Light Jets. In green the relative energy difference between reconstructed b Jet and parton level b-quark. In red the best double gaussian fit of the data. Part 1/2.

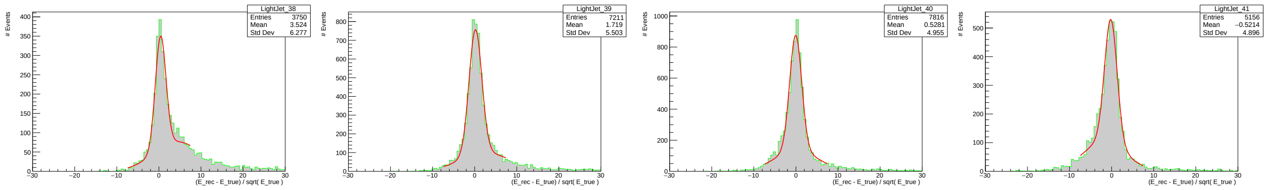

(A) L-Jets 38 (B) L-Jets 39 (C) L-Jets 40 (D) L-Jets 41

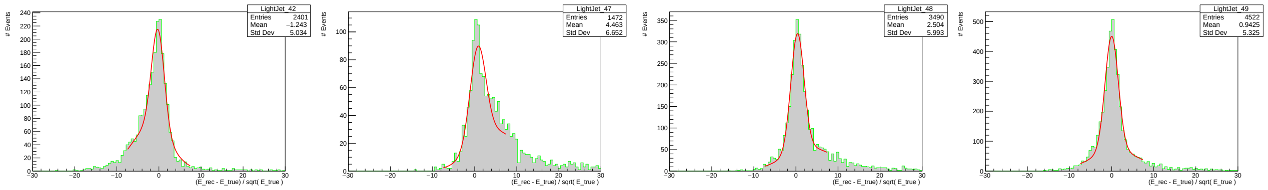

(E) L-Jets 42 (F) L-Jets 47 (G) L-Jets 48 (H) L-Jets 49

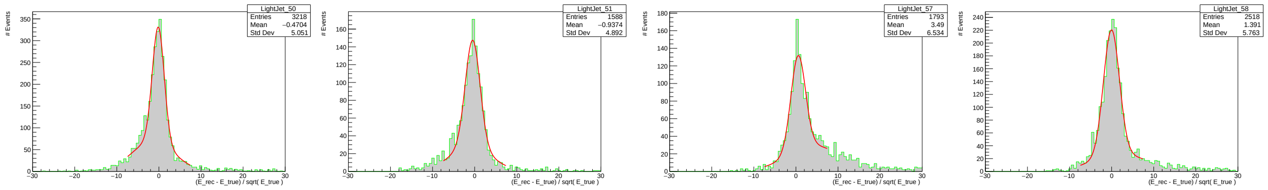

(I) L-Jets 50 (J) L-Jets 51 (K) L-Jets 57 (L) L-Jets 58

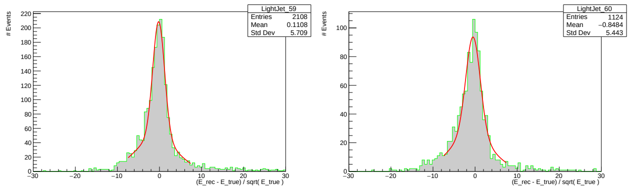

(M) L-Jets 59 (N) L-Jets 60

FIGURE A.2: Transfer functions for the Light Jets. In green the relative energy difference between reconstructed b Jet and parton level b-quark. In red the best double gaussian fit of the data. Part 2/2.

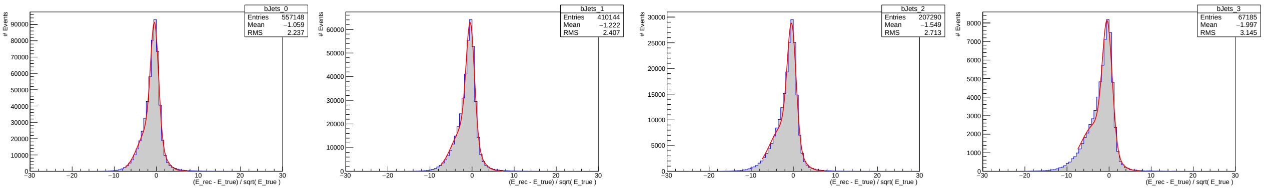

(A) b-Jets 0 (B) b-Jets 1 (C) b-Jets 2 (D) b-Jets 3

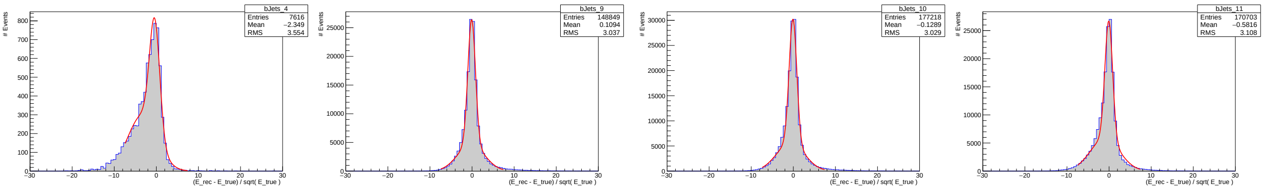

(E) b-Jets 4 (F) b-Jets 9 (G) b-Jets 10 (H) b-Jets 11

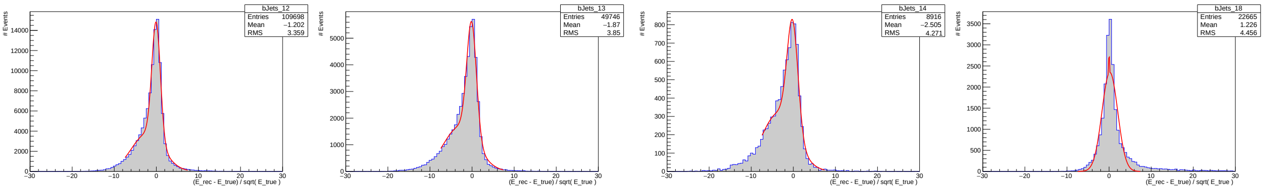

(I) b-Jets 12 (J) b-Jets 13 (K) b-Jets 14 (L) b-Jets 18

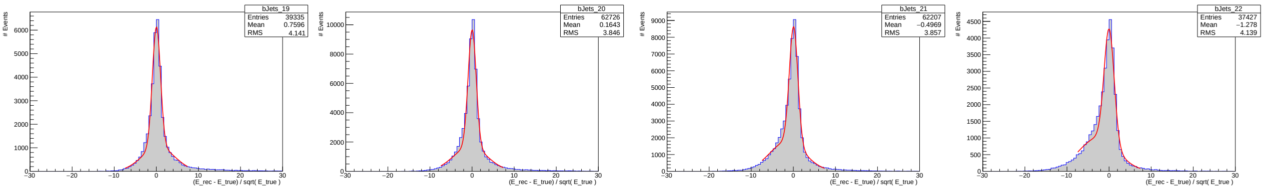

(M) b-Jets 19 (N) b-Jets 20 (O) b-Jets 21 (P) b-Jets 22

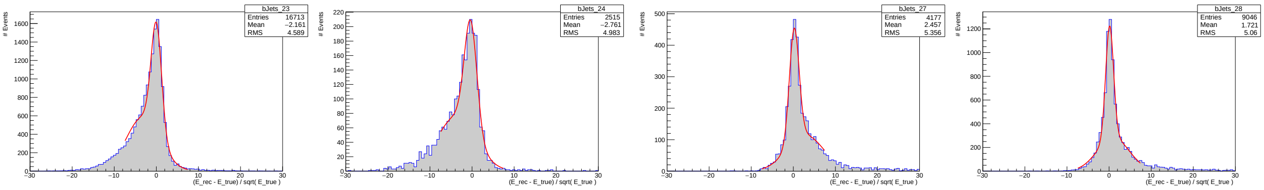

(Q) b-Jets 23 (R) b-Jets 24 (S) b-Jets 27 (T) b-Jets 28

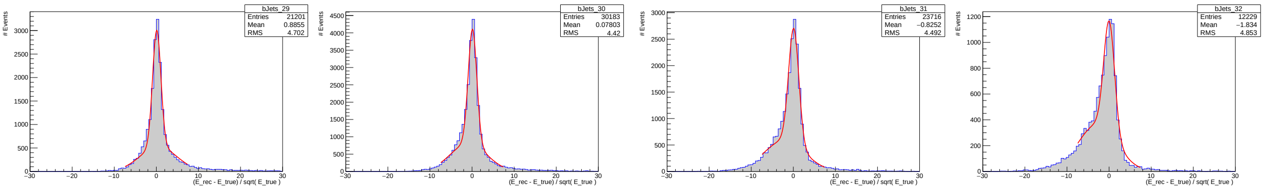

(U) b-Jets 29 (V) b-Jets 30 (W) b-Jets 31 (X) b-Jets 32

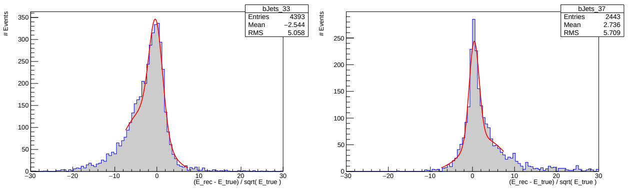

(Y) b-Jets 33 (Z) b-Jets 37

FIGURE A.3: Transfer functions for the bJets. In blue the relative energy difference between reconstructed b Jet and parton level b-quark. In red the best double gaussian fit of the data. Part 1/2.

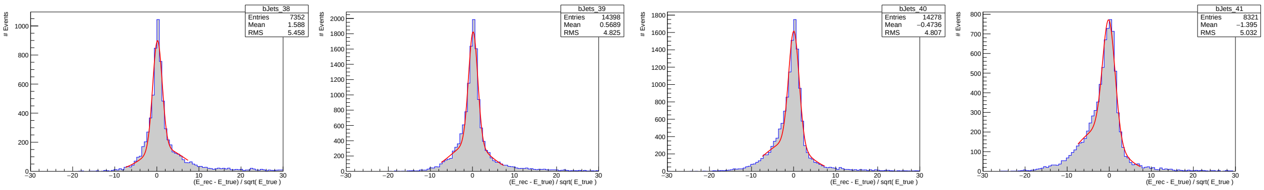

(A) b-Jets 38 (B) b-Jets 39 (C) b-Jets 40 (D) b-Jets 41

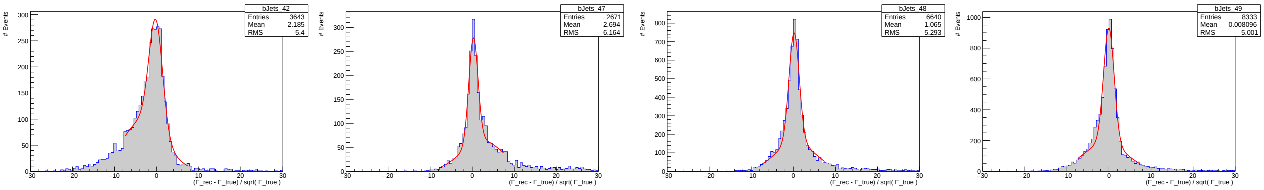

(E) b-Jets 42 (F) b-Jets 47 (G) b-Jets 48 (H) b-Jets 49

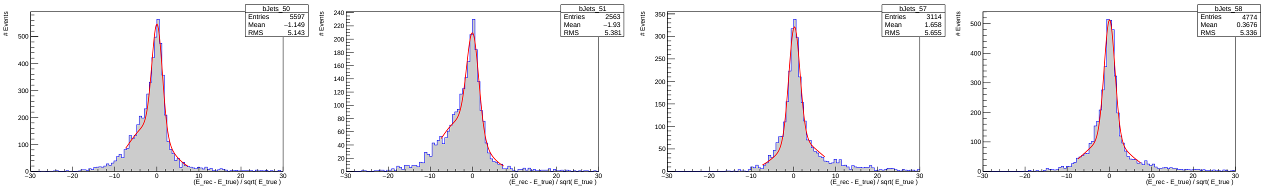

(I) b-Jets 50 (J) b-Jets 51 (K) b-Jets 57 (L) b-Jets 58

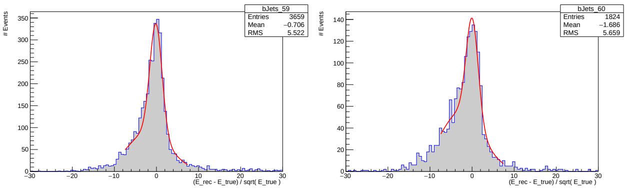

(M) b-Jets 59 (N) b-Jets 60

FIGURE A.4: Transfer functions for the bJets. In blue the relative energy difference between reconstructed b Jet and parton level b-quark. In red the best double gaussian fit of the data. Part 2/2.

Appendix B

DELPHES ATLAS Card

```
########################################
# Order of execution of  various modules
########################################

set  ExecutionPath {
ParticlePropagator

ChargedHadronTrackingEfficiency
ElectronTrackingEfficiency
MuonTrackingEfficiency

ChargedHadronMomentumSmearing
ElectronMomentumSmearing
MuonMomentumSmearing

TrackMerger
Calorimeter
EFlowMerger

PhotonEfficiency
PhotonIsolation

ElectronFilter
ElectronEfficiency
ElectronIsolation

MuonEfficiency
MuonIsolation

MissingET

NeutrinoFilter
GenJetFinder
FastJetFinder

JetEnergyScale

JetFlavorAssociation

BTagging
```

```
TauTagging

UniqueObjectFinder

ScalarHT

TreeWriter
}

#################################
# Propagate particles in cylinder
#################################

module ParticlePropagator ParticlePropagator {
set InputArray Delphes/stableParticles

set OutputArray stableParticles
set ChargedHadronOutputArray chargedHadrons
set ElectronOutputArray electrons
set MuonOutputArray muons

# radius of the magnetic field coverage, in m
set Radius 1.15
# half-length of the magnetic field coverage, in m
set HalfLength 3.51

# magnetic field
set Bz 2.0
}

####################################
# Charged hadron tracking efficiency
####################################

module Efficiency ChargedHadronTrackingEfficiency {
set InputArray ParticlePropagator/chargedHadrons
set OutputArray chargedHadrons

# add EfficiencyFormula {efficiency formula as a function of eta and pt}

# tracking efficiency formula for charged hadrons
set EfficiencyFormula {                                                  (pt <= 0.1)   *
    (0.00) +
(abs(eta) <= 1.5) * (pt > 0.1   && pt <= 1.0)   * (0.70) +
(abs(eta) <= 1.5) * (pt > 1.0)                  * (0.95) +
(abs(eta) > 1.5 && abs(eta) <= 2.5) * (pt > 0.1   && pt <= 1.0)   * (0.60) +
(abs(eta) > 1.5 && abs(eta) <= 2.5) * (pt > 1.0)                  * (0.85) +
(abs(eta) > 2.5)                                                  * (0.00)}
}

##############################
```

```
# Electron tracking efficiency
##############################

module Efficiency ElectronTrackingEfficiency {
set InputArray ParticlePropagator/electrons
set OutputArray electrons

# set EfficiencyFormula {efficiency formula as a function of eta and pt}

# tracking efficiency formula for electrons
set EfficiencyFormula {                                          (pt <= 0.1)    *
    (0.00) +
(abs(eta) <= 1.5) * (pt > 0.1    && pt <= 1.0)   * (0.73) +
(abs(eta) <= 1.5) * (pt > 1.0    && pt <= 1.0e2) * (0.95) +
(abs(eta) <= 1.5) * (pt > 1.0e2)                 * (0.99) +
(abs(eta) > 1.5 && abs(eta) <= 2.5) * (pt > 0.1    && pt <= 1.0)   * (0.50) +
(abs(eta) > 1.5 && abs(eta) <= 2.5) * (pt > 1.0    && pt <= 1.0e2) * (0.83) +
(abs(eta) > 1.5 && abs(eta) <= 2.5) * (pt > 1.0e2)                 * (0.90) +
(abs(eta) > 2.5)                                                   * (0.00) }
}

##########################
# Muon tracking efficiency
##########################

module Efficiency MuonTrackingEfficiency {
set InputArray ParticlePropagator/muons
set OutputArray muons

# set EfficiencyFormula {efficiency formula as a function of eta and pt}

# tracking efficiency formula for muons
set EfficiencyFormula {                                          (pt <= 0.1)    *
    (0.00) +
(abs(eta) <= 1.5) * (pt > 0.1    && pt <= 1.0)   * (0.75) +
(abs(eta) <= 1.5) * (pt > 1.0)                   * (0.99) +
(abs(eta) > 1.5 && abs(eta) <= 2.5) * (pt > 0.1    && pt <= 1.0)   * (0.70) +
(abs(eta) > 1.5 && abs(eta) <= 2.5) * (pt > 1.0)                   * (0.98) +
(abs(eta) > 2.5)                                                   * (0.00) }
}

########################################
# Momentum resolution for charged tracks
########################################

module MomentumSmearing ChargedHadronMomentumSmearing {
set InputArray ChargedHadronTrackingEfficiency/chargedHadrons
set OutputArray chargedHadrons

# set ResolutionFormula {resolution formula as a function of eta and pt}
```

```
# resolution formula for charged hadrons
set ResolutionFormula {                    (abs(eta) <= 0.5) ∗ (pt > 0.1) ∗ sqrt(0.06^2 + pt^2∗1.3
    e−3^2) +
(abs(eta) > 0.5 && abs(eta) <= 1.5) ∗ (pt > 0.1) ∗ sqrt(0.10^2 + pt^2∗1.7e−3^2) +
(abs(eta) > 1.5 && abs(eta) <= 2.5) ∗ (pt > 0.1) ∗ sqrt(0.25^2 + pt^2∗3.1e−3^2)}
}

###################################
# Momentum resolution for electrons
###################################

module MomentumSmearing ElectronMomentumSmearing {
set InputArray ElectronTrackingEfficiency/electrons
set OutputArray electrons

# set ResolutionFormula {resolution formula as a function of eta and energy}

# resolution formula for electrons
set ResolutionFormula {                    (abs(eta) <= 0.5) ∗ (pt > 0.1) ∗ sqrt(0.06^2 + pt^2∗1.3
    e−3^2) +
(abs(eta) > 0.5 && abs(eta) <= 1.5) ∗ (pt > 0.1) ∗ sqrt(0.10^2 + pt^2∗1.7e−3^2) +
(abs(eta) > 1.5 && abs(eta) <= 2.5) ∗ (pt > 0.1) ∗ sqrt(0.25^2 + pt^2∗3.1e−3^2)}
}

###############################
# Momentum resolution for muons
###############################

module MomentumSmearing MuonMomentumSmearing {
set InputArray MuonTrackingEfficiency/muons
set OutputArray muons

# set ResolutionFormula {resolution formula as a function of eta and pt}

# resolution formula for muons
set ResolutionFormula {                    (abs(eta) <= 0.5) ∗ (pt > 0.1) ∗ sqrt(0.02^2 + pt^2∗2.0
    e−4^2) +
(abs(eta) > 0.5 && abs(eta) <= 1.5) ∗ (pt > 0.1) ∗ sqrt(0.03^2 + pt^2∗3.0e−4^2) +
(abs(eta) > 1.5 && abs(eta) <= 2.5) ∗ (pt > 0.1) ∗ sqrt(0.06^2 + pt^2∗6.0e−4^2)}
}

##############
# Track merger
##############

module Merger TrackMerger {
# add InputArray InputArray
add InputArray ChargedHadronMomentumSmearing/chargedHadrons
add InputArray ElectronMomentumSmearing/electrons
add InputArray MuonMomentumSmearing/muons
set OutputArray tracks
```

```
}

#############
# Calorimeter
#############

module Calorimeter Calorimeter {
set ParticleInputArray ParticlePropagator/stableParticles
set TrackInputArray TrackMerger/tracks

set TowerOutputArray towers
set PhotonOutputArray photons

set EFlowTrackOutputArray eflowTracks
set EFlowPhotonOutputArray eflowPhotons
set EFlowNeutralHadronOutputArray eflowNeutralHadrons

set ECalEnergyMin 0.5
set HCalEnergyMin 1.0

set ECalEnergySignificanceMin 1.0
set HCalEnergySignificanceMin 1.0

set SmearTowerCenter true

set pi [expr {acos(−1)}]

# lists of the edges of each tower in eta and phi
# each list starts with the lower edge of the first tower
# the list ends with the higher edged of the last tower

# 10 degrees towers
set PhiBins {}
for {set i −18} {$i <= 18} {incr i} {
add PhiBins [expr {$i ∗ $pi/18.0}]
}
foreach eta {−3.2 −2.5 −2.4 −2.3 −2.2 −2.1 −2 −1.9 −1.8 −1.7 −1.6 −1.5 −1.4 −1.3 −1.2 −1.1 −1
    −0.9 −0.8 −0.7 −0.6 −0.5 −0.4 −0.3 −0.2 −0.1 0 0.1 0.2 0.3 0.4 0.5 0.6 0.7 0.8 0.9 1 1.1 1.2
    1.3 1.4 1.5 1.6 1.7 1.8 1.9 2 2.1 2.2 2.3 2.4 2.5 2.6 3.3} {
add EtaPhiBins $eta $PhiBins
}

# 20 degrees towers
set PhiBins {}
for {set i −9} {$i <= 9} {incr i} {
add PhiBins [expr {$i ∗ $pi/9.0}]
}
foreach eta {−4.9 −4.7 −4.5 −4.3 −4.1 −3.9 −3.7 −3.5 −3.3 −3 −2.8 −2.6 2.8 3 3.2 3.5 3.7 3.9 4.1
    4.3 4.5 4.7 4.9} {
add EtaPhiBins $eta $PhiBins
}
```

```
# default energy fractions {abs(PDG code)} {Fecal Fhcal}
add EnergyFraction {0} {0.0  1.0}
# energy fractions for e, gamma and pi0
add EnergyFraction {11} {1.0  0.0}
add EnergyFraction {22} {1.0  0.0}
add EnergyFraction {111} {1.0  0.0}
# energy fractions for muon, neutrinos and neutralinos
add EnergyFraction {12} {0.0  0.0}
add EnergyFraction {13} {0.0  0.0}
add EnergyFraction {14} {0.0  0.0}
add EnergyFraction {16} {0.0  0.0}
add EnergyFraction {1000022} {0.0 0.0}
add EnergyFraction {1000023} {0.0 0.0}
add EnergyFraction {1000025} {0.0 0.0}
add EnergyFraction {1000035} {0.0 0.0}
add EnergyFraction {1000045} {0.0 0.0}
# energy fractions for K0short and Lambda
add EnergyFraction {310} {0.3  0.7}
add EnergyFraction {3122} {0.3  0.7}

# set ECalResolutionFormula {resolution formula as a function of eta and energy}
# http://arxiv.org/pdf/physics/0608012v1 jinst8_08_s08003
# http://villaolmo.mib.infn.it/ICATPP9th_2005/Calorimetry/Schram.p.pdf
# http://www.physics.utoronto.ca/~krieger/procs/ComoProceedings.pdf
set ECalResolutionFormula {                    (abs(eta) <= 3.2) ∗ sqrt(energy^2∗0.0017^2 +
    energy∗0.101^2) +
(abs(eta) > 3.2 && abs(eta) <= 4.9) ∗ sqrt(energy^2∗0.0350^2 + energy∗0.285^2)}

# set HCalResolutionFormula {resolution formula as a function of eta and energy}
# http://arxiv.org/pdf/hep−ex/0004009v1
# http://villaolmo.mib.infn.it/ICATPP9th_2005/Calorimetry/Schram.p.pdf
set HCalResolutionFormula {                    (abs(eta) <= 1.7) ∗ sqrt(energy^2∗0.0302^2 +
    energy∗0.5205^2 + 1.59^2) +
(abs(eta) > 1.7 && abs(eta) <= 3.2) ∗ sqrt(energy^2∗0.0500^2 + energy∗0.706^2) +
(abs(eta) > 3.2 && abs(eta) <= 4.9) ∗ sqrt(energy^2∗0.09420^2 + energy∗1.00^2)}
}

####################
# Energy flow merger
####################

module Merger EFlowMerger {
# add InputArray InputArray
add InputArray Calorimeter/eflowTracks
add InputArray Calorimeter/eflowPhotons
add InputArray Calorimeter/eflowNeutralHadrons
set OutputArray eflow
}

###################
```

```
# Photon efficiency
###################

module Efficiency PhotonEfficiency {
set  InputArray Calorimeter/eflowPhotons
set  OutputArray photons

# set  EfficiencyFormula {efficiency  formula as a  function  of  eta  and pt}

#  efficiency   formula for photons
set  EfficiencyFormula {                                        (pt  <= 10.0)  *  (0.00)  +
(abs(eta)  <= 1.5)  *  (pt  > 10.0)    *  (0.95)  +
(abs(eta)  > 1.5  && abs(eta) <= 2.5)  *  (pt  > 10.0)    *  (0.85)  +
(abs(eta)  > 2.5)                                        *  (0.00) }
}

##################
# Photon isolation
##################

module Isolation PhotonIsolation {
set  CandidateInputArray PhotonEfficiency/photons
set  IsolationInputArray EFlowMerger/eflow

set  OutputArray photons

set  DeltaRMax 0.5

set  PTMin 0.5

set  PTRatioMax 0.1
}

#################
# Electron   filter
#################

module PdgCodeFilter ElectronFilter {
set  InputArray Calorimeter/eflowTracks
set  OutputArray electrons
set  Invert  true
add PdgCode {11}
add PdgCode {-11}
}

#####################
# Electron  efficiency
#####################

module Efficiency ElectronEfficiency  {
set  InputArray ElectronFilter/electrons
```

```
set OutputArray electrons

# set EfficiencyFormula {efficiency formula as a function of eta and pt}

# efficiency formula for electrons
set EfficiencyFormula {                                              (pt <= 10.0) * (0.00) +
(abs(eta) <= 1.5) * (pt > 10.0)   * (0.95) +
(abs(eta) > 1.5 && abs(eta) <= 2.5) * (pt > 10.0)   * (0.85) +
(abs(eta) > 2.5)                                    * (0.00) }
}

####################
# Electron isolation
####################

module Isolation ElectronIsolation {
set CandidateInputArray ElectronEfficiency/electrons
set IsolationInputArray EFlowMerger/eflow

set OutputArray electrons

set DeltaRMax 0.5

set PTMin 0.5

set PTRatioMax 0.1
}

#################
# Muon efficiency
#################

module Efficiency MuonEfficiency {
set InputArray MuonMomentumSmearing/muons
set OutputArray muons

# set EfficiencyFormula {efficiency as a function of eta and pt}

# efficiency formula for muons
set EfficiencyFormula {                                              (pt <= 10.0) * (0.00) +
(abs(eta) <= 1.5) * (pt > 10.0)   * (0.95) +
(abs(eta) > 1.5 && abs(eta) <= 2.7) * (pt > 10.0)   * (0.85) +
(abs(eta) > 2.7)                                    * (0.00) }
}

################
# Muon isolation
################

module Isolation MuonIsolation {
set CandidateInputArray MuonEfficiency/muons
```

```
set  IsolationInputArray EFlowMerger/eflow

set  OutputArray muons

set  DeltaRMax 0.5

set  PTMin 0.5

set  PTRatioMax 0.1
}

###################
#  Missing ET merger
###################

module Merger MissingET {
#  add InputArray InputArray
add InputArray EFlowMerger/eflow
set  MomentumOutputArray momentum
}

##################
#  Scalar  HT merger
##################

module Merger ScalarHT {
#  add InputArray InputArray
add InputArray UniqueObjectFinder/jets
add InputArray UniqueObjectFinder/electrons
add InputArray UniqueObjectFinder/photons
add InputArray UniqueObjectFinder/muons
set  EnergyOutputArray energy
}


#####################
#  Neutrino Filter
#####################

module PdgCodeFilter NeutrinoFilter {

set  InputArray Delphes/stableParticles
set  OutputArray filteredParticles

set  PTMin 0.0

add PdgCode {12}
add PdgCode {14}
add PdgCode {16}
add PdgCode {−12}
add PdgCode {−14}
```

```
add PdgCode {−16}

}

#####################
# MC truth jet finder
#####################

module FastJetFinder GenJetFinder {
set InputArray NeutrinoFilter/filteredParticles

set OutputArray jets

# algorithm: 1 CDFJetClu, 2 MidPoint, 3 SIScone, 4 kt, 5 Cambridge/Aachen, 6 antikt
set JetAlgorithm 6
set ParameterR 0.6

set JetPTMin 20.0
}


############
# Jet finder
############

module FastJetFinder FastJetFinder {
set InputArray Calorimeter/towers

set OutputArray jets

# algorithm: 1 CDFJetClu, 2 MidPoint, 3 SIScone, 4 kt, 5 Cambridge/Aachen, 6 antikt
set JetAlgorithm 6
set ParameterR 0.6

set JetPTMin 20.0
}

##################
# Jet Energy Scale
##################

module EnergyScale JetEnergyScale {
set InputArray FastJetFinder/jets
set OutputArray jets

# scale formula for jets
set ScaleFormula { sqrt( (3.0 − 0.2∗(abs(eta)))^2 / pt + 1.0 ) }
}

########################
# Jet Flavor Association
```

```
########################

module JetFlavorAssociation JetFlavorAssociation {

set  PartonInputArray Delphes/partons
set  ParticleInputArray Delphes/allParticles
set  ParticleLHEFInputArray Delphes/allParticlesLHEF
set  JetInputArray JetEnergyScale/jets

set  DeltaR 0.3
set  PartonPTMin 5.0
set  PartonEtaMax 2.5

}

###########
# b−tagging
###########

module BTagging BTagging {
set  JetInputArray JetEnergyScale/jets

set  BitNumber 0

# add EfficiencyFormula {abs(PDG code)} {efficiency formula as a function of  eta  and pt}
# PDG code = the highest PDG code of a quark or gluon inside DeltaR cone around jet axis
# gluon's PDG code has the lowest priority

# based on ATL−PHYS−PUB−2015−022

# default  efficiency  formula (misidentification  rate)
add EfficiencyFormula {0} {0.002+7.3e−06∗pt}

# efficiency  formula for c−jets  (misidentification  rate)
add EfficiencyFormula {4} {0.20∗tanh(0.02∗pt)∗(1/(1+0.0034∗pt))}

# efficiency  formula for b−jets
add EfficiencyFormula {5} {0.80∗tanh(0.003∗pt)∗(30/(1+0.086∗pt))}
}

#############
# tau−tagging
#############

module TauTagging TauTagging {
set  ParticleInputArray Delphes/allParticles
set  PartonInputArray Delphes/partons
set  JetInputArray JetEnergyScale/jets

set  DeltaR 0.5
```

```
set TauPTMin 1.0

set TauEtaMax 2.5

# add EfficiencyFormula {abs(PDG code)} {efficiency formula as a function of eta and pt}

# default efficiency formula (misidentification rate)
add EfficiencyFormula {0} {0.01}
# efficiency formula for tau-jets
add EfficiencyFormula {15} {0.6}
}

#####################################################
# Find uniquely identified photons/electrons/tau/jets
#####################################################

module UniqueObjectFinder UniqueObjectFinder {
# earlier arrays take precedence over later ones
# add InputArray InputArray OutputArray
add InputArray PhotonIsolation/photons photons
add InputArray ElectronIsolation/electrons electrons
add InputArray MuonIsolation/muons muons
add InputArray JetEnergyScale/jets jets
}

##################
# ROOT tree writer
##################

# tracks, towers and eflow objects are not stored by default in the output.
# if needed (for jet constituent or other studies), uncomment the relevant
# "add Branch ..." lines.

module TreeWriter TreeWriter {
# add Branch InputArray BranchName BranchClass
add Branch Delphes/allParticles Particle GenParticle

add Branch TrackMerger/tracks Track Track
add Branch Calorimeter/towers Tower Tower

add Branch Calorimeter/eflowTracks EFlowTrack Track
add Branch Calorimeter/eflowPhotons EFlowPhoton Tower
add Branch Calorimeter/eflowNeutralHadrons EFlowNeutralHadron Tower

add Branch GenJetFinder/jets GenJet Jet
add Branch UniqueObjectFinder/jets Jet Jet
add Branch UniqueObjectFinder/electrons Electron Electron
add Branch UniqueObjectFinder/photons Photon Photon
add Branch UniqueObjectFinder/muons Muon Muon
add Branch MissingET/momentum MissingET MissingET
add Branch ScalarHT/energy ScalarHT ScalarHT}
```